Development, Computational and Experimental Characterization of a Canard Aircraft Configuration

Pedro Miguel Micaelo Fernandes

Thesis to obtain the Master of Science Degree in

Aerospace Engineering

Supervisors: Prof. Afzal Suleman
Dr. José Lobo do Vale

Examination Committee

Chairperson: Prof. Fernando José Pacharro Lau
Supervisor: Prof. Afzal Suleman
Member of the Committee: Prof. Frederico José Prata Rente Reis Afonso

November 2021

Acknowledgments

This thesis is the culmination of the work done for the past five years in order to get my aerospace degree but also of the people that have had a positive influence throughout my academic journey and the rest of my life. I am forever grateful to them.

I would like to start by thanking Professor Afzal Suleman for giving me the opportunity to study at the University of Victoria - Centre for Aerospace Research in Canada in a project of great interest and for always being available to help me and my colleagues with any problems, thesis related or not.

I would also like to thank the people I met at CfAR who helped me professionally in my thesis. A special mention to Dr. José Vale for guiding me in the right direction, teaching me valuable knowledge, correcting my mistakes, and sharing the experience he acquired over the years. I would also like to thank John Rafaelli for helping me with the manufacturing process of the wing analyzed in this thesis.

Thank you to my friends, those that came with me to Canada and with whom I was able to make great memories, those that I met in Canada and that I hope I will see many more times, and those in Europe that have helped me become who I am today. A special acknowledgment to Hugo Faustino for helping during the GVT, but also for being a great friend throughout the whole journey.

Last but not least, my deepest gratitude to my family for financially and emotionally supporting me all my life, my parents, my sister, and my grandparents.

Resumo

O objetivo desta dissertação é desenhar estruturalmente e aerodinâmicamente um novo veículo aéreo não tripulado com configuração canard e capacidade de descolagem e aterragem na vertical para ser usado pelo Departamento de Defesa Nacional do Canadá com vista a detetar submarinos ao longo da costa do país utilizando um sensor de deteção de anomalias magnéticas.

Inicialmente, um processo incompleto de otimização multidisciplinar com base em modelos de aproximação foi completado de modo a alcançar uma solução otimizada.

Depois da solução otimizada ter sido alcançada, pequenos ajustes ao desenho fora do processo de otimização foram estudados para testar o seu impacto no desempenho da aeronave. Uma mudança ao canard foi feita devido a requisitos da velocidade de perda. Simulações de interação fluido-estrutura de sentido único foram realizadas para validar a integridade estrutural da configuração. Por fim, uma caracterização extensiva aerodinâmica da aeronave foi completada incluindo simulação de interação fluido-estrutura nos dois sentidos na condição cruzeiro. A seguir, as superfícies de controlo foram definidas e a inércia da aeronave foi estimada. Com estas características, um modelo dinâmico de voo foi construído em *Simulink* e os modos dinâmicos foram estudados para assegurar a estabilidade da aeronave.

Por fim, a asa projetada foi manufaturada e tanto testes estáticos como de vibração em solo foram realizados de forma a se comparar a amostra manufaturada a um modelo de elementos finitos com vista a futuras análises de aeroelasticidade.

Palavras-chave: Veículo Aéreo Não Tripulado, Otimização Multidisciplinar, Interação Fluido-Estrutura, Modelo Dinâmico de Voo, Testes de Carga Estáticos, Testes de Vibração em Solo.

Abstract

The goal of this dissertation is to structurally and aerodynamically design a new canard fixed-wing configuration with Vertical Take-Off and Landing (VTOL) capability Unmanned Aerial Vehicle (UAV) to be used by the Defense Research and Development Canada (DRDC) to detect submarines of the coast of Canada using a Magnetic Anomaly Detection (MAD) sensor.

Initially, a surrogate-based Multidisciplinary Design Optimization (MDO) process that was not yet finished is completed in order to reach a structurally and aerodynamically optimized solution.

After the optimized solution was obtained, small design changes outside of the optimization process were analyzed to test their impacts on the aircraft performance. A design change to the canard was made due to stall speed requirements. One-way Fluid-Structure Interaction (FSI) simulations were performed to validate the structural integrity of the configuration. Changes were also made to the preliminary solution from the optimization process in this step. Finally, an extensive aerodynamic characterization of the aircraft was completed including a two-way FSI at cruise condition. Next, the control surfaces were defined and estimates of the inertia of the aircraft were made. With these characteristics, a flight dynamics model was constructed using *Simulink* and the dynamic modes were studied to prove the stability of the aircraft.

Finally, the projected wing was manufactured and static loading tests and Ground Vibration Tests (GVT) were performed in order to compare the manufactured specimen to a finite element model which can be used for future aeroelasticity analysis.

Keywords: Unmanned Aerial Vehicle, Multidisciplinary Design Optimization, Fluid-Structure Interaction, Flight Dynamics Model, Ground Vibration Tests, Static Load Tests.

Contents

Acknowledgments . . . iii

Resumo . . . v

Abstract . . . vii

List of Tables . . . xiii

List of Figures . . . xv

Nomenclature . . . xix

Glossary . . . xxiii

1 Introduction **1**

1.1 Motivation . . . 1

1.2 State of the Art . . . 2

1.2.1 History of Unmanned Aerial Vehicles . . . 2

1.2.2 Multidisciplinary Design Optimization . . . 3

1.2.3 Fluid-Structure Interaction . . . 4

1.2.4 Experimental Ground Tests . . . 4

1.3 Objectives and Deliverables . . . 4

1.4 Thesis Outline . . . 5

2 Theoretical Background **7**

2.1 Multidisciplinary Design Optimization . . . 7

2.1.1 Problem Formulation . . . 7

2.1.2 Surrogate Model - Kriging . . . 7

2.1.3 Surrogate Search . . . 8

2.1.4 Optimization Algorithm - Genetic Algorithm . . . 9

2.2 Structural Analysis . . . 9

2.2.1 Finite Element Method . . . 9

2.2.2 Composite Materials - Tsai-Wu Failure Criteria . . . 10

2.3 Aerodynamic Analysis . . . 11

2.3.1 Computational Fluid Dynamics . . . 11

2.4 Fluid-Structure Interaction . . . 12

2.5 Flight Dynamics . . . 13

2.5.1 State Space Formulation 15
2.5.2 Dynamic Modes 15
2.6 Modal Analysis 16
2.6.1 Eigenvalues and Eigenvectors 16
2.7 Ground Vibration Tests 18
2.7.1 Impact Testing 18
2.7.2 Roving Hammer vs Roving accelerometer 18

3 Multidisciplinary Design Optimization 19
3.1 Optimization Tool 19
3.2 Problem Formulation 19
3.2.1 Mission Requirements 19
3.2.2 Objective Function 20
3.2.3 Design Variables and Parametrization 21
3.3 MDA Procedure 22
3.4 Geometric Models 23
3.4.1 Structural Analysis 23
3.4.2 CFD analysis 24
3.5 MDO Methodology 25
3.5.1 Surrogate Models 25
3.5.2 Search Algorithm 26
3.6 Optimization Results 26
3.6.1 Final configuration 30

4 Aircraft Characterization 35
4.1 Design change study 35
4.2 Stall Speed Determination 36
4.3 Winglet modification 40
4.4 Structural Validation 41
4.5 Aircraft Performance 45
4.5.1 Cruise Performance in Deformed State 45
4.5.2 Velocity Dependent Trim Condition 46
4.6 Control Surfaces Design 50
4.7 Flight Dynamics Model 52
4.8 Stability 54

5 Experimental Testing 57
5.1 Manufacturing 57
5.2 Ground Vibration Testing 61
5.2.1 Mode shape analysis 62

5.3 Wing Static Loading 66
5.3.1 Photogrammetry 66
5.3.2 $1g$ Loading Case 68
5.3.3 $3g$ and $4.5g$ Loading Cases 69

6 Conclusions 73
6.1 Achievements 73
6.2 Future Work 74

Bibliography 75

A Aerodynamic and Stability Derivatives 79
A.1 Aerodynamic Derivatives 79
A.2 Stability Derivatives 79

List of Tables

3.1 Optimization design variables 22
3.2 Carbon fiber material properties 23
3.3 Comparison between iteration 61 and iteration 68. 31
3.4 Values of the design variables for the final chosen design. 32

4.1 Comparison of the three configurations and their stall properties. 39
4.2 PVC foam material properties 42
4.3 Aerodynamic derivatives. 53
4.4 Aircraft component list. 53

5.1 Impact locations and Degrees of Freedom. 62
5.2 Sensor locations and Degrees of Freedom. 62
5.3 Wing mode shapes and respective natural frequencies. 63
5.4 Mass distribution along the wing for both tests. 70

List of Figures

1.1 First UAVs: Curtiss N-9 modified as an aerial torpedo and Kettering Bug. 2

2.1 Examples of conforming mesh (a) and non-conforming mesh (b) [19]. 12
2.2 Conventions used for the body and earth reference frames. 13

3.1 Examples of the structural model and OML of a configuration. 24
3.2 Mesh domain and mesh elements around aircraft for an example configuration. 25
3.3 Evolution of the lift to drag ratio along the optimization. 27
3.4 Evolution of the structural mass along the optimization. 27
3.5 Evolution of the Tsai-Wu failure index along the optimization. 28
3.6 Evolution of the objective function along the optimization. 28
3.7 Evolution of the range ratio R/R_{ref_0} along the optimization. 29
3.8 L/D vs structural mass plot. 29
3.9 Close-up of the evolution of the range ratio R/R_{ref0} along the optimization. 30
3.10 Top and Isometric views of configuration 61. 30
3.11 Top and Isometric views of configuration 68. 31
3.12 Geometric dimensions of configuration 68. 33
3.13 Tsai-Wu failure index values on the entire aircraft structure. 34
3.14 Tsai-Wu failure index values on critical regions. 34

4.1 Top and Isometric views of swept-back configuration. 35
4.2 C_L and C_m as a function of α. 37
4.3 Top and Isometric views of configuration with a 20% bigger canard area. 38
4.4 Top and Isometric views of configuration with a 109% bigger canard area. 38
4.5 Stall speed calculation based on wing and canard area. 40
4.6 Old and new versions of the winglet. 41
4.7 Structural model in *Ansys Mechanical* 42
4.8 Imported pressure mapped on the structural components. 43
4.9 Tsai-Wu failure index on initial aircraft structure and close-up on wing root. 43
4.10 Tsai-Wu failure index on revised aircraft structure and resulting deformation. 44
4.11 Pressure distribution on the aircraft's surfaces and symmetry plane. 46
4.12 Streamlines around the aircraft body. 46

4.13 Tsai-Wu failure index on aircraft structure from cruise speed two-way FSI. 47
4.14 C_L, C_D and C_m vs α plots with trendlines for all three coefficients. 48
4.15 Lift over Drag ratio for different forward velocities. 49
4.16 $C_{L_{trim}}$, $C_{L_{w+fus}}$, and C_{L_c} vs airspeed and Lift over Drag ratio vs $C_{L_{trim}}$ plots. 49
4.17 Trimmed angles for different forward velocities. 49
4.18 Power and Thrust required for trim condition for different forward velocities. 50
4.19 Top and Isometric view of the aircraft with ailerons actuated. 51
4.20 Lateral and isometric view of the aircraft with rudder actuated. 52
4.21 Flight Dynamics Model architecture. 54
4.22 Dynamic Model subsystem architecture. 54
4.23 Eigenvalue evolution for longitudinal motion. 55
4.24 Eigenvalue evolution for lateral motion. 55
4.25 1° canard half a second pulse dynamic simulation at 35 m/s. 56
4.26 1° aileron half a second pulse dynamic simulation at 35 m/s. 56

5.1 CAD Mold assembly. 57
5.2 Close-up of the wingtips mold CAD assembly. 58
5.3 Manufactured molds. 59
5.4 Manufacturing of the lower surface. 59
5.5 Internal structure glued to the upper surface and lower surface. 60
5.6 Manufactured wing. 60
5.7 Setup of the wing for GVT. 61
5.8 FE model from *Ansys* and *MEScope* model of the wing. 62
5.9 1st out-of-plane symmetrical bending. 63
5.10 1st out-of-plane anti-symmetrical bending. 63
5.11 1st torsion mode shape. 64
5.12 2nd out-of-plane symmetrical bending. 64
5.13 2nd out-of-plane anti-symmetrical bending. 64
5.14 2nd torsion mode shape. 64
5.15 3rd out-of-plane symmetrical bending. 65
5.16 1st in-plane symmetrical bending. 65
5.17 3rd torsion mode shape. 65
5.18 Wing fixed support setup for static load tests. 66
5.19 Setup of the wing before static load tests. 67
5.20 Point clouds of undeformed shape and $1g$ loading condition shape. 67
5.21 Photograph of $1g$ loading condition. 68
5.22 3D plot of the deformed and undeformed LE and TE from both experimental and computational results. 69
5.23 Smoothing of the extracted points from the photogrammetry software. 69

5.24 Displacement of the LE and TE for both methods. 70

5.25 Photographs of the 3g and 4.5g loading conditions. 71

Nomenclature

Greek symbols

α	Angle of attack.
β	Angle of side-slip.
γ	Twist angle.
δ	Control surface deflection.
ϵ	Turbulent dissipation.
ζ	Damping coefficient.
η	Propeller efficiency.
θ	Pitch angle.
Λ	Sweep angle.
λ	Eigenvalues, taper ratio.
ν	Poisson’s ratio.
ρ	Density.
σ_i	Stress tensor components.
τ_{ij}	Shear strength components.
ϕ	Roll angle.
χ	Feasible set of design points.
ψ	Yaw angle.
ω	Turbulent frequency.
ω_n	Natural frequency.

Roman symbols

A	Dynamic Matrix.

AR	Aspect Ratio.
b	Span.
$BSFC$	Brake specific fuel consumption.
C	Damping matrix.
c	Chord.
$\bar{c}$	Mean aerodynamic chord.
C_D	Coefficient of drag.
C_L	Coefficient of lift.
C_l	Coefficient of roll moment.
C_m	Coefficient of pitch moment.
C_n	Coefficient of yaw moment.
C_Y	Coefficient of lateral force.
cbr	Airfoil camber.
D	Drag.
E	Elastic modulus.
F	Force.
f	Frequency.
$f(\mathbf{x})$	Search function.
F^a	Applied load vector.
F^r	Reaction load vector.
F_{ij}	Strength tensors.
G	Shear modulus.
g	Acceleration of gravity.
h_n	Composite layer thickness.
I	Inertia matrix.
i_c	Canard incidence angle.
K	Stiffness matrix.
k	Turbulent kinetic energy.

k_e	Element stiffness matrix.
K_n	Static margin.
L	Lift.
l_c	Distance between canard and wing aerodynamic centers.
l_w	Distance between wing aerodynamic center and center of gravity.
M	Moment, mass matrix.
m	Mass.
m_f	Final mass at the end of the mission segment.
m_i	Initial mass.
m_s	Structural mass.
p	Pressure.
p, q, r	Angular velocity cartesian components.
R	Range.
r	Radius.
S	Surface area.
S_S	In-plane shear strength.
S_{Lc}	Longitudinal compressive strength.
S_{Lt}	Longitudinal tensile strength.
S_{Tc}	Transverse compressive strength.
S_{Tt}	Transverse tensile strength.
$[S]$	Transformation matrix.
t	Time, airfoil relative thickness.
thk	Composite thickness.
$\mathbf{u}$	Velocity vector.
u, v, w	Linear velocity cartersian components.
u_n	Nodal displacement vector.
V	Speed.
x, y, z	Cartesian position.

Subscripts

A	Aileron.
c	Canard.
$cruise$	Cruise.
$disc$	Wing chord discontinuity.
f	Fin.
f_{spar}	Front wing spar.
i, j, k	Computational indexes.
i_c	Canard angle of incidence.
max	Maximum.
min	Minimum.
n	Normal component.
R	Rudder.
ref	Reference.
$root$	Root of the wing.
$stall$	Stall.
T	Thrust.
tip	Tip of the wing.
$trim$	Trim condition.
w	Wing.
$wglt$	Winglet.
x, y, z	Cartesian components.

Superscripts

T	Transpose.

Glossary

ACP	Ansys Composite PrepPost
CAD	Computer-Aided Design
CFD	Computational Fluid Dynamics
CFRP	Carbon Fiber Reinforced Polymers
CNC	Computer Numerical Control
CSM	Computational Structural Mechanics
CfAR	Centre for Aerospace Research
CoG	Center of Gravity
DOF	Degrees of Freedom
DRDC	Defense Research and Development Canada
EOM	Equations of Motion
FCM	Flight Control System
FDM	Flight Dynamics Model
FEA	Finite Element Analysis
FEM	Finite Element Method
FE	Finite Element
FRF	Frequency Response Function
FSI	Fluid-Structure Interaction
FVM	Finite Volume Method
GA	Genetic Algorithm
GVT	Ground Vibration Tests
HF	High Fidelity
IP	In-Plane
LE	Leading Edge
LF	Low Fidelity
LLT	Lifting Line Theory
LTI	Linear Time-Invariant
MAD	Magnetic Anomaly Detection
MDA	Multidisciplinary Design Analysis
MDF	Medium Density Fiberboard

MDOF	Multiple Degrees of Freedom
MDO	Multidisciplinary Design Optimization
MLE	Maximum Likelihood Estimation
MPC	Multi-Point Constraints
MTOM	Maximum Take-Off Mass
NACA	National Advisory Committee for Aeronautics
OML	Outer Mold Line
OP	Out-of-Plane
RBM	Rigid-Body Motion
SDOF	Single Degree of Freedom
SFOC	Special Flight Operations Certificate
SST	Shear Stress Transport
TE	Trailing Edge
UAV	Unmanned Aerial Vehicle
UD	Unidirectional
UVic	University of Victoria
VTOL	Vertical Take-Off and Landing
WB2	Watson and Barnes Criterion

Chapter 1

Introduction

The will to fly is as old as civilization itself. The first time man conquered the skies through manned flight was with lighter than air aircraft in 1783 via the use of hot air balloons but only in 1903 were the Wright brothers able to make the first powered heavier-than-air manned flight [1, 2].

After more than a century of technological advancements in aerospace engineering after this flight, a big focus is turning to Unmanned Aerial Vehicles (UAVs). The fact that these systems do not need a crew and can be remotely piloted or even autonomous makes them safer in terms of not putting on board human lives at risk and also more efficient because they can be more compact and operate for longer hours. This brings many applications in various sectors, from agriculture and farming to leisure and aerial photography [3].

1.1 Motivation

An industry that is at many times at the forefront of technology is the military. In this field, the necessity for having the most advanced systems regularly outweighs the cost associated with research and development.

The motivation for this thesis is the design and development of a canard fixed-wing configuration with Vertical Take-Off and Landing (VTOL) capability Unmanned Aerial Vehicle (UAV) that is being pursued by the University of Victoria (UVic) Centre for Aerospace Research (CfAR) in collaboration with the Defense Research and Development Canada (DRDC), and it is meant to be used by the Canadian Air Force for Magnetic Anomaly Detection (MAD) operations of surveillance of the Canadian maritime borders. It will look for magnetic signals originating from submerged metallic vehicles, namely submarines.

This thesis work is the continuation of the work done in two other MSc theses. Bruno Luís did part of the conceptual and preliminary design so some decisions of the aircraft configuration were already established [4]. Then Tiago Jesus built a Multidisciplinary Design Optimization (MDO) tool in order to structurally and aerodynamically size the drone but whose optimization process was not yet converged [5]. The major objective of this work is to complete the optimization and increase the detail of the design including aero-structural characterization, dynamic modeling, and experimental validation.

1.2 State of the Art

1.2.1 History of Unmanned Aerial Vehicles

Unmanned aerial vehicles, sometimes referred to as drones, began to appear shortly after the first heavier than air manned flight in 1903. Elmer Sperry, the inventor of the gyroscope, started implementing these devices in order to stabilize aircraft in 1913. With the advent of the first world war, the pursue of unmanned aircraft became more important as it could be a way of gaining a military advantage. The first UAVs were aerial torpedoes like the modified Curtiss N-9s (figure 1.1(a)) and the Kettering Bug (figure 1.1(b)). These were made to explode on impact and they flew in 1917 and 1918 respectively, albeit with a low success rate of hitting their targets due to launch problems, engine failures, and unstable behavior. With the end of the war in the same year, these aircraft ended up not being utilized in combat [6].

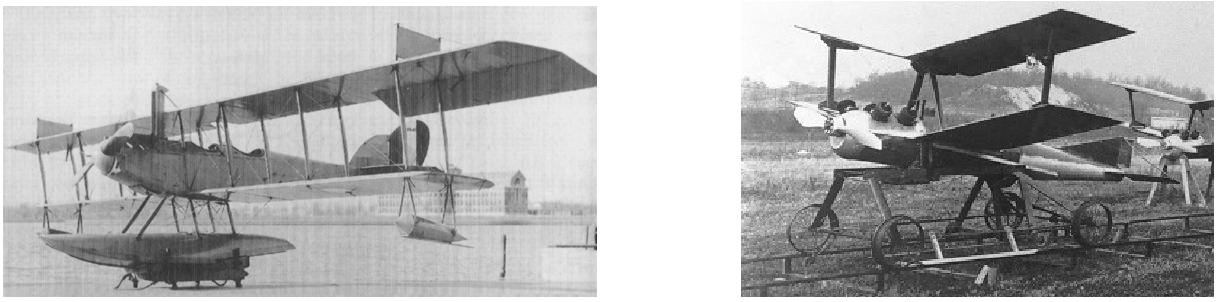

(a) Modified Curtiss n-9 [7].

(b) Kettering Bug [8].

Figure 1.1: First UAVs: Curtiss N-9 modified as an aerial torpedo and Kettering Bug.

As hostilities ceased, the focus on unmanned aircraft fell in favor of air transport during the period between world wars. Nevertheless, some testing was still taking place with radio-controlled drones being used as aerial targets. The success of these drones revived the interest in UAV technology as weapons delivery and guided-missile platforms [9].

With the beginning of the second world war came one of the first successful cruise missiles, the V-1 flying bomb, part of the Vengeance weapons designed by Nazi Germany to attack Great Britain. With almost 9000 bombs landing in the UK causing more than 6200 casualties and seriously wounding 18000 others, the V-1 proved its effectiveness even if it had little impact on the outcome of the war [9, 10].

The Cold War brought to light a new application of UAVs as reconnaissance systems due to the necessity of both the USA and the USSR of spying on each other without suffering casualties if the surveillance aircraft was detected in enemy airspace. This made UAVs gain traction as fundamental warfare weaponry which only increased throughout the rest of the century and especially after wars like the Vietnam war and the Israel/Lebanon conflict where they were used for photography, electronic detection, jamming, deception and even spreading propaganda leaflets [10].

Nowadays UAVs are not limited to military operations. The number of civil applications and use, by government agencies, corporations, and even individuals, rose as the cost of this technology has fallen. One can highlight aerial photography, imaging and mapping, fire detection and forest protection, chemical spraying, crop dusting and filming for the entertainment industry as some of the nonmilitary applications for UAVs. They can be classified according to multiple categories such as weight, flight ceiling, endurance, and takeoff method, each having its advantages and disadvantages [3, 11].

1.2.2 Multidisciplinary Design Optimization

Multidisciplinary Design Optimization is a field that has developed significantly in the most recent decades with new design tools, methodology approaches, and better computational analysis capacity making it more abundantly used and important in design processes. The difference between the state of the art in this area in the nineties and now is evident when comparing papers from both eras summarizing the most recent advancements like [12, 13] and [14], respectively. The origins of this method are related to aerospace engineering, but it has since been applied to other engineering industries and applications [15].

One of the most important steps when carrying out an MDO study is correctly formulating the optimization problem. This is done not only by considering a selection of objectives that describe the desired design qualities but also by choosing a representative combination of design variables [16].

The objectives are usually related to either weight, aerodynamics, or mission performance, where the latter can be further broken down into range, cost, fuel burn, and other less frequent targets (*e.g.* environmental). Most of the problems are single-objective, but they can also be combined either by a single function or by formulation of multi-objective problems [14].

The design variables and constraints guarantee an accurate exploration of the design space. Sensitivity analysis of the design variables on the objective allows for reductions of the total number of parameters while constraints are usually related to case-dependent features or common airworthiness aspects [17].

Other essential components of the optimization framework are the disciplinary models. The most common and usually primary disciplines are aerodynamics, weight estimation, structural analysis, and propulsion. Geometric models, stability and trim, and mission performance (like the amount of energy required for different flight segments) are also common but as support elements to the optimization. Rarer, but still prevalent is using alternative models like environmental impact (as in emission pollution and/or noise levels), flight dynamics or cost and life cycle as part of the optimization process. Even less often but still existent is using subsystem simulations and electromagnetism in the framework [14].

The necessity of correctly simulating the problem but also of having fast iterations determines the level of fidelity employed. Low Fidelity (LF) approximations like panel method codes or empirical equations are usually used in the conceptual design stage while High Fidelity (HF) tools like Computational Fluid Dynamics (CFD) and Computational Structural Mechanics (CSM) are reserved more for the detailed design stage or if the product is unconventional. Medium fidelity approaches like Euler solvers or simplified geometry analysis are a trade-off between high and low which can prove beneficial in certain situations [18].

1.2.3 Fluid-Structure Interaction

The demand for an increase in accuracy in science and engineering simulations today more constantly requires the coupling of multiple physical fields. One of the most common but also challenging multidisciplinary problems are Fluid-Structure Interactions (FSI), *i.e.*, interactions between one or more solid elastic structures with an internal or surrounding fluid flow. The applications of these are extensive, from parachutes and airplane wings to blood flow in arteries and inner ear fluid dynamics [19, 20].

The solution to an FSI problem can be either iterative or non-iterative depending on the coupling of the two disciplines. The fluid flow is usually calculated first to determine the velocity and pressure fields. The pressure at the interface is then used to solve the solid equations. If the displacements from the structural simulations are then used to recalculate the fluid flow equations and this process is repeated until convergence is reached, then the solution is iterative. This is the common procedure for the usual study cases in FSI problems. However, in the uncoupled approach, there is a single calculation for the fluid domain and a subsequent evaluation of the structural results. In this case, the interaction is only one-way and although rarer, it can also prove to be a useful tool. This thesis makes use of both types. The first is used for calculating the aerodynamic performance while in cruise conditions where the fluid results with the deformed aircraft state are important while the second method is used for calculating the structural response to the ultimate load case, where going back to the fluid simulation would not significantly change the outcome as this is a conservative approach.

1.2.4 Experimental Ground Tests

The search for more efficient aircraft designs that provide better aerodynamic results often leads to the use of high aspect ratio wings and strong lightweight materials. A disadvantage of these implementations is an increase in flexibility and a reduction of the frequencies of the structural modes. This can result in reduced performance and make aeroelastic instabilities such as flutter or divergence apparent in the normal operational flight envelope.

To validate an aircraft design for these situations, numerical modeling and computational simulations may not be sufficient if the structural model does not exactly reproduce the manufactured pieces. For this reason, ground tests can be used to validate the data and update the computational models.

Two of the most common ground tests are static load and Ground Vibration Tests (GVT). The former is better aimed at demonstrating the stiffness limit and ultimate load requirements while the latter is better suited to obtain the aircraft mode shapes which can then be used for flutter calculations [21, 22]. Both tests will be performed to validate the structural model of the wing designed for this aircraft which can be used in the future to update its design.

1.3 Objectives and Deliverables

The following tasks are the objectives that are meant to be fulfilled by this thesis work:

- Structurally and aerodynamically size a UAV with the longest range possible given the constraints of the design and the mission through the use of an MDO process;
- Analyze the performance of the selected design and make the necessary changes to ensure all requirements are met;
- Perform FSI simulations to obtain the aerodynamic efficiency during cruise conditions with the deformed structure caused by the fluid pressure loads;
- Size the control surfaces, build a Flight Dynamics Model (FDM) and perform stability analysis to guarantee a stable behavior;
- Build and test the designed wing for static load and ground vibration tests.

1.4 Thesis Outline

There are five additional chapters in this thesis. Below is a small description of each of them.

Chapter 2 - Theoretical Background

In this chapter a brief explanation of the important concepts required to understand this dissertation is presented. This includes a description of the simulation models, composite materials, the multidisciplinary optimization process, fluid-structure interaction, and the experimental tests done.

Chapter 3 - Optimization Process

In this chapter, the entire MDO process is detailed, including the problem formulation, the Multidisciplinary Design Analysis (MDA) procedure, and the MDO methodology. The attainment of the final configuration is also described.

Chapter 4 - Aircraft Characterization

In this chapter, the final configuration obtained from the optimization process is tested. Aerodynamic and structural changes are made to make the solution from the previous chapter meet stall speed requirements and structural viability. The aerodynamic characteristics are obtained and a 2-way fluid-structure interaction is performed to check if the deformation from the aerodynamic loads affects the aerodynamic performance of the aircraft. The control surfaces are sized and a flight dynamics model is built in order to simulate the aircraft. A stable behavior is also ensured.

Chapter 5 - Experimental Testing

To validate the structural results obtained in the last chapter, a composite wing is built and GVT and static loading tests are performed. The procedure and the results of these tests are explored in this chapter.

Chapter 6 - Conclusions

In this chapter a short analysis of the achieved objectives and the work done is available as well as a discussion about points of improvement.

Chapter 2

Theoretical Background

2.1 Multidisciplinary Design Optimization

2.1.1 Problem Formulation

The first step in an optimization process is defining the problem. Taking into account the goal of the optimization, an objective function f is defined as a way to quantitatively measure how good a design is which allows the comparison between two different designs.

Each design is defined by the design variables which are changeable parameters that influence function f. A design point $\mathbf{x}$ is a k-dimensional vector of values corresponding to k different design variables. The domain in which these can change is called the design space.

Design limitations are called constraints. If they are related to the design variables they are called bounds but they can also be outcome dependent. They can be either equalities or inequalities.

Thus, it is possible to state the optimization problem as:

$$\begin{aligned} \text{Minimize} \quad & f(\mathbf{x}) \\ \text{w.r.t.} \quad & \mathbf{x} \in \chi\,, \\ \text{subject to} \quad & h_i = 0,\ i = 1, ..., N_i \\ & g_j \geq 0,\ j = 1, ..., N_j\,, \end{aligned} \tag{2.1}$$

where χ is the feasible set of design points corresponding to the region of the domain in $\mathbb{R}^k$ where all constraints are satisfied, h is the vector of equality constraints and g is the vector of inequality constraints which includes the bounds [23].

2.1.2 Surrogate Model - Kriging

A surrogate model is a mathematical approximation that mimics the behavior of the system it is trying to substitute. It is generally much faster to compute but it is susceptible to large deviations from the real values. The surrogate model used in the MDO present in this project is a Kriging model [24].

Being $\mathbf{x}^{(i)}(i = 1, ..., n)$ the sample points at which the real function was evaluated and $\mathbf{y} = [y^{(1)}, ..., y^{(n)}]$ the function results at those given points, the stochastic process that originates $y(\mathbf{x})$, $Y(\mathbf{x})$, can be represented by:

$$Y(\mathbf{x}) = \mu_m + \epsilon(\mathbf{x}) \, , \tag{2.2}$$

where μ_m is the mean of the response at a sampled design point and $\epsilon(\mathbf{x})$ is the error that represents the fluctuations around the trend function which has a zero expected value $E[\epsilon(\mathbf{x})] = 0$ because it originates from a stationary Gaussian process.

The correlation between two points $\mathbf{x}$ and $\mathbf{x}'$ is given by the following squared exponential kernel function:

$$\text{cor}[Y(\mathbf{x}), Y(\mathbf{x}')] = \exp\left(\sum_{j=1}^{k} \theta_j (\mathbf{x}_j - \mathbf{x}'_j)^2\right) \, , \tag{2.3}$$

where k is the number of design variables.

The parameters θ must be adequately chosen in order to build an accurate approximation model since these affect the influence of each design variable on the function that is to be approximated. This assignment is done using the Maximum Likelihood Estimation (MLE) method, which measures the probability of the initial data set resulting from the model, given the θ parameters set [24].

2.1.3 Surrogate Search

Having the initial surrogate model, it is necessary to decide which new design points to evaluate in search of the global optimum. Four criteria were utilized to do this task in this MDO process.

The first is prediction-based exploration which is a local optimization technique that selects the point that minimizes the objective function. It can be an efficient search method but it might get stuck on local minima making it less useful than other more global criteria in the initial surrogate search.

The expected improvement exploration is one of those more global search criteria that focuses on maximizing the expected improvement over the current best function evaluation. It takes into account both the probability of improvement and the amount of improvement which facilitates not getting stuck on local minima but may make the optimization slow to converge [23, 24]

The Watson and Barnes criterion (WB2) is a method falling in between both previous methods because it takes into account both expected improvement but also the prediction values making it good at finding regional minima. Lastly, the WB2S criterion adds a scaling factor to WB2 that helps the exploration remain more global than prediction based as the number of evaluated design points increases [25].

Instead of constraining the optimization of the objective function, it is possible to take the existing constraints into a probability of feasibility function that assesses the probability that the constraints are met. This can then be merged with the objective function in a new search function that will run unconstrained

[24].

2.1.4 Optimization Algorithm - Genetic Algorithm

With the search methods defined, it is still necessary to choose the optimization algorithm to operate the search. Population methods are appropriate for the case of a surrogate optimization with an initial randomly obtained database of points. These points are called individuals and the current set of points is called the population.

The population method chosen for this MDO was a Genetic Algorithm (GA). These are inspired in biological evolution because fitter individuals have a higher chance of transmitting their genes, *i.e.*, the design points that have the best objective function values are more probable to pass onto the next generation after undergoing crossover and mutation events. The former allows for a combination of chromosomes between parents to generate children while mutations allow for more exploration of the design space that might not happen with just the initial population [23].

2.2 Structural Analysis

For the structural analysis performed, Finite Element Analysis (FEA) are used with the help of *ANSYS Mechanical APDL* and *ANSYS Workbench* software. Since the materials used are Carbon Fiber Reinforced Polymers (CFRP), the Tsai-Wu failure criterion is used to check if there is structural failure [26].

2.2.1 Finite Element Method

The Finite Element Method (FEM) is a method used to approximately solve the differential equations that characterize the problem and that could be impossible to resolve from analytical methods.

The structure being tested is divided into subdomains called elements that form a mesh. The governing equations are approximated at each element by functions and algebraic equations that connect the solution values at a finite number of pre-selected points called element nodes. These equations are then combined through inter-element continuity of the solution and a balance of inter-element forces. The resulting simulation is a static analysis that is valid for all degrees of freedom [27].

The overall equilibrium equation that describes the mechanical behavior of the discretized structure is:

$$[K]\{u_n\} = \{F\} \Leftrightarrow [K]\{u_n\} = \{F^a\} + \{F^r\}, \quad [K] = \sum_{m=1}^{N} [k_e] \, , \tag{2.4}$$

where $[K]$ is the total stiffness matrix, N is the number of elements, $[k_e]$ is the element stiffness matrix, $\{u_n\}$ is the nodal displacement vector, $\{F^a\}$ is the applied load vector, *i.e.*, applied nodal loads, thermal loads and pressure loads, and $\{F^r\}$ is the reaction load vector.

The stiffness matrix is obtained from the material properties, the geometric dimensions and the strain matrix, which is built from the shape functions of the chosen finite element. Knowing this for each element, it is possible to obtain the displacements for the complete structure [28].

2.2.2 Composite Materials - Tsai-Wu Failure Criteria

Anisotropic material properties are direction-dependent. This means that isotropic material failure criteria are not applicable and the strength and stress in all directions must be taken into account.

Laminate composites are classified as orthotropic materials which is a subset of anisotropic materials whose properties are different in three mutually orthogonal directions.

For a single ply of a laminate, the five independent strength constants that coincide with the maximum allowed in-plane stresses in the principal axes are:

- S_{Lt} - Longitudinal tensile strength
- S_{Lc} - Longitudinal compressive strength
- S_{Tt} - Transverse tensile strength
- S_{Tc} - Transverse compressive strength
- S_S - In-plane shear strength

Tsai and Wu determined that failure takes place if the following quadratic condition for a six-dimensional stress space is verified:

$$F_i\sigma_i + F_{ij}\sigma_i\sigma_j = 1\,, \qquad i,j = 1,...,6\,, \tag{2.5}$$

where $\sigma_{1,2,3}$ are the direct stresses in each of the principal directions, $\sigma_4 = \tau_{23}$, $\sigma_5 = \tau_{31}$, $\sigma_6 = \tau_{12}$ are the shear stresses and F_i and F_{ij} are stress tensors.

For a single orthotropic laminate ply subject to plane stress, the aforementioned equation can be simplified to:

$$F_1\sigma_{11} + F_2\sigma_{22} + F_6\tau_{12} + F_{11}\sigma_{11}^2 + F_{22}\sigma_{22}^2 + F_{66}\tau_{12}^2 + 2F_{12}\sigma_{11}\sigma_{22} = 1\,, \tag{2.6}$$

where the expressions for the strength coefficients are:

$$\begin{aligned}
&F_1 = \frac{1}{S_{Lt}} - \frac{1}{S_{Lc}}\,;\\
&F_2 = \frac{1}{S_{Tt}} - \frac{1}{S_{Tc}}\,;\\
&F_6 = 0\,;\\
&F_{11} = \frac{1}{S_{Lt}S_{Lc}}\,;\\
&F_{22} = \frac{1}{S_{Lt}S_{Lc}}\,;\\
&F_{66} = \frac{1}{S_S^2}\,.
\end{aligned} \tag{2.7}$$

The term F_{12} must be determined by a biaxial tensile test. In this test, the shear stress τ_{12} is null and the stress state will be an equal tensile stress in both principal directions, $\sigma_{11} = \sigma_{22} = \sigma$. By replacing the known stresses and coefficients in equation 2.6 one gets:

$$F_{12} = \frac{1}{2\sigma^2}\left[1 - \left(\frac{1}{S_{Lt}} - \frac{1}{S_{Lc}} + \frac{1}{S_{Tt}} - \frac{1}{S_{Tc}}\right)\sigma - \left(\frac{1}{S_{Lt}S_{Lc}} + \frac{1}{S_{Lt}S_{Lc}}\right)\sigma^2\right]. \tag{2.8}$$

However, F_{12} can be estimated with the expression:

$$-\frac{1}{2}(F_{11}F_{22})^{1/2} \leq F_{12} \leq 0 \tag{2.9}$$

Because the Tsai-Wu criterion takes into account the interaction between different stress components it is usually better than other simpler criteria and agrees with experimental testing [26].

2.3 Aerodynamic Analysis

There are two types of aerodynamic analyses employed in this project.

A low fidelity calculation based on Prandtl's Lifting Line Theory (LLT) of the aerodynamic loads is used for the structural simulations during the optimization process. Prandtl's LLT is a simple solution for analyzing the aerodynamic behavior of unswept 3D wings with no dihedral and an aspect ratio $AR \geq 4$. Taking into account the twist and chord variation along the span, this theory is a good approximation when dealing with incompressible, inviscid, and steady flow problems [29].

High fidelity CFD analyses are used with the software *ANSYS CFX* for the aerodynamic characterization of the aircraft.

2.3.1 Computational Fluid Dynamics

Ansys CFX is a CFD software based on the Finite Volume Method (FVM), which is a numerical technique that discretizes the geometric domain in non-overlapping elements or finite volumes that form a three-dimensional mesh. The integration of the differential equations in each element into algebraic equations allows for the solution of the system. In FVM the face fluxes between adjacent volumes are identical making it a strictly conservative method [30].

The governing equations in *Ansys CFX* are the unsteady Navier-Stokes Equations which describe the conservation of mass, momentum in the three directions, and energy. This group of equations accurately describes laminar and turbulent flow but solving them would require computational power not available today. Turbulence models are used to predict the effects of turbulence without needing very fine meshes, making them very common in CFD research today [31, 32].

The turbulence model used for this project was the Shear Stress Transport (SST) which is a two-equation eddy-viscosity model. It introduces two additional transport equations, one for the turbulent kinetic energy k and another for either the turbulent dissipation ϵ or the turbulent frequency ω. Each combination stems two different models, the $k-\epsilon$ or the $k-\omega$ respectively.

For the inner region of the boundary layer it takes advantage of the robustness of the $k-\omega$ model but to bypass its problems in the free shear flow region it transitions to the $k-\epsilon$ which is more independent of the boundary layer in the outer regions. By also adding a term to take into account the turbulent shear stress it can give more accurate results and better predict flow separation under adverse pressure gradients [30–32]

2.4 Fluid-Structure Interaction

The numerical procedures to solve FSI problems can be mainly classified into two categories. The first is the monolithic approach which couples the fluid and structure dynamics into the same mathematical framework to form a complete system of nonlinear algebraic equations. This may result in more accurate results but demands complete control of the implementation code which may require more resources and expertise. On the other hand, a partitioned approach treats the fluid and the structure as two independent computational fields solved separately with their own mesh discretization and numerical algorithm and coupled via interfacial conditions that communicate information between the two solutions. This allows for the use of existing single-physics solvers like commercial software which can reduce code development time but can also stem for a slow solution convergence [19, 20].

FSI solution procedures can also be classified with respect to their meshes. The conforming mesh method treats the interface location as part of the solution because the interface conditions are also boundary conditions. This means that the mesh must conform to the interface, hence the name. Movement of the interface position requires re-meshing or mesh updating to continue with the solution. In contrast, non-conforming mesh methods handle the boundary location and the associated interface conditions as constraints forced on the model equations. This allows for the fluid and structure equations to be solved separately and with independent grids through the use of non-conforming meshes, where re-meshing is not necessary. The difference between these two procedures can be seen in figure 2.1. Most partitioned approaches like the one used in this thesis use conforming mesh methods while the non-conforming mesh method is more present in newer FSI developments with immersed methods [19].

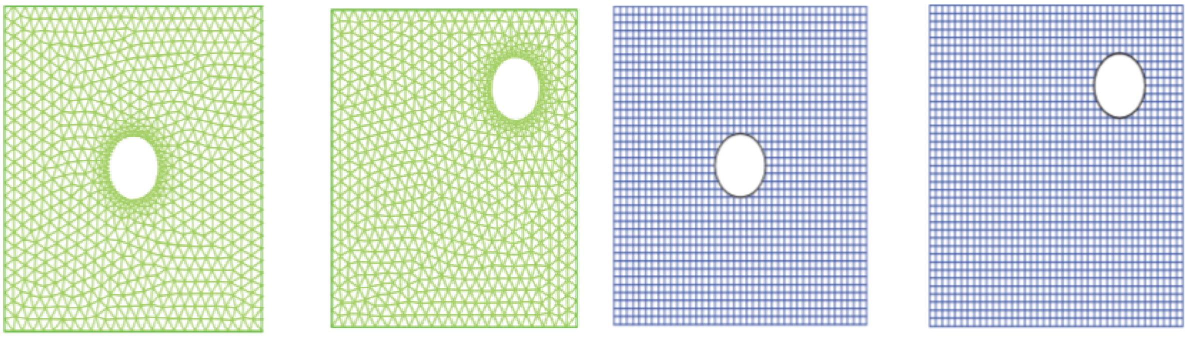

(a) Conforming mesh. Left: $t = t_1$; Right: $t = t_2$.

(b) Non-conforming mesh. Left: $t = t_1$; Right: $t = t_2$.

Figure 2.1: Examples of conforming mesh (a) and non-conforming mesh (b) [19].

The FSI simulations in this project will be made through *Ansys Workbench* by coupling the previously mentioned CFD capabilities of *Ansys CFX* with the structural analysis of *Ansys Mechanical*.

2.5 Flight Dynamics

Flight Dynamics is the study of the movement of an aircraft through the air and how the forces acting on the vehicle influence its velocity and attitude through time. The first parameter to be established is the convention for the body frame and the Earth frame. The body frame's origin is in the center of gravity of the aircraft with the x-axis pointing forwards, the y-axis pointing right, and the z-axis pointing downwards. The Earth fixed inertial frame uses the North-East-Down (NED) convention. Both reference frames can be found in figure 2.2.

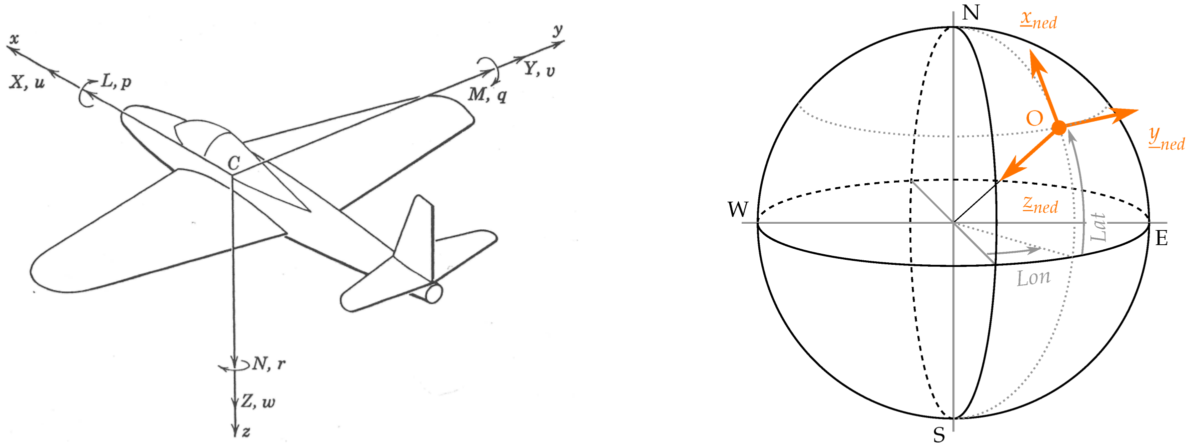

(a) Body reference frame [33].

(b) Earth reference frame [34].

Figure 2.2: Conventions used for the body and earth reference frames.

The transformation between both reference frames uses the Euler angles $\Phi = (\phi, \theta, \psi)$ where ϕ is the roll angle, θ the pitch angle and ψ the yaw angle. The matrix to transform a vector from the Earth reference frame to the body reference frame is given by:

$$S = \begin{bmatrix} \cos\theta\cos\psi & \cos\theta\sin\psi & -\sin\theta \\ \sin\phi\sin\theta\cos\psi - \cos\phi\sin\psi & \sin\phi\sin\theta\sin\psi + \cos\phi\cos\psi & \sin\phi\cos\theta \\ \cos\phi\sin\theta\cos\psi + \sin\phi\sin\psi & \cos\phi\sin\theta\sin\psi - \sin\phi\cos\psi & \cos\phi\cos\theta \end{bmatrix} . \tag{2.10}$$

The transformation in the opposite direction uses the transpose of matrix S, S^T.

The dynamic equations of the rigid aircraft are obtained from the Newton-Euler equations for linear and angular momentum which in the body reference frame are:

$$m\left(\frac{d}{dt}V + \Omega V - Sg\right) = F \,, \tag{2.11a}$$

$$I\frac{d}{dt}\omega + \Omega I\omega = M \,, \tag{2.11b}$$

where m is the aircraft mass, $V = [U, V, W]^T$ is the air velocity $\omega = [P, Q, R]^T$ is the angular velocity, g is the gravity constant, $F = [X, Y, Z]^T$ is the external force which includes both aerodynamic and propulsion forces, I is the inertia matrix, $M = [L, M, N]^T$ is the external moment which also includes the aerodynamic and propulsion forces and Ω is the matrix form of the cross product $\omega\times$ given by:

$$\Omega = \begin{bmatrix} 0 & -R & Q \\ R & 0 & P \\ -Q & P & 0 \end{bmatrix} . \tag{2.12}$$

These equations need to be linearized in order to progress further which is done by using the small perturbation theory. In this theory, any variable X can be expressed as the sum of an equilibrium term X_0 plus a perturbation term x considerably smaller than the first one, $X = X_0 + x$. In this case, the equilibrium condition is the trimmed flight condition and x refers to small perturbations around that equilibrium state. The linearization of forces assumes that both lateral and longitudinal motions are uncoupled, *i.e.*, lateral forces and moments depend only on lateral variables and the same for the longitudinal forces and moments. Thus, the forces and moments can be linearized as:

$$F = F_i x_i \,, \quad F_i = \frac{1}{m}\frac{\partial F}{\partial i} \,, \tag{2.13a}$$

$$M = M_i x_i \,, \quad M_i = \frac{1}{I_i}\frac{\partial M}{\partial i} \,, \tag{2.13b}$$

where F_i and M_i are the stability derivatives, x_i is the perturbation for the variable i and I_i is the inertia moment term respective to the moment being calculated.

Combining the linearized equations with the equations of motion (EOM) one gets the system of equations:

$$\begin{cases} \dot{u} + qW_0 + g\cos(\theta_0)\theta = X_u u + X_w w + X_{\delta_{i_c}}\delta_{i_c} + X_{\delta_T}\delta_T \\ \dot{w} + qU_0 + g\sin(\theta_0)\theta = Z_u u + Z_w w + Z_{\delta_{i_c}}\delta_{i_c} + Z_{\delta_T}\delta_T \\ \dot{q} = M_u u + M_w w + M_{\dot{w}}\dot{w} + M_q q + M_{\delta_{i_c}}\delta_{i_c} + M_{\delta_T}\delta_T \end{cases} , \tag{2.14}$$

$$\begin{cases} \dot{v} + rU_0 - pW_0 - g\cos(\theta_0)\phi = Y_v v + Y_p p + Y_r r + Y_{\delta_R}\delta_R \\ \dot{p} - \frac{I_{xz}}{I_{xx}}\dot{r} = L_v v + L_p p + L_r r + L_{\delta_A}\delta_A + L_{\delta_R}\delta_R \\ \dot{r} - \frac{I_{xz}}{I_{zz}}\dot{p} = N_v v + N_p p + N_r r + N_{\delta_A}\delta_A + N_{\delta_R}\delta_R \end{cases} , \tag{2.15}$$

where θ_0 is the equilibrium angle of pitch and δ refers to the input values for the control surfaces (i_c - canard, A - ailerons, R - rudder) and the engine (T) [35].

The equations for the stability derivatives are present in Appendix A.

2.5.1 State Space Formulation

A space state is used to evaluate the aircraft's dynamic modes. For a Linear Time-Invariant (LTI) system, this formulation can be written as the following first-order differential equation:

$$\dot{x} = Ax + Bu \,, \tag{2.16}$$

where x is the state vector, A is the state matrix, B is the input matrix and u is the input vector. To obtain equations 2.14 and 2.15 in this form some manipulation needs to be done that results in the matrix equations 2.17 and 2.18 for the longitudinal and lateral movements respectively.

$$\dot{x} = \begin{bmatrix} X_u & X_w & -W_0 & -g\cos(\theta_0) \\ Z_u & Z_w & U_0 & -g\sin(\theta_0) \\ M_u + M_{\dot{w}} Z_u & M_w + M_{\dot{w}} Z_w & M_q + M_{\dot{w}} U_0 & -g\sin(\theta_0) M_{\dot{w}} \theta \\ 0 & 0 & 1 & 0 \end{bmatrix} x + \begin{bmatrix} X_{\delta_{i_c}} & X_{\delta_T} \\ Z_{\delta_{i_c}} & Z_{\delta_T} \\ M_{\delta_{i_c}} & M_{\delta_T} \\ 0 & 0 \end{bmatrix} u \,, \tag{2.17}$$

where the state vector is $x = [u, w, q, \theta]^T$ and the input vector is $u = [\delta_{i_c}, \delta_T]^T$.

$$\dot{x} = \begin{bmatrix} Y_v & Y_p + W_0 & Y_r - U_0 & g\cos(\theta_0) \\ L'_v & L'_p & L'_r & 0 \\ N'_v & N'_p & N'_r & 0 \\ 0 & 1 & tan(\theta_0) & 0 \end{bmatrix} x + \begin{bmatrix} Y_{\delta_A} & Y_{\delta_R} \\ L'_{\delta_A} & L'_{\delta_R} \\ N'_{\delta_A} & N'_{\delta_R} \\ 0 & 0 \end{bmatrix} u \,, \tag{2.18}$$

where the state vector is $x = [v, p, r, \phi]^T$, the input vector is $u = [\delta_A, \delta_R]$ and the derivatives L'_i and N'_i are given by [35]:

$$\begin{cases} L'_i = L_i + \frac{I_{xz}}{I_{xx}} N_i \\ N'_i = N_i + \frac{I_{xz}}{I_{zz}} L_i \end{cases} . \tag{2.19}$$

2.5.2 Dynamic Modes

Each motion has multiple dynamic modes and each mode is characterized by its eigenvalue or poles. The eigenvalues λ are the solutions to the equation:

$$\det(A - \lambda I) = 0 \,, \tag{2.20}$$

where I is the identity matrix with the same dimensions as A.

These eigenvalues can be broken down into the damping coefficient ζ and natural frequency ω. By writing them as $\lambda = n \pm i\omega$ one can get the natural frequency:

$$\omega_n = \sqrt{\omega^2 + n^2} \,, \tag{2.21}$$

and the damping coefficient:

$$\zeta = -\frac{n}{\omega_n}\,. \tag{2.22}$$

The longitudinal motion has two modes, each represented by a complex pair of poles. The phugoid is a slow mode with low damping characterized by big oscillations in the longitudinal velocity and altitude through an exchange between kinetic energy and potential energy. On the other hand, the short-period is a faster mode with higher damping where the variation of the angle of attack is predominant when compared to the other variables.

The lateral motion has three modes. The spiral mode is characterized by a single and often unstable pole related to an increase in roll angle and speed. The Dutch roll is usually characterized by a fast and slightly damped complex pair of poles where all lateral variables contribute to the motion. The final mode is the roll which is a fast stable and highly damped single-pole where the predominant variable is the roll angle.

For an aircraft to be dynamically stable it has to be stable in both the longitudinal and lateral motions, which means that all the eigenvalues of the previously mentioned modes have to have a negative real part [36].

2.6 Modal Analysis

Modal analysis deals with the dynamic characteristics of mechanical structures and with the identification of their natural frequencies and mode shapes. Structures vibrate and deform in specific mode shapes when excited at their natural frequencies. If the excitation does not match a natural frequency then the resulting deformation will be a combination of the all mode shapes.

The identification of the mode shapes happens through the measurement of the Frequency Response Functions (FRFs) at multiple locations that, when combined, describe the frequency response of the entire structure which can be used to formulate a modal model for studying its dynamic behavior. Although real structures have Multiple Degrees of Freedom (MDOF) and are non-linear, they can normally be approximated as a group of Single Degree of Freedom (SDOF) systems [37, 38].

2.6.1 Eigenvalues and Eigenvectors

The Eigenvalues and Eigenvectors that characterize a system can be derived from Newton's equation. In the general damping case, this equation has the following form:

$$M\ddot{u}(t) + C\dot{u}(t) + Ku(t) = f(t)\,, \tag{2.23}$$

where M is the mass matrix, K is the stiffness matrix, C is the damping matrix, $\ddot{u}(t)$, $\dot{u}(t)$ and $u(t)$ are the acceleration, velocity and displacement vectors, and $f(t)$ is the vector of externally applied forces. This equation can be rewritten in a simplified state-space form like:

$$A\dot{x} + Bx = F\,, \tag{2.24}$$

where

$$A = \begin{bmatrix} C & M \\ M & 0 \end{bmatrix}\,, \tag{2.25a}$$

$$B = \begin{bmatrix} K & 0 \\ 0 & -M \end{bmatrix}\,, \tag{2.25b}$$

$$F = \begin{Bmatrix} f(t) \\ 0 \end{Bmatrix}\,, \tag{2.25c}$$

$$\begin{cases} x = [u(t)^T\, \dot{u}(t)^T]^T \\ \dot{x} = [\dot{u}(t)^T\, \ddot{u}(t)^T]^T \end{cases}\,. \tag{2.25d}$$

A first order differential equation can be identified from equation 2.24 whose generalized family of solutions can be expressed as:

$$x = \phi e^{\omega t} = \begin{Bmatrix} \phi \\ \lambda\phi \end{Bmatrix} e^{\omega t}\,. \tag{2.26}$$

By equaling F to zero in equation 2.24 one can get the free vibrations of the system and by applying the Laplace Transform one gets:

$$\det(sA + B)X(s) = 0\,. \tag{2.27}$$

By multiplying both sides of equation 2.27 by A^{-1} and by equaling $s = -\lambda$ it is possible to obtain the solution for the eigenvalues and eigenvectors. Because both A and B are real matrices, the eigenvalues must be either real, in which case the system is overdamped, or a complex pair of poles that represent free vibration which is the focus of modal analysis.

The eigenvalue of the complex pole pair that has a positive imaginary part can be defined as:

$$s_j = -\zeta_j\omega_j + i\omega_j\sqrt{1-\zeta_j^2}\,, \tag{2.28}$$

where ζ_j is the damping coefficient and ω_j is the angular natural frequency. The natural frequency f_j can be obtained from the expression $f_j = \frac{\omega_j}{2\pi}$ [39].

The computational analysis in this thesis was made using the *Ansys Mechanical* software. In this case, there is no damping and the Laplace Transformation can be simplified to solve the equation:

$$\det(K - \lambda M) = 0\,. \tag{2.29}$$

The poles of each mode will then have the form:

$$s_j = \pm i\sqrt{\lambda} = \pm i\omega_j \, . \tag{2.30}$$

2.7 Ground Vibration Tests

One of the experimental tests that aid in the realm of aeroservoelasticity is Ground Vibration Testing (GVT). These tests serve to experimentally measure the aircraft structural vibration modes which can be used to adjust FEM models for further analysis like calculating aeroelastic instability phenomena [40].

GVT works by measuring the acceleration response of the structure relative to the force excitation applied to the aircraft which will be recorded as FRFs.

2.7.1 Impact Testing

The type of excitation used in the experimental part of this project is through an impact hammer. This is a type of excitation that is very convenient and cheap when compared to other methods because of the small amount of hardware it requires. It works by recording the force from hitting the structure with an impedance head. Different tip hardness and different masses can be used to excite different frequency ranges and input different amounts of energy into the system.

Another way of exciting a system in GVT is through the use of a shaker that is mounted to the structure and resonating it at different frequencies. Although this is also an option, the complexity is much higher and the availability of the impact hammer determined the excitation method [41].

2.7.2 Roving Hammer vs Roving accelerometer

Since the cost of the sensors used in GVT is high, the number of degrees of freedom is often bigger than the number of sensors available to do the test. There are two options to overcome this obstacle. The first one involves roving the excitation source while keeping the sensor in the same position, measuring the same degrees of freedom. The other means always exciting the same location while moving the sensor location. From an analysis viewpoint, the results will be the same so the practicality of each technique will dictate which one is used. Since moving the sensors would be more time demanding the roving hammer approach was chosen [41].

Chapter 3

Multidisciplinary Design Optimization

3.1 Optimization Tool

The optimization tool and process was built and defined by Tiago Jesus [5] but it had not yet converged as of the beginning of this thesis work. For this reason, any substantial change could not be implemented as that would require restarting the optimization process. This chapter will summarize all the important details about the process and the final results obtained as part of this project's work.

3.2 Problem Formulation

3.2.1 Mission Requirements

To formulate the optimization problem, define the objective function and set constraints, it is necessary to establish the requirements of the aircraft and the mission.

Being the DRDC the client of this project, their demands have the highest priority. With them in mind, there were other requirements made by the CfAR team in regards to testing and legislation. Finally, there were also some conditions defined by Bruno Luís' analysis [4]. The relevant information for this design process is the following:

1. Payload: the payload of this aircraft will be the MAD sensor and the electrical power supplies required for the correct functioning of the sensor. Its position must be such that the distances to engines and strong electrical currents do not affect the magnetic detection. This is what led to the decision to use a canard configuration as the payload will be in the front of the aircraft as far away as possible from most of the electrical components which are in the back;
2. Speed and Wind: The aircraft must be capable of following a submarine that is traveling in the direction of the wind. Being the record speed for a submerged submarine a claimed 23 m/s by the soviet K-222 Papa class, nuclear-powered submarine [42] and the average surface winds approximately 12 m/s, the cruise speed V_{cruise} was set to 35 m/s. Considering V_{cruise} and that the stronger wind gusts in the Artic rarely exceed 25 m/s, the dash speed was set to 60 m/s;

3. MTOM: The current Canadian legislation on non-recreational UAV system operations states that if the Maximum Take-Off Mass (MTOM) does not exceed 25 kg, there is an exemption from the requirement to obtain a Special Flight Operations Certificate (SFOC). Because this facilitates building and flying the aircraft for testing at CfAR, 25 kg was set as the MTOM of the aircraft;

4. Maximum operational Load Factor: The maximum acceleration the aircraft was set to withstand is $3g$. This was decided during team meetings, as it is a typical value for general aircraft;

5. Stability: The static margin (K_n) was defined as being 10% of the mean aerodynamic chord and the vertical tail volume coefficient (C_{VT}) was settled at 0.02 also by the CfAR team during Bruno Luis' thesis due to stability reasons.

3.2.2 Objective Function

The ultimate objective of the optimization problem is to maximize range. The Breguet equation shown below allows an estimation of the range for propeller aircraft:

$$R = \frac{\eta}{g}\frac{L/D}{BSFC}\ln\left(\frac{m_i}{m_f}\right) , \tag{3.1}$$

where η is the propeller efficiency, g is the acceleration of gravity, L/D is the lift to drag ratio, m_i is the initial mass, m_f is the final mass at the end of the mission segment and $BSFC$ is the brake specific fuel consumption which is defined as the mass flow rate of fuel per unit of engine output power and it is measured in kg/(W.s). Because m_i and the payload mass are assumed to be constant in this study, savings in structural mass will result in a bigger range due to increased fuel capacity.

The propulsion system for this aircraft is not yet defined so instead of using equation 3.1 as the objective function, a multi-objective optimization including L/D and the structural mass m_S is formulated. Through the use of the weighted sum method, it is possible to evaluate the variation of range relative to a reference aircraft configuration. By approximating the range as varying linearly with L/D and m_S we get the following expression [43]:

$$\frac{\Delta R}{R_{ref}} = \frac{1}{R_{ref}}\frac{\delta R}{\delta(L/D)}\Delta(L/D) + \frac{1}{R_{ref}}\frac{\delta R}{\delta(m_S)}\Delta(m_S)\,. \tag{3.2}$$

The derivatives can be obtained from the original range equation 3.1 which results in:

$$\frac{\Delta R}{R_{ref}} = \frac{\Delta(L/D)}{(L/D)_{ref}} - \frac{\ln\left(1+\frac{m_{S_{ref}}}{m_{f_{ref}}}\right)}{\ln\left(\frac{m_i}{m_{f_{ref}}}\right)}\frac{\Delta m_S}{m_{S_{ref}}}, \tag{3.3}$$

where $\Delta(L/D) = (L/D) - (L/D)_{ref}$ and $\Delta m_S = m_S - m_{S_{ref}}$.

For the first reference configuration, it was assumed that the structural mass was 50% of the empty aircraft weight m_f. For the next iterations, the non-structural component of that mass was kept constant. If the analysis of a new configuration reveals it is feasible and better than the reference, then $m_{S_{ref}}$ and $m_{f_{ref}}$ are updated to the values of that configuration.

Because the goal is to maximize range but the objective function will be minimized, the symmetric of equation 3.3 is the function provided to the optimizer.

3.2.3 Design Variables and Parametrization

Each design point includes geometric, aerodynamic, and structural variables. These are used to build aerodynamic and structural models in order to evaluate the lift to drag ratio in cruise and structural mass of the aircraft. Their parametrization is described in this section.

The wing planform is defined using span (b_w), leading edge sweep angle (Λ_w) and bilinear chord and twist distributions defined with four parameters each (c_{root_w}, c_{disc_w}, c_{tip_w}, $y_{c_{disc}}$ and $\gamma_{w_{root}}$, $\gamma_{w_{disc}}$, $\gamma_{w_{tip}}$, $y_{\gamma_{w_{disc}}}$). The relative thickness (t_w) and camber (cbr_w) of the wing airfoil are also variable parameters. The thickness distributions of the wing spars and skin are also defined by three parameters each ($thk_{tip_{spar}}$, $thk_{disc_{spar}}$, $thk_{root_{spar}}$ and $thk_{tip_{skin}}$, $thk_{disc_{skin}}$, $thk_{root_{skin}}$). The chordwise position of the aft spar of the wing is fixed as 70% of the local chord while the position of the front spar can vary between 10% and 25%, making it another design variable ($pos_{f_{spar}}$).

The trapezoidal winglet geometry parameterization includes span (b_{wglt}), taper ratio (λ_{wglt}), and winglet sweep (Λ_{wglt}) as variable parameters. Relative thickness (t_{wglt}) and camber (cbr_{wglt}) of the winglet airfoil are also design parameters.

The canard planform is rectangular with a variable area dependent on the wing area (S_c) and span (b_c). The camber of the canard airfoil is another variable parameter in the design (cbr_c), while the thickness is fixed at 12%. The canard support structure is a constant thickness tube whose radius (r_{tube}) and thickness (thk_{tube}) values are design parameters.

The vertical fin is defined by its root chord (c_{root_f}), taper ratio (λ_f), and span (b_f). It has the symmetric airfoil NACA0010 and only one spar located at 70% of its chord.

All airfoils are defined by the NACA 4-digit airfoil parameterization [128] with the max camber position at 40% of the chord.

Longitudinal and vertical distance (l_c and z_c) between the wing and canard aerodynamic centers are also variable and define the lifting surfaces completely in the configuration.

The fuselage structure is composed of two parallel and identical laminate spars with constant thickness. Each spar has two holes to encapsulate the canard and wing structures. The Outer Mold Line (OML) of the fuselage was designed by [4] with the MAD sensor on the nose of the aircraft in mind. This shape is kept constant even after the MDO process is complete. The last variables in the design of the aircraft are the thickness of the fuselage spars (thk_{fuse}) and spanwise and transverse scaling factors (y_{scale} and z_{scale}) to the fuselage shape.

Table 3.1 lists all the design variables including the upper and lower bounds.

Certain constraints were included when choosing the bounds for these design variables to make sure that the payload fits inside the fuselage (by now allowing the fuselage to be scaled down) and that the canard stalled before the wing (by limiting the canard area to 25% of the wing area, even though this is not enough to fully guarantee that the canard stalls first).

Table 3.1: Design variables with correspondent lower and upper bounds and respective units.

Variable	L.B.	U.B.	Variable	L.B.	U.B.
y_{scale} [-]	1	1.05	$\gamma_{w_{tip}}$ [°]	$\gamma_{w_{disc}} - 3$	$\gamma_{w_{disc}}$
z_{scale} [-]	1	1.05	$y_{\gamma_{w_{disc}}}$ [m]	$0.3b_w/2$	$0.7b_w/2$
thk_{fuse} [m]	0.002	0.005	Λ_w [°]	0	30
r_{tube} [m]	$0.2c_ct_c$	$0.9c_ct_c$	t_w [-]	0.1	0.15
thk_{tube} [m]	$0.2r_{tube}$	r_{tube}	cbr_w [-]	0	0.07
$pos_{f_{spar}}$ [m]	$0.1c(y)$	$0.25c(y)$	b_{wglt} [m]	0.05	0.2
$thk_{tip_{spar}}$ [m]	8×10^{-4}	1.5×10^{-3}	λ_{wglt} [-]	0.2	0.6
$thk_{disc_{spar}}$ [m]	8×10^{-4}	3×10^{-3}	Λ_{wglt} [°]	0	30
$thk_{root_{spar}}$ [m]	1×10^{-3}	5×10^{-3}	t_{wglt} [-]	0.08	0.12
$thk_{tip_{skin}}$ [m]	6×10^{-4}	1.5×10^{-3}	cbr_{wglt} [-]	0	0.02
$thk_{disc_{skin}}$ [m]	6×10^{-4}	2×10^{-3}	b_c [m]	1	2
$thk_{root_{skin}}$ [m]	6×10^{-4}	3×10^{-3}	S_c [m^2]	$0.15S_w$	$0.25S_w$
b_w [m]	2.3	4	l_c [m]	1.5	3.5
c_{root_w} [m]	0.15	0.5	z_c [m]	pos^1_{bot}	pos^1_{top}
c_{disc_w} [m]	0.1	c_{root_w}	cbr_c [-]	0	0.07
c_{tip_w} [m]	0.1	c_{disc_w}	c_{root_f} [m]	0.1	0.2
$y_{c_{disc}}$ [m]	$0.3b_w/2$	$0.7b_w/2$	λ_f [-]	0.2	0.6
$\gamma_{w_{root}}$ [°]	-3	10	b_f [m]	0.2	0.4
$\gamma_{w_{disc}}$ [°]	$\gamma_{w_{root}} - 3$	$\gamma_{w_{root}}$			

[1] pos_{top} and pos_{bot} correspond to the most top and bottom positions on the fuselage spar with a safety margin for placing the canard.

As mentioned previously in 3.2.1, the vertical tail volume coefficient was set to 0.02 for stability reasons which determines the longitudinal position of the vertical fin.

The only constraint that requires evaluating the results is the structural failure criterion at the ultimate load case scenario. Due to the $3g$ operational requirement, $4.5g$ was used as the ultimate vertical load factor for the structural analysis. Because the aircraft will be made out of CFRP, the Tsai-Wu criterion explained earlier in section 2.2.2 is used. The feasible design region will be where the Tsai-Wu failure index is smaller than 1.

3.3 MDA Procedure

There are two disciplines in the MDA of this thesis, structures and aerodynamics.

The analysis can be split into the following steps:

1. Generation of the structural geometry based on the inputs for the design variables;
2. LF estimation of the aerodynamic loading on the lifting surfaces (wing and canard) based on Prandtl's LLT;
3. Structural FEM analysis using the previously calculated aerodynamic loads to determine the structural mass and evaluate structural integrity;
4. If the structure is feasible then the OML for the HF aerodynamic simulations is created;
5. HF CFD analyses are performed to determine both trim and stability conditions and to gather performance results.

3.4 Geometric Models

The structural model is created in *Ansys Mechanical APDL*. Besides the geometric dimensions, it is also necessary to provide the material properties of each section. As mentioned previously, the structure is made of CFRP, either unidirectional (UD) carbon-epoxy or bidirectional woven carbon-epoxy. The properties for both these laminates are available in table 3.2.

Table 3.2: Carbon fiber material properties. Negative signs correspond to compressive limits.

	UD Carbon-Epoxy	Woven Carbon-Epoxy
ρ [kg/m^3]	1449.1	1422.9
E_x [MPa]	1.17$\times 10^5$	67100
E_y [MPa]	6070	67100
E_z [MPa]	6070	7500
ν_{xy} [-]	0.3	0.05
ν_{yz} [-]	0.42	0.3
ν_{xz} [-]	0.3	0.3
G_{xy} [MPa]	3100	4000
G_{yz} [MPa]	1600	1600
G_{xz} [MPa]	3100	4000
$\sigma_{x_{max}}$ [MPa]	1453	711
$\sigma_{x_{min}}$ [MPa]	-368	-356
$\sigma_{y_{max}}$ [MPa]	39.6	711
$\sigma_{y_{min}}$ [MPa]	-45	-356
$\sigma_{z_{max}}$ [MPa]	39.6	50
$\sigma_{z_{min}}$ [MPa]	-45	-150
$\tau_{xy_{max}}$ [MPa]	41	54
$\tau_{yz_{max}}$ [MPa]	40	39
$\tau_{xz_{max}}$ [MPa]	40	39
h_n [mm]	0.165	0.208

All spars are made of woven layers, with the fuselage having a minimum of 10 layers, the wing plus winglet spars a minimum of 4, and the vertical tail spar a fixed number of 5. The canard tube is made out of UD carbon with a minimum of 6 layers.

The wing skin has a minimum number of 3 woven layers and both UD and woven can be added in the middle of the laminate according to the sequence +Woven $\rightarrow$ +UD $\rightarrow$ +UD $\rightarrow$ +Woven in order to keep an always symmetric stacking sequence. The winglet skin and the vertical fin have a fixed number of 3 woven layers.

The OML of the entire aircraft for the aerodynamic analysis is generated using *SOLIDWORKS*.

Figures 3.1(a) and 3.1(b) show a structural model example and an OML example respectively.

3.4.1 Structural Analysis

Two FEM simulations are necessary to calculate the structural weight and the Tsai-Wu failure index. In the first simulation, half of the structural geometry is imported with boundary conditions applied to the nodes in the symmetry plane, namely zero displacement in the pitch axis direction, as well as zero rotation in the roll and yaw axes. The material properties and the composite stacking of each section are also defined. Two elements are used, 'SHELL181' and 'MPC184'. The first is used as the

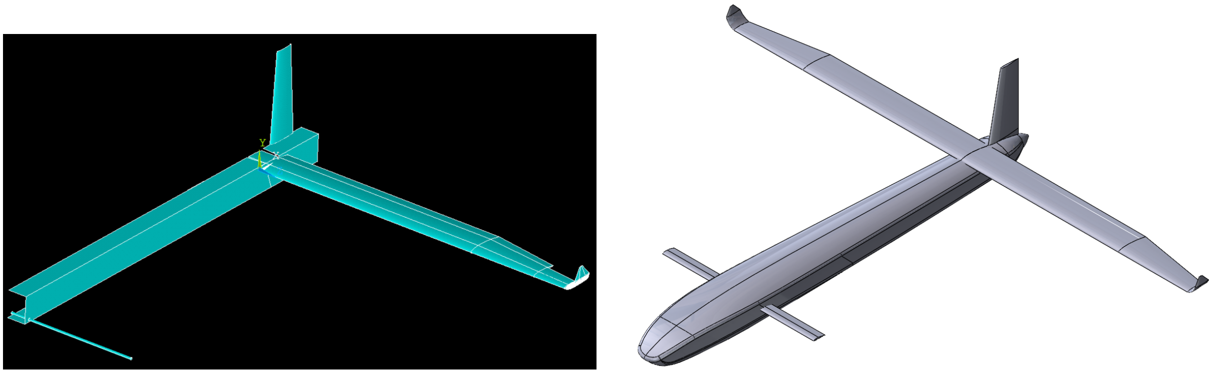

(a) *Ansys APDL* structural model.

(b) *SOLIDWORKS* OML.

Figure 3.1: Examples of the structural model and OML of a configuration.

structural elements of the laminates, while the second is used for the connections between the different components of the structure. The finite element model of each structure has approximately 45000 elements.

From the first analysis, the mass of the structure and its CoG position are recorded and used to calculate the mass and position of the CoG of a mass point that brings the total mass of aircraft to the expected value with a correct position for the CoG based on the trim conditions calculated previously.

With this information, the second simulation with the 4.5g load is calculated and the Tsai-Wu criteria is evaluated for the whole aircraft. The maximum value is saved to add to the surrogate model of this constraint.

3.4.2 CFD analysis

ANSYS CFX is used to perform the HF aerodynamic analysis, which uses the OML model uploaded from *SOLIDWORKS*.

A mesh convergence study was performed by Tiago Jesus [5]. The parameters varied were the maximum element size for both the UAV and the air domain, the growth rate, and the curvature normal angle for the elements on the surface of the aircraft. The mesh was considered converged for an approximate number of 5.3 million tetrahedral elements, with an aircraft maximum element size of 0.008 m, an airflow maximum element size of 0.45 m, a growth rate of 1.2, and a curvature normal angle of $10°$. The flow domain is a rectangular parallelepiped with a length of 10 times the fuselage length, a width of 5 times the wingspan and a height of 16 mean aerodynamic chords where the front face is 3 fuselage lengths away from the nose of the aircraft. Figures 3.2(a) and 3.2(b) show the mesh domain and the mesh elements around an aircraft for an example configuration. These mesh settings will be used throughout the rest of the project.

There are 5 steps to evaluate the aerodynamic performance for the trimmed flight condition at cruise speed:

1. The first simulations are run with a $0°$ canard incidence angle (i_c) and for three different angles of attack. Taking the C_L and C_m coefficients for the three analyses it is possible to esti-

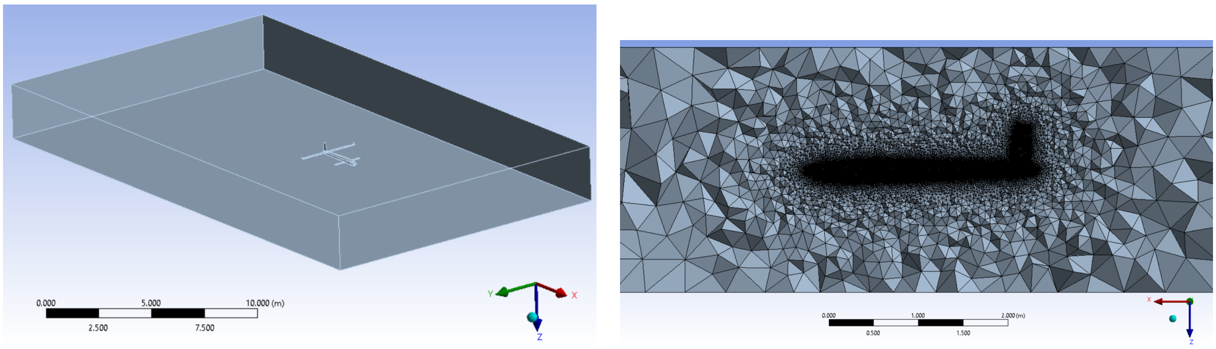

(a) Mesh domain.

(b) Mesh elements around aircraft.

Figure 3.2: Mesh domain and mesh elements around aircraft for an example configuration.

mate the neutral point position and subsequently the corrected CoG position using the expression $dC_m/d\alpha = -(dC_L/d\alpha)K_n$ with a static margin of 10% [36].

2. The C_m values of the three previous simulations are updated with the new CoG position.

3. A simulation with $i_c = -2°$ is calculated in order to get the derivatives dC_L/di_c and dC_m/di_c. These derivatives are used to estimate the i_c angle that trims the aircraft for $\alpha = 0°$.

4. Three more simulations with the new i_c estimation are used to recalculate the values of $dC_L/d\alpha$, $dC_m/d\alpha$, $C_{L_{\alpha=0}}$ and $C_{m_{\alpha=0}}$ for this i_c. This allows for a better linearization around the trim condition.

5. By solving the system of equations 3.4 it is possible to determine the value of the variables $\Delta i_{c_{trim}}$ (which is the difference between the trim condition and the i_c from step 4) and α_{trim} which gives the correct trim condition. One last CFD simulation is done to validate the trim condition and retrieve the value of L/D.

$$\begin{cases} C_{L_{trim}} = \frac{dC_L}{d\alpha}\alpha_{trim} + \frac{dC_L}{di_c}\Delta i_c + C_{L_{\alpha=0}} \\ C_{m_{trim}} = \frac{dC_m}{d\alpha}\alpha_{trim} + \frac{dC_m}{di_c}\Delta i_c + C_{m_{\alpha=0}} \end{cases} . \tag{3.4}$$

3.5 MDO Methodology

3.5.1 Surrogate Models

Three Kriging-based stochastic surrogate models built with the DACE MATLAB toolbox were used for an approximation of the problem at hand. Two were generated using all 37 design variables from the structural data. One models the constraint value corresponding to the Tsai-Wu failure index and the other one the structural mass. The third model is relative to the aerodynamic data, so only 27 design variables were used as the 10 other ones were only structural. This model estimates the aerodynamic lift to drag ratio.

3.5.2 Search Algorithm

Tiago Jesus performed a comparison of all eight search functions implemented in the optimization tool [5]. Based on his results, he gave priority to the predictions made by the WB2 and WB2S methods. However, in this thesis work, as the optimization reached convergence, all methods predicted worse results than the best reference configuration except for the prediction-based exploration. For this reason, most of the final iterations obtained from the optimization tool resulted from this method.

The GA function used is also available in *MATLAB*. It was set to a maximum number of 50 generations, a population size of 400 individuals, and function and constraint tolerances both of 1×10^{-8}. The initial population corresponded to all the feasible samples at each iteration.

3.6 Optimization Results

The optimization was already underway when this thesis work started. Before the surrogate models were created, there were 8 fully evaluated configurations and the best one was considered the initial reference. It had the following properties:

- $m_{S_{ref}} = 9.731$ kg;
- $m_{f_{ref}} = 19.462$ kg;
- $L/D = 13.6$.

Tiago Jesus fully evaluated 33 different configurations for his thesis work. The design point with the best performance he achieved had the following properties:

- $m_{S_{ref}} = 4.209$ kg;
- $m_{f_{ref}} = 13.940$ kg;
- $L/D = 16.6$.

This means that the range of this configuration was 2.85 times greater than the original reference configuration.

However, the optimization had not yet fully converged. For this thesis work 39 more fully analyzed design points were studied for a total number of 72 iterations. Out of those 39, 12 were introduced by the author to help the exploration of the design space get configurations with better range.

Figures 3.3, 3.4, and 3.5 plot the evolution of the L/D, m_S, and the Tsai-Wu failure index along the optimization. The initial samples are represented by the crosses on the negative side of the horizontal axis, the configurations coming from the GA are labeled as the black circles while the configurations defined by the author are plotted as the hollow circles.

At the beginning of the optimization, there was a general upwards trend in the L/D values. Some failed attempts are present like iterations 21 and 28 but the trend still remained. Between iterations 29 and 38 some stagnation started to happen. This was combated by the introduction of five configurations

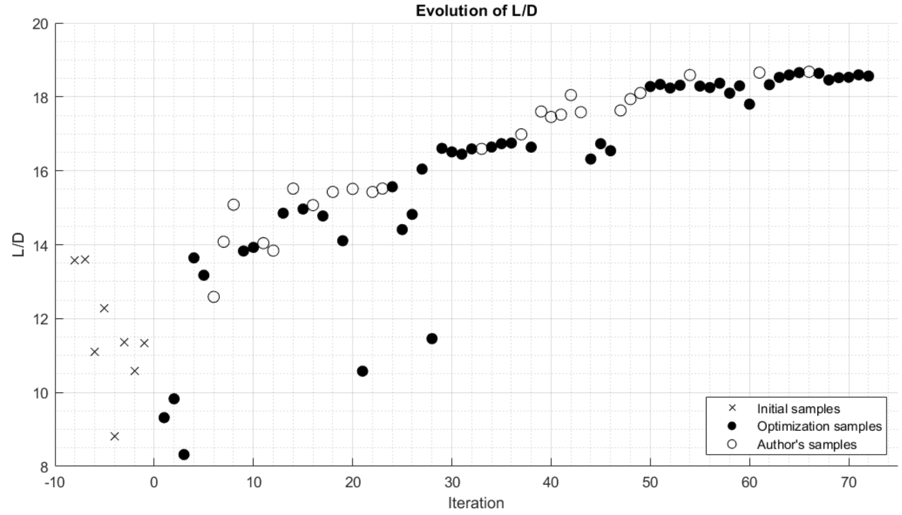

Figure 3.3: Evolution of the lift to drag ratio along the optimization.

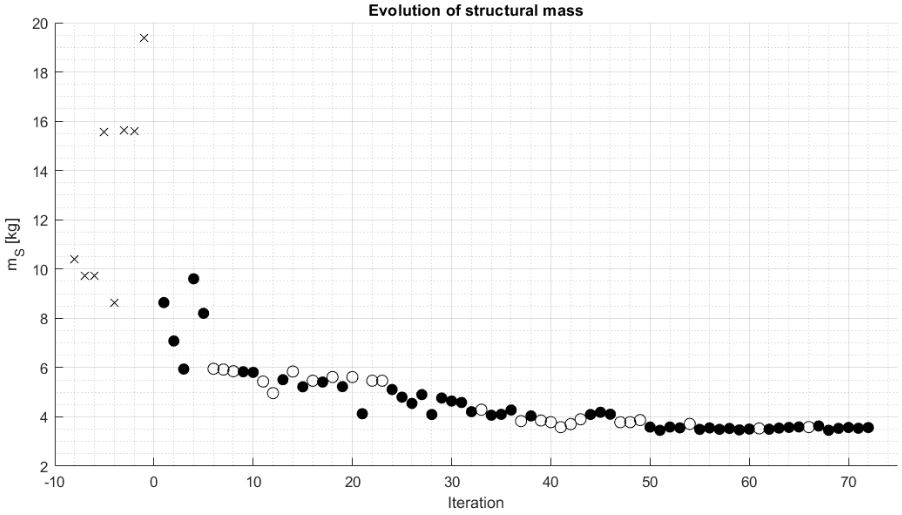

Figure 3.4: Evolution of the structural mass along the optimization.

by the author that were characterized by having higher aspect ratio wings which were able to exceed the $L/D = 17$. After three failed attempts by the surrogate search to obtain better range configurations, three more user configurations were tested to try to guide the design to that part of the design space. This was successful and from iteration 50, the configurations were almost all able to get L/D ratios over 18 but always below 18.7.

The structural mass of the initial configurations was very high and even made some of them unfeasible because there would be no extra mass for fuel. However, the mass quickly dropped off as some of the structural variables got closer to their lower bounds. The mass started decreasing to slightly above 4 kg until iteration 36. Then the introduction of the author-designed configurations allowed for the structural variables to be brought down to their lower bounds when permitted which made m_s decrease below 4 kg. As with the L/D, the structural mass remained low between the interval of 3.4 and 3.6 kg from iteration 50 onwards.

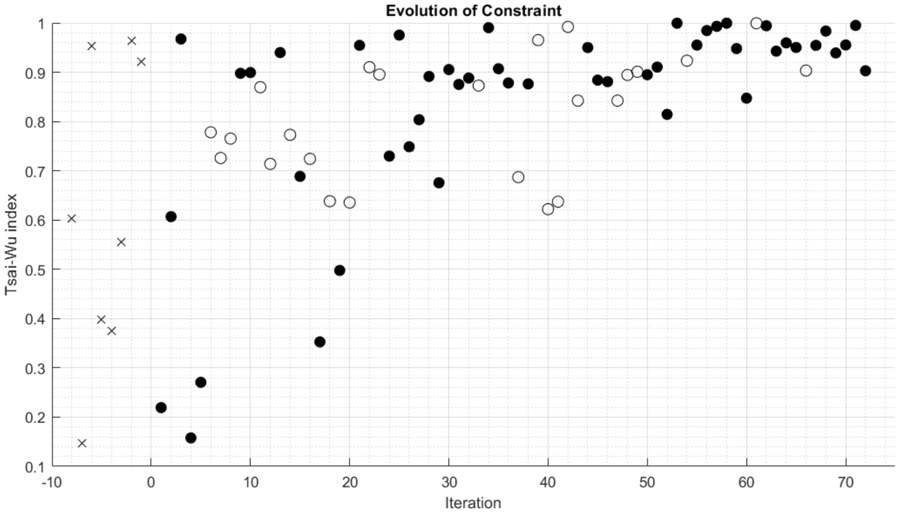

Figure 3.5: Evolution of the Tsai-Wu failure index along the optimization.

As for the constraint, up until iteration 19, some configurations were unnecessarily reinforced since the Tsai-Wu criterion was below 0.5. As the surrogate models got better at predicting the structural influence of each variable, the constraint value started getting consistently closer to 1 and after iteration 42 it was always above 0.8 with most of the configurations being above 0.9 which is expected due to the minimization of the structural mass.

Figures 3.6 and 3.7 plot the evolution of the objective function ΔR and the ratio R/R_{ref_0} respectively, where R_{ref_0} is the range of the initial reference configuration.

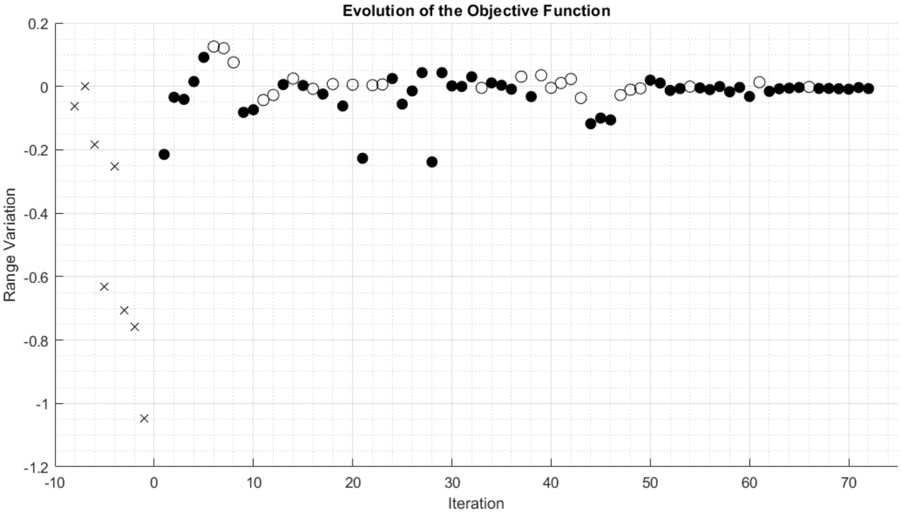

Figure 3.6: Evolution of the objective function along the optimization.

As expected, the variation in range tends to be closer to 0 the further along the optimization process is done. While it was possible to get increases of 12% in range from one iteration to the next in the beginning, at the later stages multiple configurations were worse than the previous ones and when they were better, the increase in range was below 2%. From iteration 51 until 73 there was only one

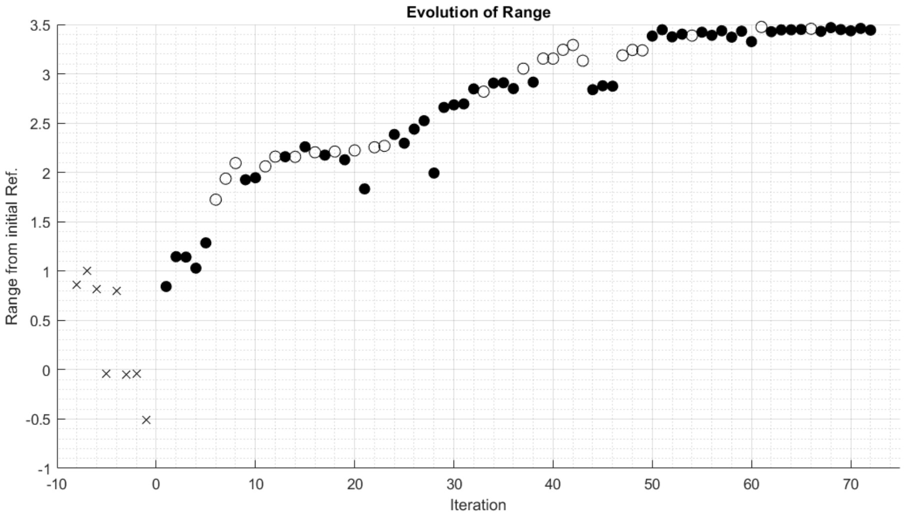

Figure 3.7: Evolution of the range ratio R/R_{ref_0} along the optimization.

increase in range in iteration 61. This is the interval where the optimization process can be classified as converged since more iterations are not able to bring better results.

From iteration 55 to iteration 73 the range ratio R/R_{ref_0} is about 3.45 which means that these configurations can go 3.45 times as far as the initial reference.

As a last means of analysis, figure 3.8 shows the design points of the solved problem on a lift to drag ratio vs structural mass plot.

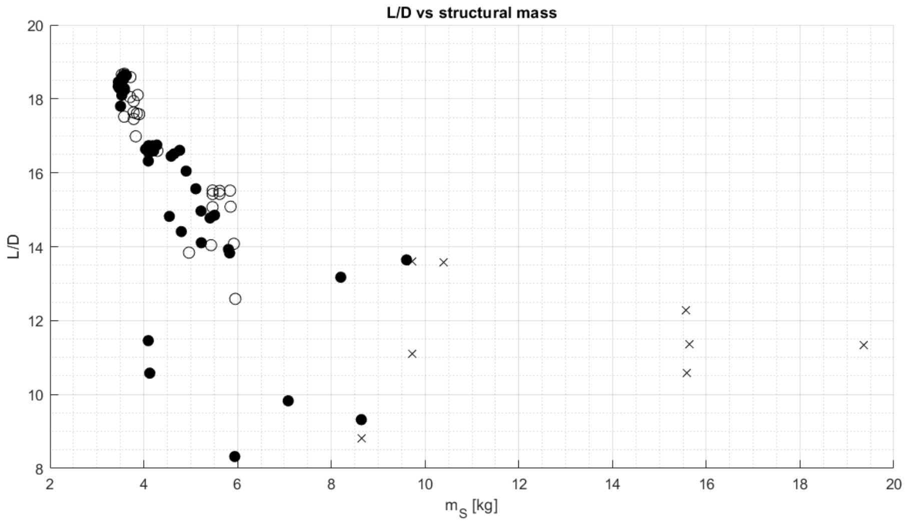

Figure 3.8: L/D vs structural mass plot.

Disregarding the initial configurations and some of the early iterations, most of the aircraft designs are below the 6 kg mark and above an L/D of 13.5. Furthermore, there is a very big concentration of points below an m_s of 4 kg and with an L/D above 17 where the iterations can't be easily distinguished. This mostly corresponds to the same interval of configurations between iterations 50 and 73 where the optimization process started to converge.

3.6.1 Final configuration

After the general analysis of the evolution of the optimization process, it is necessary to choose the configuration that will go forwards to further analysis. Looking at figure 3.9 it is possible to see in detail the final designs that have the higher values of range.

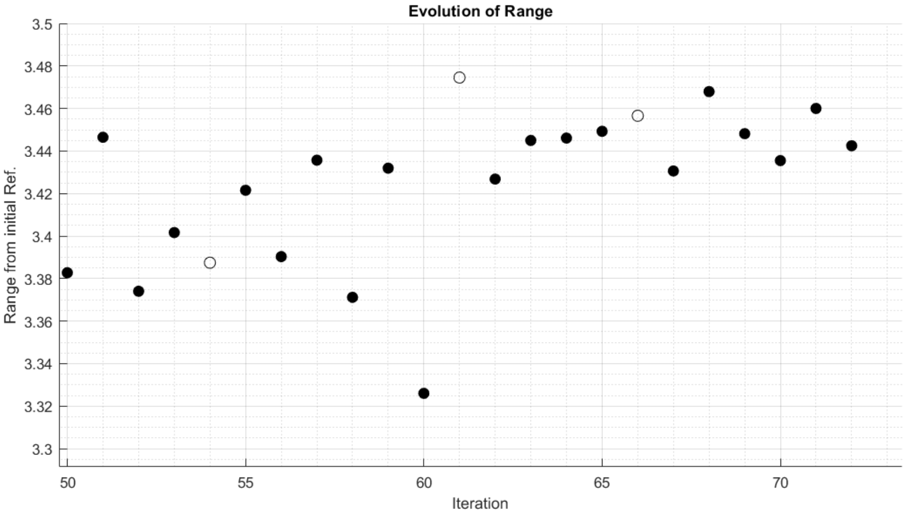

Figure 3.9: Close-up of the evolution of the range ratio R/R_{ref0} along the optimization.

The 24 points displayed have all similar designs characterized by a high aspect ratio wing, a small canard when compared to the wing, and a lightweight structure. Out of these, two of them display the highest levels of range, iterations number 61 and number 68, even if by only a percent. The isometric and top views of both aircraft can be seen in figures 3.10 and 3.11.

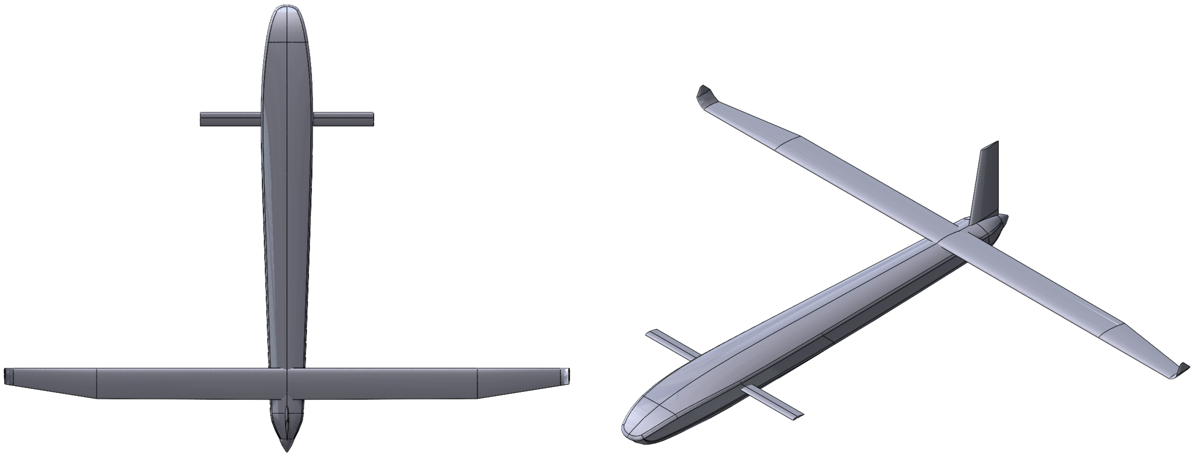

(a) Top view of configuration 61.

(b) Isometric view of configuration 61.

Figure 3.10: Top and Isometric views of configuration 61.

These two configurations were analyzed in more detail through the creation of table 3.3 which states the range performance values, some geometric parameters that were considered of higher significance, and the trim condition angles where α_c is the canard true angle of attack which can be obtained by the expression $\alpha_c = \alpha + i_c$.

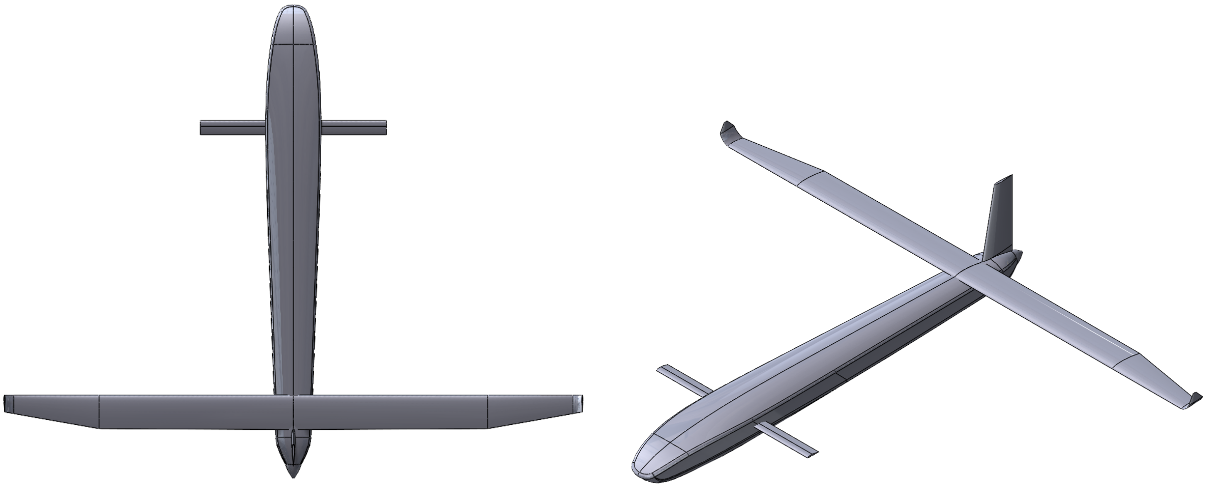

(a) Top view of configuration 68.

(b) Isometric view of configuration 68.

Figure 3.11: Top and Isometric views of configuration 68.

Table 3.3: Comparison between iteration 61 and iteration 68.

	Configuration 61	Configuration 68	Δ [%]
L/D	18.655	18.457	-1.06
m_s [kg]	3.521	3.457	-2.10
R/R_{ref}	3.475	3.468	-0.20
S_w [m^2]	0.5251	0.5116	-2.58
b_w [m]	3.152	3.001	-4.79
$\bar{c}_w$ [m]	0.167	0.170	2.32
AR_w	18.915	17.600	-6.95
b_c [m]	1	1	0
c_c [m]	0.0788	0.0767	-2.58
AR_c	12.695	13.031	2.65
α_{trim} [°]	1.437	2.027	-
$i_{c_{trim}}$ [°]	3.718	2.926	-
α_c [°]	5.155	4.952	-

Configuration 61 is characterized by a slightly higher L/D but also a higher structural mass. This is mainly due to the higher wingspan and smaller mean aerodynamic chord ($\bar{c}_w$) when compared to iteration 68 which results in a higher aspect ratio of 18.9 versus 17.6 respectively. This increases L/D but has the drawback of requiring more composite layers to withstand the higher wing root bending momentum so the total range difference between the two configurations is only 0.2 %.

Both canards are set at 15 % of the wing area and because configuration 61 has a 2.58 % higher wing area, so will its canard. Since both have an equal span of 1 m, the difference is in the canard chord which results in a slightly lower aspect ratio of 12.7 for canard 61 in comparison with 13.0 for canard 68.

Configuration 61 has a lower trim angle of attack but a higher canard incidence angle which in total makes the angle of attack of the canard higher than for aircraft 68. This may mean that the stall speed of configuration 61 may be higher than for 68, which can prove disadvantageous for testing reasons as will be discussed in the next chapter.

Overall, the fact that configuration 68 has a lower aspect ratio which means it might be less susceptible to aeroelasticity phenomena and that the canard has a lower i_c and α_c which may give it a slower stall speed, made it be the chosen configuration for the analysis to come.

The final configuration originating from the optimization process is then number 68. The function outputs from this design point are:

- $m_s = 3.457$ kg;
- $m_f = 13.188$ kg;
- $L/D = 18.457$;
- $R/R_{ref_0} = 3.468$.

In comparison with the initial reference configuration, the structural mass is 64.5 % lower and the lift to drag ratio is 35.7 % higher which combined results in 3.468 times higher range. When comparing to the best configuration up until iteration 33, m_s still decreased 17.9 % and the L/D increased 11.2 % which means that the range increased in total 21.7 % which proves that there was still room for improvement at the beginning of this thesis work.

The design variable values for this configuration are displayed in table 3.4.

Table 3.4: Values of the design variables for the final chosen design.

Variable	Value	Variable	Value
y_{scale} [-]	1	$\gamma_{w_{tip}}$ [°]	0.121
z_{scale} [-]	1	$y_{\gamma_{w_{disc}}}$ [m]	$0.7b_w/2$
thk_{fuse} [m]	0.002	Λ_w [°]	0
r_{tube} [m]	$0.606c_ct_c$	t_w [-]	0.105
thk_{tube} [m]	$0.2r_{tube}$	cbr_w [-]	0.029
$pos_{f_{spar}}$ [m]	$0.25c(y)$	b_{wglt} [m]	0.05
$thk_{tip_{spar}}$ [m]	8×10^{-4}	λ_{wglt} [-]	0.2
$thk_{disc_{spar}}$ [m]	8×10^{-4}	Λ_{wglt} [°]	28.467
$thk_{root_{spar}}$ [m]	1×10^{-3}	t_{wglt} [-]	0.08
$thk_{tip_{skin}}$ [m]	6×10^{-4}	cbr_{wglt} [-]	0.0021
$thk_{disc_{skin}}$ [m]	6×10^{-4}	b_c [m]	1
$thk_{root_{skin}}$ [m]	1.008×10^{-3}	S_c [m^2]	$0.15S_w$
b_w [m]	3.001	l_c [m]	1.5
c_{root_w} [m]	0.186	z_c [m]	pos_{bot}
c_{disc_w} [m]	0.181	cbr_c [-]	0.052
c_{tip_w} [m]	0.1	c_{root_f} [m]	0.2
$y_{c_{disc}}$ [m]	$0.695b_w/2$	λ_f [-]	0.6
$\gamma_{w_{root}}$ [°]	0.951	b_f [m]	0.4
$\gamma_{w_{disc}}$ [°]	0.1434		

Some of the design variables were set to their limit bounds, either lower or upper. An example of this is the fuselage scaling factors which are both set to the minimum lowering the drag related to the fuselage due to the reduced frontal area. These dimensions guarantee that the fuselage is just big enough to fit the MAD sensor.

The fin dimensions are at their upper bounds. This increases its area which allows for it to be placed closer to the trailing edge of the wing. Coupled with the small value for the l_c, the fuselage can be short with just 2.545 m reducing its surface area and once again its drag.

The wing chord and twist discontinuities are almost coincident and at their upper bounds. Combined with the fact that the chord at the discontinuity is almost the same as at the root and that there is no sweep, the wing can be decomposed to an approximately rectangular section and a tapered section. There is some degree of twist at the root which is almost canceled at the discontinuity and kept approximately constant until the tip of the wing. Taking into account the small winglets, the total wingspan of the aircraft is 3.102 m. The wing airfoil has almost 3 % camber and a thickness of just 10.5 %. The distance between the center of gravity of the aircraft and the aerodynamic center of the wing (l_w) is 0.295 m.

The structural variables related to the thickness of the laminates are almost all set to their minimum bounds, except for root skin. By taking a closer look at the Tsai-Wu distribution in figure 3.13 it is possible to see why this happens. The wingbox, in particular the wing skin, is one of the components that carries the biggest loads and if the laminate had fewer layers it would not be able to withstand the aerodynamic forces.

The canard area is set at 15 % of the wing, which results in most of the lift being produced by the latter which is more efficient making the L/D higher. The canard is also positioned low on the fuselage reducing wake interference with the wing. The tube that supports is about 60 % of the airfoil thickness and the minimum thickness allowed. At the root, it is also one of the most stressed components.

Figure 3.12 illustrates the most relevant dimensions of the final aircraft configuration.

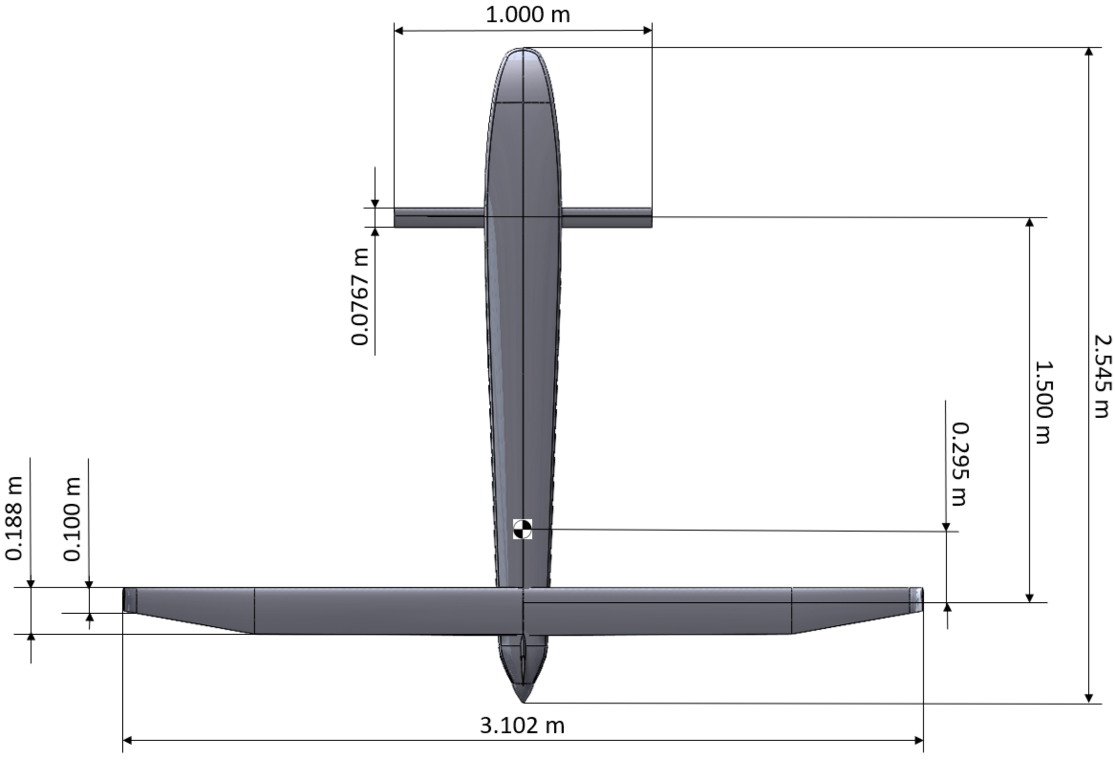

Figure 3.12: Geometric dimensions of configuration 68.

Close-ups of the Tsai-Wu criteria values in the most critical regions can be visualized in figures

3.14(a) and 3.14(b).

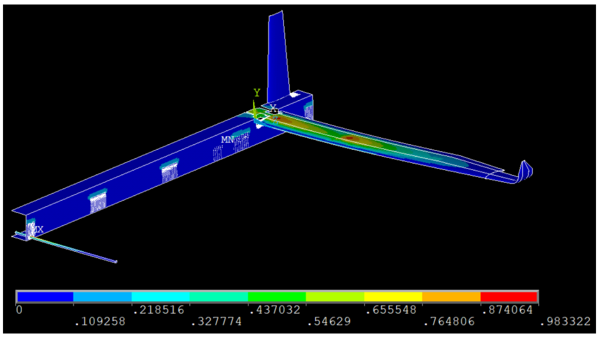
Y
X
MN
MX
0
.109258
.218516
.327774
.437032
.54629
.655548
.764806
.874064
.983322

Figure 3.13: Tsai-Wu failure index values on the entire aircraft structure.

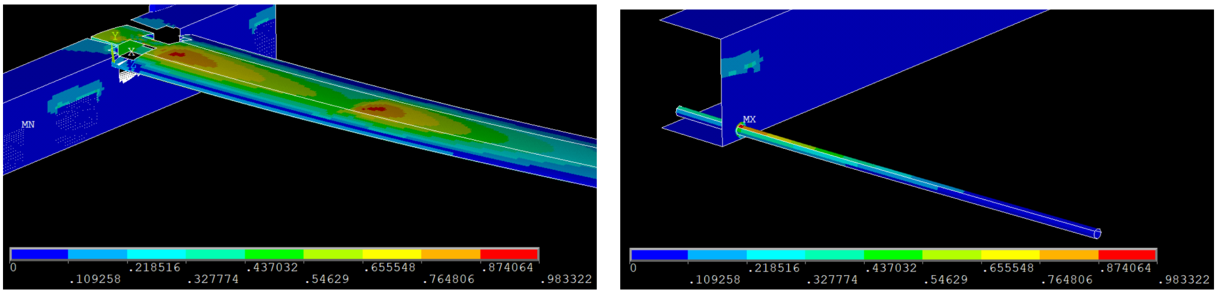
Y
X
MN
MX
0
.109258
.218516
.327774
.437032
.54629
.655548
.764806
.874064
.983322

(a) Wing root region.

(b) Canard tube.

Figure 3.14: Tsai-Wu failure index values on critical regions.

Chapter 4

Aircraft Characterization

This chapter is dedicated to the aerodynamic and structural characterization of the aircraft. Possible design changes were studied and some of them were implemented. The rationale behind them is also explained here. An FDM model was built and the stability of the aircraft was evaluated.

4.1 Design change study

After the optimization process was completed and the final configuration was chosen, there was the possibility of modifying the design to a concept not possible in the optimization design space. This modified design consisted of taking out the vertical stabilizer, sweeping back the wing, and increasing the winglets' area to the same size as the vertical stabilizer. The objective of this change was to decrease the total drag by eliminating the component coming from the vertical stabilizer even if it slightly increased the wing drag. The configuration that resulted from this change has a 10° wing sweep angle and rectangular winglets with 0.34 m in height and 0.1 m in chord. The top and isometric views of the OML model of this aircraft can be seen in figures 4.1(a) and 4.1(b).

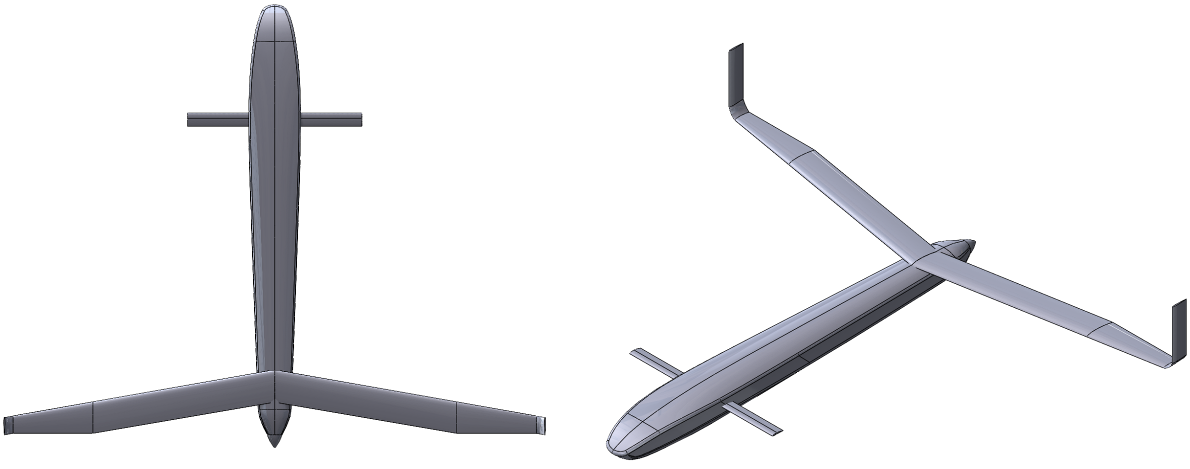

(a) Top view of swept-back configuration.

(b) Isometric view of swept-back configuration.

Figure 4.1: Top and Isometric views of swept-back configuration.

The trimmed L/D of this configuration is 18.576 which is 0.64 % higher than the base configuration. Initially, it might seem that it is worth making this change, but the mass increase due to this design change also has to be taken into account. This mass increase will mostly come from the increased wing ultimate root bending moment introduced by the lateral force produced by the winglet.

Assuming that the original empty aircraft mass is 20 kg, which leaves 5 kg for the fuel tank, the new mass over which the increase in L/D does not compensate the change in design can be calculated by the expression 4.1 which is derived from the range equation 3.1.

$$18.457 \ln\left(\frac{25}{20}\right) = 18.576 \ln\left(\frac{25}{x}\right) \Leftrightarrow x = 20.0284 \, \text{kg} \, . \tag{4.1}$$

This means that if the increase in mass is over 28.4 g then it is not worth to change the design. The initial mass estimate of the wing according to the FEM model is 1.368 kg which means that the increase in mass has to be less than 2.08 % of the wing mass.

In cruise condition, the wing root bending moment estimate from CFD of the original configuration is approximately 75.14 N.m and for the design in question, it is 76.90 N.m which is 2.34 % more. Assuming that in the ultimate load case scenario, the percentage difference is the same as for cruise condition and that the increase in mass is directly proportional to the wing root bending moment, this means that it is already not worth to pursue this design change since $2.34 > 2.08$. Furthermore, a rudder for the wing tip surfaces was designed to estimate the increase in structural load that this control surface would add. CFD analysis showed that the wing root bending moment increased to 93.74 N.m or 24.75 % more, which translates to an increase of 339 g for the wing structure, assuming proportionality between mass and wing root bending moment once again.

Along with the added complexity of having two control actuators located at the tips of the wing instead of just one close to the fuselage made this design change be discarded.

4.2 Stall Speed Determination

The next step in validating the design was determining the stall speed V_{stall}. The requirements for this parameter are related to the testing of the aircraft. For it to be tested near CfAR's headquarters, the operating speed can not exceed 28 m/s as it would be too difficult to maneuver it safely within the testing field. Considering an operating speed 1.3 times higher than the stall speed, which is standard practice in aviation, V_{stall} should be at the maximum 21.5 m/s.

To calculate the stall speed, 12 CFD simulations were performed with varying angles of attack between -5° and 17° . Along with the simulation with the angle of attack in trim condition, these computations allowed for the construction of the plots in figures 4.2(a) and 4.2(b).

These plots show the C_L and C_m values in regards to the angle of attack for the wing, canard, and fuselage separately. It also shows the trendline for the sum of the wing and fuselage components while their behavior is linear which is between -5° and 9° .

To calculate the stall speed one must solve the system of equations 4.2 to determine the unknown

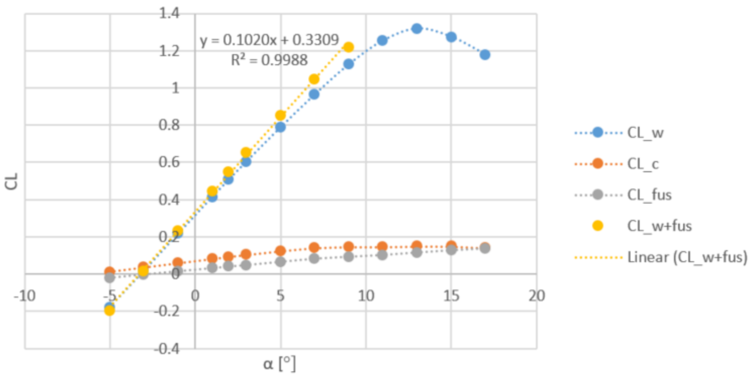

(a) C_L vs α plot.

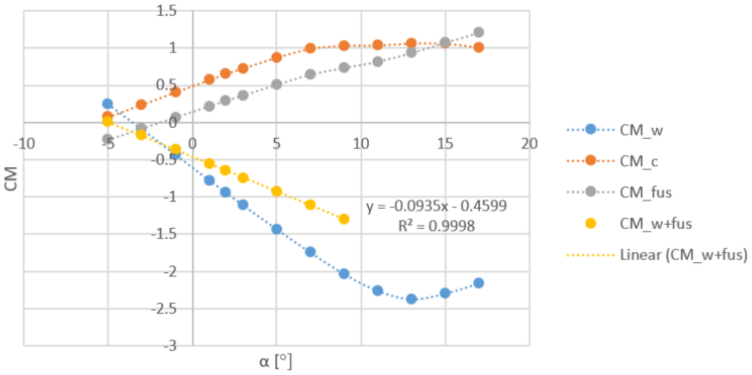

(b) C_m vs α plot.

Figure 4.2: C_L and C_m as a function of α.

variables V_{stall} and α_{stall}. Since the aircraft has a canard configuration, the canard must stall first. This means that the canard lift and moment component will be at their maximum level possible, $C_{L_{c_{max}}}$ and $C_{m_{c_{max}}}$ respectively. From figures 4.2, it is possible to see that this happens at a canard angle of attack of $\alpha_c = 13°$. The C_L and C_m contributions of the wing plus fuselage are defined as $C_{L_{w+fus}} = m_1\alpha_{stall} + b_1$ and $C_{m_{w+fus}} = m_2\alpha_{stall} + b_2$, where the m and b terms are acquired from the linear trendlines in figures 4.2.

$$\begin{cases} M = 0 \\ L_c + L_{w+fus} = m_i g \end{cases} \Leftrightarrow \begin{cases} C_{m_{c_{max}}} + C_{m_{w+fus}} = 0 \\ \frac{1}{2}\rho S_w V_{stall}^2 (C_{L_{c_{max}}} + C_{L_{w+fus}}) = m_i g \end{cases} \Leftrightarrow$$
$$\Leftrightarrow \begin{cases} C_{m_{c_{max}}} + m_2\alpha_{stall} + b_2 = 0 \\ \frac{1}{2}\rho S_w V_{stall}^2 (C_{L_{c_{max}}} + m_1\alpha_{stall} + b_1) = m_i g \end{cases} . \tag{4.2}$$

Solving the system of equations for the aircraft at hand one gets $V_{stall} = 26.278$ m/s and $\alpha_{stall} = 6.402°$. The angle of attack is still below 9° which is still inside the interval where the linear trendline of the wing plus fuselage is valid. The canard incidence angle for this situation is $i_c = \alpha_c - \alpha_{stall} = 13 - 6.402 = 6.598°$. After simulating this condition with CFD to validate the results, the stall angles were recalculated to get a more precise stall velocity and after another CFD simulation to validate these second results, the stall condition was determined to be $V_{stall} = 26.205$ m/s, $\alpha_{stall} = 6.464°$ and $i_c = 6.536°$.

This stall speed is not low enough because the aircraft would have to be flown dangerously close to the stall speed when testing. Thus, two more aircraft designs where the canard area was changed were analyzed. The first aircraft, which will be addressed as configuration 68-20, has a 20% bigger canard area and was used to test what would be the difference in the stall speed of a small change in the canard area. Configuration 68-109 or the second one has a 109 % bigger canard area and was used to see what would be the difference of a more significant change in canard area. The 109 % value was decided taking into consideration that the canard area should not be bigger than 25 % of the wing area. By taking the canard span and canard chord of this configuration at face level, it would seem that it would be 31.4 % of the wing area but in reality, there is a 0.295 m section of the canard that produces no aerodynamic forces because it is inside the fuselage. The aspect ratio of the canards in all three configurations was kept the same, which means that both the chord and the span varied. A top and isometric view of both configurations can be seen in figures 4.3 and 4.4.

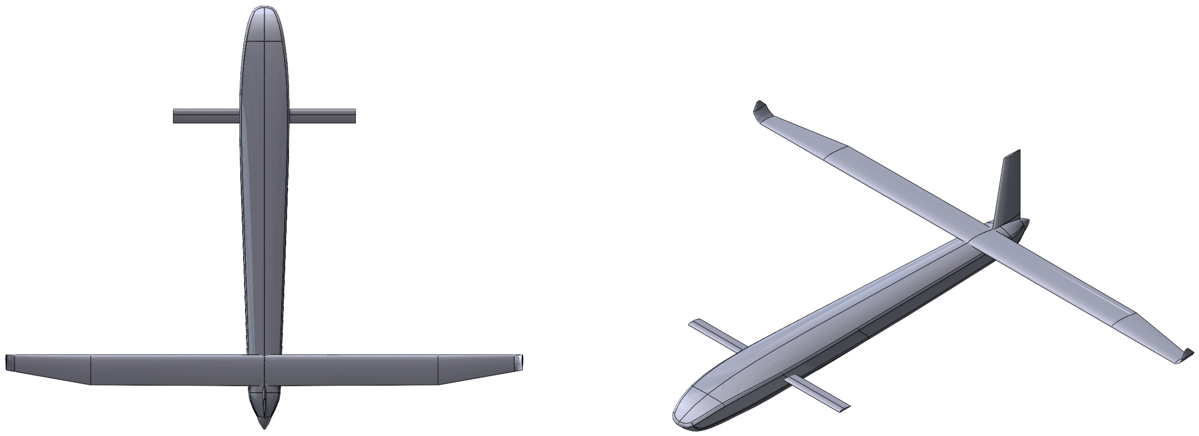
(a) Top view of configuration 68-20.
(b) Isometric view of configuration 68-20.

Figure 4.3: Top and Isometric views of configuration with a 20% bigger canard area.

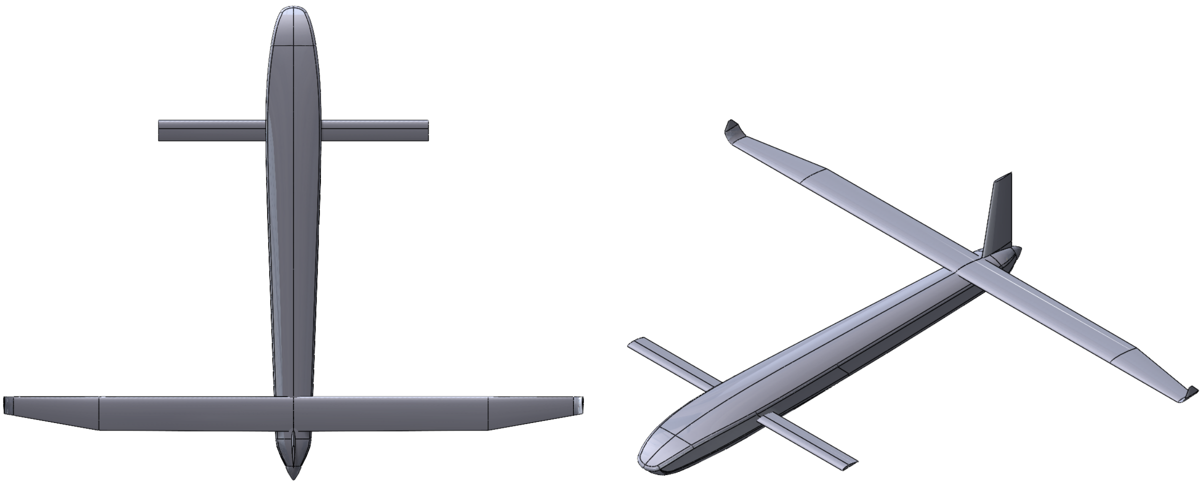
(a) Top view of configuration 68-109.
(b) Isometric view of configuration 68-109.

Figure 4.4: Top and Isometric views of configuration with a 109% bigger canard area.

By applying the same process that was done to configuration 68, the cruise and stall conditions were evaluated for these two new configurations. With these results, table 4.1 was built. It shows some of the geometric differences between the different designs as well as variations of the cruise condition, the stall condition, and range differences.

Table 4.1: Comparison of the three configurations and their stall properties.

	68	68-20	Δ [%]	68-109	Δ [%]
b_c [m]	1.000	1.095	9.6	1.447	44.7
c_c [m]	0.0767	0.0841	9.6	0.111	44.7
S_c [m^2]	0.0767	0.0921	20.1	0.1606	109.4
S_c/S_w [%]	15.0	18.0	20.1	31.4	109.4
$S_{c_{wet}}/S_w$ [%]	10.6	13.2	24.5	25.0	136.4
l_w [m]	0.295	0.327	10.8	0.457	54.9
L/D_{cruise} [-]	18.457	18.233	-1.2	17.774	-3.7
$i_{c_{trim}}$ [°]	2.926	2.199	-0.727°	0.602	-2.323°
α_{trim} [°]	1.968	1.857	-0.111°	1.364	-0.604°
L_w/L [%]	79.31	77.13	-2.8	68.12	-14.1
L_c/L [%]	14.47	16.55	14.4	25.27	74.6
L_{fus}/L [%]	6.22	6.32	1.6	6.61	6.3
V_{stall} [m/s]	26.205	24.974	-4.7	22.608	-13.7
V_{cruise}/V_{stall} [-]	1.336	1.401	4.9	1.548	15.9
L/D_{stall} [-]	15.624	14.672	-6.1	12.754	-18.4
$C_{L_{w_{stall}}}$ [-]	0.912	0.979	7.3	1.066	16.8
$i_{c_{stall}}$ [°]	6.536	5.683	-0.853°	4.299	-2.237°
α_{stall} [°]	6.464	7.317	0.853°	8.701	2.237°
m_c [g]	178.6	214.5	20.1	374	109.41
ΔR_{mass}[1] [%]	0	-0.80	-	-4.36	-
ΔR_{total}[2] [%]	0	-2.01	-	-7.90	-

[1] This difference in range due to the extra structural mass was calculated by assuming the original configuration had 5 kg of fuel.

[2] The total range difference is the sum of the differences caused by the decrease in L/D and the extra structural mass.

From this table, it is possible to verify that an increase in the canard area leads to a decrease in the L/D in cruise of 1.21 % for the 68-20 and of 3.7 % for the 68-109. This is because the bigger surface area in the front brings the CoG forward which in turn makes the percentage of the total lift provided by the canard increase so there is less lift produced by the more efficient wing. On the other hand, the less significant decrease in L/D during cruise allows for a more significant difference in the stall speed of each configuration, going from 26.2 m/s to 24.5 m/s or 4.7 % less for the 68-20 and to 22.6 m/s or 13.73 % less for the 68-109. This decrease in stall speed is accompanied by a higher stall angle which makes the correspondent $C_{L_{wing}}$ higher as well. All configurations have a V_{cruise}/V_{stall} ratio over 1.3 which would make them all viable in that regard. On the negative side, there is also an increase in mass due to the bigger quantity of material necessary to build each canard. In total, the 68-20 has a 2.0 % smaller range than the 68 and the 68-109 has a 7.9 % difference.

After this study was performed, it was decided to progress the rest of the analysis of this project with the 68-109 configuration. Even though the stall speed does not meet the 21.5 m/s requirement, it was decided that 22.6 m/s was enough to test the aircraft at 28 m/s, which gives a testing speed over stall speed ratio of 1.24. This decision was based on the fact that this change only alters the canard area while seeking a design with an even lower stall speed would require either a very big canard converting the airplane configuration to a tandem wing or increasing the wing area which was also not desirable. If in the future the extra range of the original configuration proves to be necessary, then the canard can be reverted to its original state which was considered an easy implementation without big impacts on the design of the rest of the aircraft.

Furthermore, a *MATLAB* program was built to estimate the stall speed based on the canard to wing area ratio and the wing area. From that program, the graph in figure 4.5 was created.

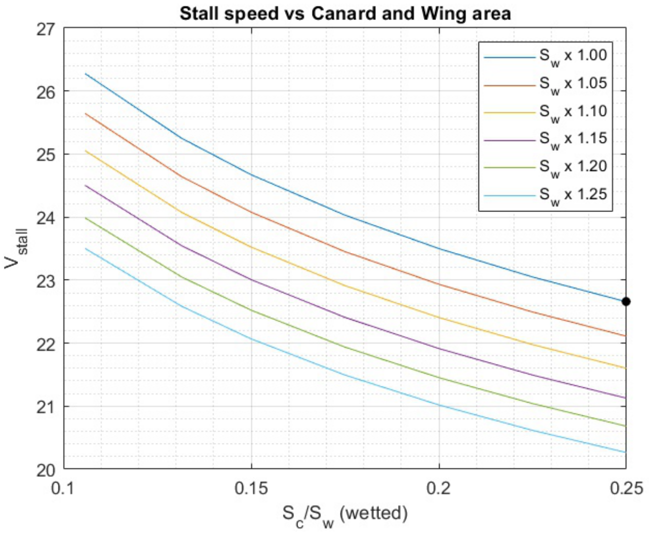

Figure 4.5: Stall speed calculation based on wing and canard area. Black dot signals the chosen configuration going forwards (68-109).

This graph shows that it would be possible to meet the 21.5 m/s requirement by different configurations. For example, it could be chosen to increase the wing area by 10 % while having a canard with a wetted area equal to 25 % of the wing area or it could also be chosen to increase the wing area by 25 % while having a canard area only equal to 17.5 % of the wing area.

4.3 Winglet modification

Before the final OML of the aircraft was established, one last adjustment was made to the winglet design. The way the winglet was defined during the optimization process made it so that the final shape had sharp corners and edges and an overall not smooth transition from the tip of the wing to the tip of the winglet. For these reasons, it was decided that the winglet design could be refined.

Keeping the same tip chord, winglet length and leading edge sweep but changing the transition between the wing and this surface to a smooth curve, it was possible to increase the L/D from the original 17.774 for the 68-109 configuration to 17.815, which represents a 0.23 % increase. This increase is somewhat negligible but at least it shows that the change likely does not negatively impact the performance. Still, changing the design also has another benefit in regards to the manufacturing of the wing.

During the lay-up process of the carbon fiber layers, it is easier to make the final product adhere to the shape of the mold if it is smoother, so the new design makes the chance of success of correctly manufacturing the wing higher. Figures 4.6(a) and 4.6(b) show the old and the new winglet design respectively.

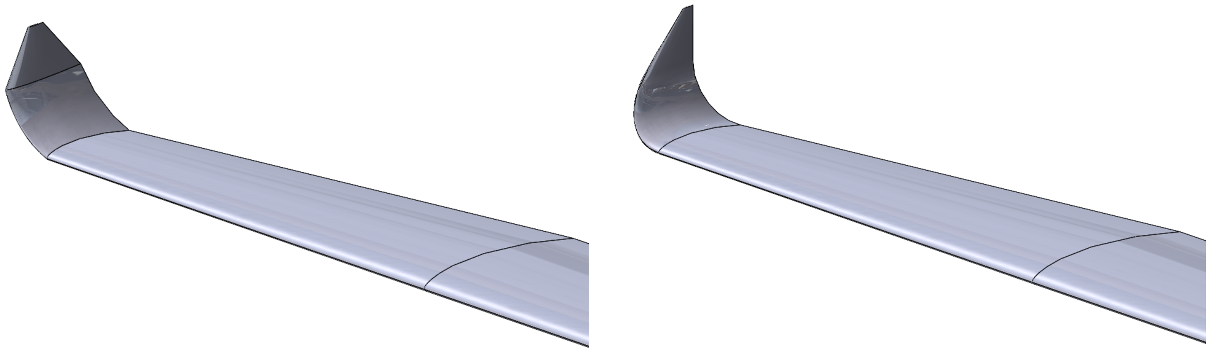

(a) Old winglet design.

(b) New winglet design.

Figure 4.6: Old and new versions of the winglet.

4.4 Structural Validation

The structure of the aircraft suffered several changes in order to get a lighter structure and to increase the available space inside the fuselage.

The first is related to the fuselage. The spar design used in the optimization process was not the most adequate because it took away a substantial amount of the available volume inside the fuselage, leaving all the components that must go inside of it more constrained. Furthermore, it was heavy due to the minimum number of 10 woven layers. Since there is still the necessity of fabricating the outside skin of the fuselage, the decision was to transform the OML of the fuselage into a structure that supports its own loads. The spars were far from breaking in the ultimate load condition, which means that there is extra material that can be removed in order to reduce the structural mass. The implementation of a core material allows for a lighter structure while keeping the thickness and, in turn, the stiffness high. The core material used is a homogeneous PVC foam whose properties can be found on table 4.2. The laminate will then be a sandwich composite composed of one layer of woven carbon fiber at a 45° angle with the aircraft longitudinal axis on each side of one layer of core material.

The second structural change is related to the canard. Similar to the fuselage, there is still the need to make the outside skin even with the canard tube. For this reason, it was decided it was best to make the skin of the canard the main load-carrying structure. While the canard tube was composed of only of UD layers, the new canard laminate will be made of two woven layers, one UD layer and another woven layer all oriented along the span of the canard. This will give it enough structural integrity to withstand not only the aerodynamic loads but also the thrust of the electric motors for the VTOL capabilities which may be placed at the tips of the canards.

With this in mind, a Computer-Aided Design (CAD) surface model was made in *SOLIDWORKS*. This

Table 4.2: PVC foam material properties. A negative sign corresponds to a compressive limit.

	PVC Foam
ρ [kg/m^3]	80
E [MPa]	90
ν [-]	0.3
G [MPa]	27
σ_{max} [MPa]	2.5
σ_{min} [MPa]	-2.5
τ_{max} [MPa]	1.15
h_n [mm]	3.175

model was imported to *Ansys Workbench* and the composite definition of each surface was done using the *Ansys Composite PrepPost* module (ACP). The model only includes half of the aircraft since the load cases analyzed will be symmetric to reduce computational costs.

The same boundary conditions used in *Ansys APDL* were applied here, which are the no displacement in the pitch axis direction, as well as zero rotation in the roll and yaw axes. MPC contact formulation elements were used to connect the different structural components while beam contact formulation elements were used between the wing skin and the wing spars. A remote point mass connected to the fuselage was also added to bring the total aircraft mass up to 25 kg and to place the CoG in the correct position. Figure 4.7 shows the imported structural model in Ansys.

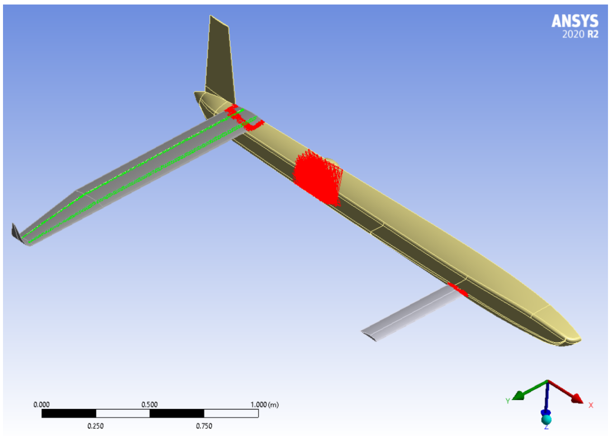

Figure 4.7: Structural model in *Ansys Mechanical*. Red lines represent MPC connections while green lines model beam connections.

For a better analysis of the structure, instead of using the aerodynamic loads calculated from the LF Prandtl's LLT, a one-way FSI employing CFD analysis was used. Since the ultimate load case scenario is a 4.5g maneuver and the lift varies linearly with the square of the velocity, the simulated condition had the cruise angle of attack and canard incidence angle but a velocity $\sqrt{4.5} = 2.121$ times higher, *i.e.*, 74.246 m/s. This means that the aircraft is trimmed but will be producing 4.5 times the lift necessary to sustain the pull-up maneuver. This speed is over the dash speed requirement, so over the maximum velocity specified for the aircraft, but what is being tested is the ability of the aircraft structure to survive the load and not the airspeed.

The resulting pressure on the surfaces of the aircraft is then imported to *Ansys Mechanical* and applied to the structure surfaces. This imported pressure can be seen in figure 4.8.

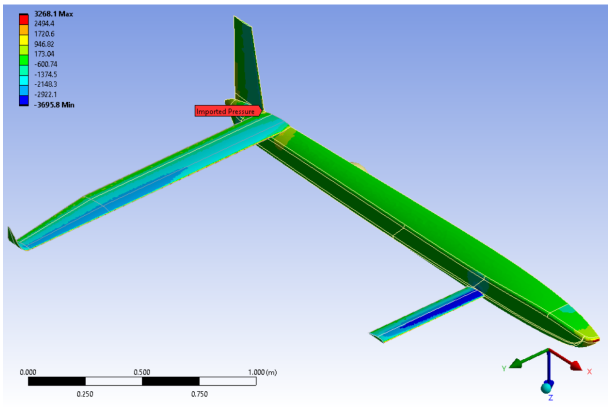
3268.1 Max
2494.4
1720.6
946.82
173.04
-600.74
-1374.5
-2148.3
-2922.1
-3695.8 Min
Imported Pressure
0.000
0.500
1.000 (m)
0.250
0.750
Y
X
Z

Figure 4.8: Imported pressure mapped on the structural components. Scale in Pascal.

The structural analysis is then run with large deflections on. Large deflections on makes the load be applied in increments and after each substep, the stiffness matrix K of the structure is recalculated to take into account the deformed state. This is especially important when large deflections occur, hence the name.

After running the simulation it was found that the wing structure from the optimization process is not capable of withstanding the aerodynamic loads for the ultimate conditions. Figure 4.9(a) plots the Tsai-Wu failure index for the whole aircraft structure while figure 4.9(b) shows a close-up of the wing root section.

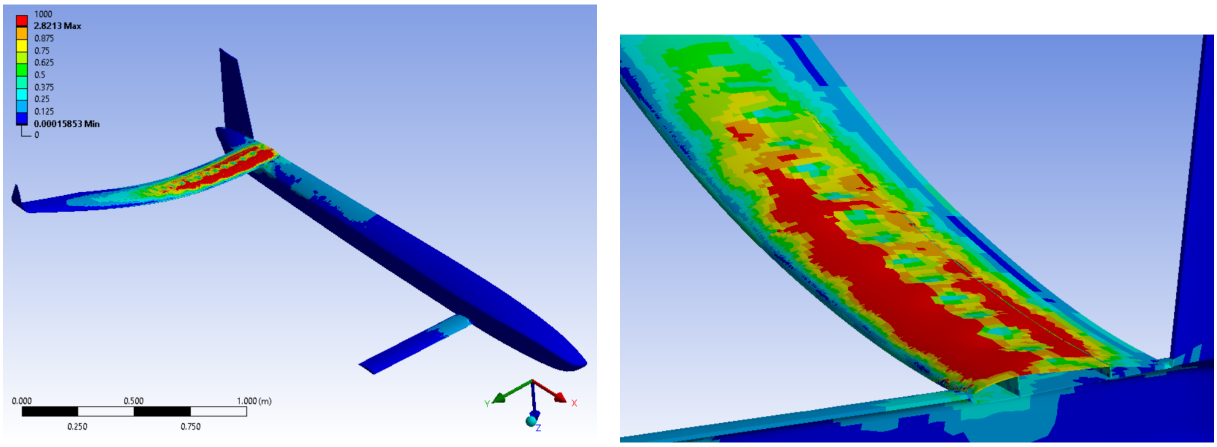
1000
2.8213 Max
0.875
0.75
0.625
0.5
0.375
0.25
0.125
0.00015853 Min
0
0.000
0.500
1.000 (m)
0.250
0.750
Y
X
Z

(a) Tsai-Wu failure index on aircraft.

(b) Close-up of Tsai-Wu failure index on wing.

Figure 4.9: Tsai-Wu failure index on initial aircraft structure and close-up on wing root.

Due to the downwash of the canard, the pressure distribution closer to the wing root section is less intense than at the middle and tip of the wing. This makes the latter sections produce more lift which in turn amplifies the wing root bending moment since these sections are further away from the center of the aircraft. The winglet also amplifies this effect as it makes more lift be produced by the tip of the wing, something that is not taken into account in Prandtl's LLT. The result is a maximum Tsai-Wu failure index of 2.82.

Furthermore, buckling is visible in the top skin between the front and rear spars. The non-linear analysis permitted the finding of this issue. Buckling is characterized by the bowing of a structure when under compression, even if the load applied does not reach the ultimate compressive strength. In this case, it is possible to see that the Tsai-Wu criteria values in this region are under 1, the value at which the composite breaks, but buckling still occurs. This problem also needs addressing.

The solution to both these situations is a redesign of the composite layup. The top surface will be different from the bottom surface since CFRP is weaker in compression than in tension. The top skin will have the same core as the fuselage between the two spars to eliminate buckling. The woven layers will be placed at 90° instead of 45° because it was found these are better at carrying the loads and the composite will always be symmetric.

The layup of the top surface from the root until 0.25 m after is composed of two woven layers, two UD layers, the core, two UD layers, and two woven layers, in that order. From 0.25 m to 0.50 m after the root, the layup has two less woven layers, one on top and one on the bottom. From 0.50 m until the chord discontinuity at 1.04 m two UD layers are dropped, always keeping the laminate symmetrical. The bottom surface of the wing has one woven layer, two UD, and another woven layer from the root up until the chord discontinuity at 1.04 m away from the root. From the 1.04m up until the beginning of the winglet 1.5 m away from the root chord, both the bottom and top surfaces are composed of three woven layers which means that the core in the top surface also ends because the stresses at this section are not enough to make the composite buckle. The winglets are made of two woven layers on each skin.

The wing spars also suffered a redesign. Previously they were composed of five 45° woven layers that dropped down to four after 0.88 m. The angle was changed to 90° for the same reason as the wing skin and the number of layers was decreased. Both spars have 4 layers initially until they transition to 3 after 0.5 m and to 2 at the chord discontinuity.

With this new layup sequence, the structural simulation was reevaluated. The Tsai-Wu failure index for this scenario is available in figure 4.10(a). The deformation values of the structure are also available in figure 4.10(b).

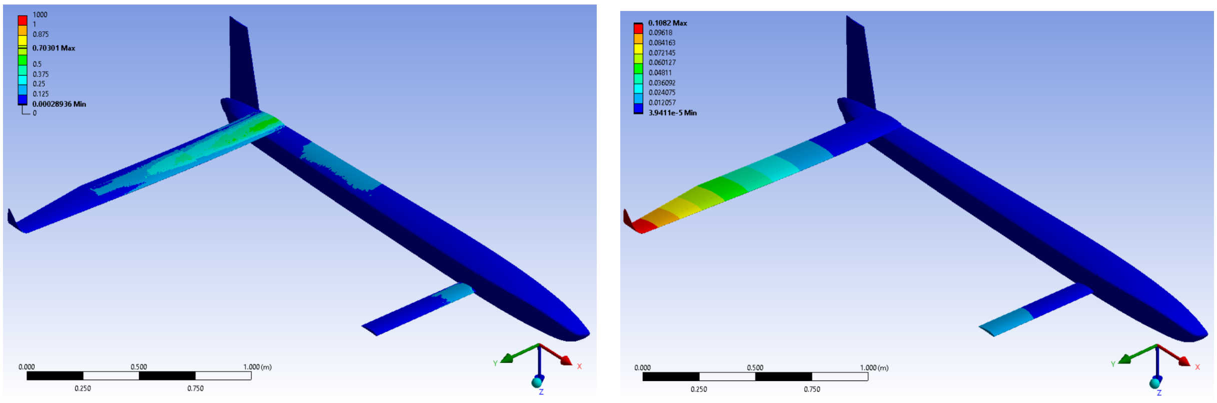

(a) Tsai-Wu failure index on aircraft.

(b) Deformation.

Figure 4.10: Tsai-Wu failure index on revised aircraft structure and resulting deformation.

The maximum Tsai-Wu failure index in the new composite lay-up is 0.703 near the root section which does not exceed the critical value of 1. This means that it will not break in the ultimate load case scenario. No buckling is visible. It is possible to see jumps in the failure criteria values when layers are removed from the top surface, but they still do not exceed the value of 1, which means that it should be safe to remove those layers. Furthermore, it is possible to see that the maximum deformation seen on the aircraft is at the tip of the wing and has a value of 0.108 m.

The Tsai-Wu failure index values in the fuselage are still low. They do not exceed 0.3 in the most stressed regions, which are the connections to the wing, canard, and point mass. Its deformation is in the millimeter range which ensures that all the electronic equipment, propulsion system, and payload are safe from big deformations.

The canard has a Tsai-Wu failure index always below 0.35 so it is also safe from breaking. Its maximum deformation is 0.018 m at the tip, which is a small deformation in comparison to the span of the canard.

The total estimated mass of the structural components is 3.316 kg. 1.607 kg are from the fuselage, 0.374 kg from the canard, and 1.335 kg from the wing. This means that the mass decreased from the original configuration from chapter 3. Even though the fuselage surface area is considerably bigger than the fuselage spars were, the use of a core allowed it to be lighter and remain stiff. The canard is heavier than the tube was, but one must consider that the tube did not have the outer shape and that the canard is now more than twice the size of the previous canard. Even though the wing had to be reinforced, the different layup on the bottom skin allowed for a reduction in mass that made the total mass of this component still be lower than the original.

4.5 Aircraft Performance

4.5.1 Cruise Performance in Deformed State

With the final aerodynamic design done and the final composite structures defined, the aircraft performance can be further characterized.

The cruise performance will be accessed by a two-way FSI simulation. This simulation will determine the aerodynamic performance of the aircraft taking into account the deformation caused by the aerodynamic loads.

The analysis will be performed using *Ansys Workbench* to couple the *CFX* and *Transient Structural* modules. The first step was importing the structural model and the CFD OML with the domain to *Ansys* and defining their respective meshes. The surfaces in both models that lie on the interface have to be selected. Then, using the *System Coupling* module, both computational analysis methods will be connected with two Data Transfer processes. The first will be the transfer of the pressure forces from *CFX* to *Transient Structural*. The second runs in the opposite direction and transfers the displacements from the loaded structure to the mesh of the fluid domain. The mesh in the fluid domain has to be remeshed after each structural analysis to take into account the change in geometry.

After running the analysis, it was discovered that the L/D in cruise condition is 17.800 which is a 0.15 % better result than with just the CFD analysis. This shows that the fluid forces deform the structure in a way that should not decrease the aerodynamic coefficients.

By analyzing the pressure distribution around the aircraft and on the symmetry plane as seen in figure 4.11 it is possible to see that the canard has a higher pressure differential than the wing. By also analyzing the streamlines around the aircraft like it is shown in figure 4.12, it is possible to see that the former lifting surface produces a downwash effect on the fluid flow that can be felt by the latter from the root section up until the length of the canard span. This results in a lower pressure distribution in this area and a load increase in the second half of the wing, as was previously mentioned in section 4.4. It is also possible to see that the fuselage shape has a small pressure drop in the top front surface which is what allows it to make around 6.6 % of the total lifting force.

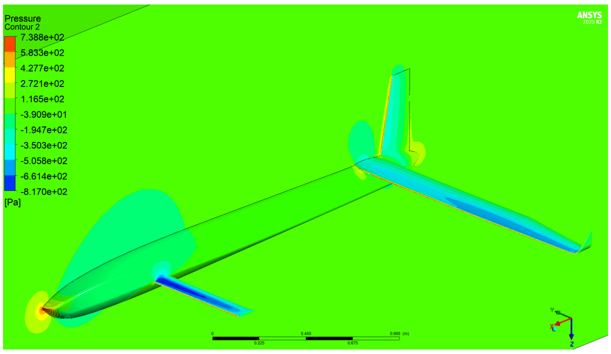
Pressure
Contour 2
7.388e+02
5.833e+02
4.277e+02
2.721e+02
1.165e+02
-3.909e+01
-1.947e+02
-3.503e+02
-5.058e+02
-6.614e+02
-8.170e+02
[Pa]
ANSYS

Figure 4.11: Pressure distribution on the aircraft's surfaces and symmetry plane.

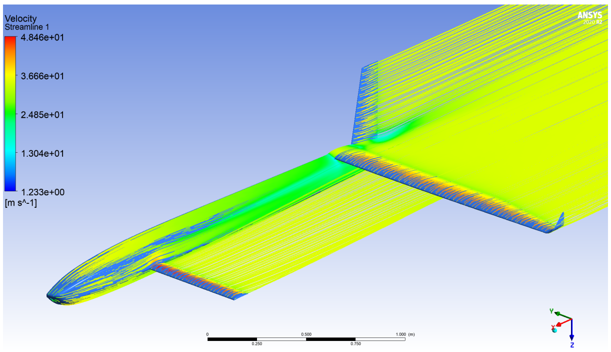
Velocity
Streamline 1
4.846e+01
3.666e+01
2.485e+01
1.304e+01
1.233e+00
[m s^-1]
ANSYS

Figure 4.12: Streamlines around the aircraft body.

Figure 4.13 shows the Tsai-Wu failure index from the structural results. In it, it is possible to certify that the aircraft is, in general, loaded far under the failure condition, which is to be expected since this is a nominal load case of $1g$. The region that shows higher stresses is the wing root region which is in accordance with the ultimate load case scenario studied in section 4.4. The maximum deformation of 0.031 m is estimated at the tip of the winglet, approximately 3.5 times lower than the maximum deformation in the $4.5g$ test.

4.5.2 Velocity Dependent Trim Condition

To characterize the aircraft at speeds besides the cruise condition, one can use the simulations evaluated in section 4.2 to find the trim condition at all speeds between the stall speed and the dash

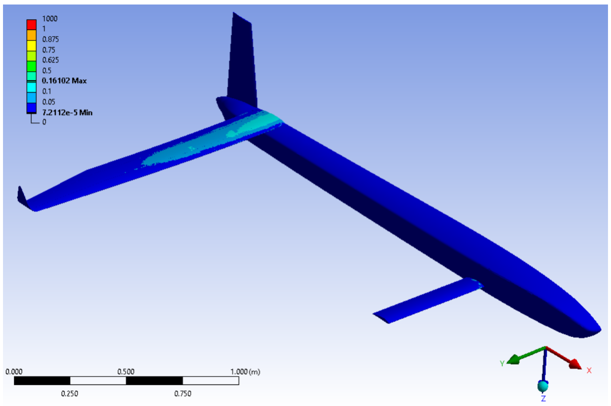

Figure 4.13: Tsai-Wu failure index on aircraft structure from cruise speed two-way FSI.

speed. Figure 4.14 shows the plots of the C_L, C_D, and C_m vs α for the 68-109 configuration along with trend lines of these functions for the canard and for the wing plus fuselage. They are separated because both have independent angles of attack. One should take into consideration that the true angle of attack of the canard in the plots is $\alpha + i_{c_{trim_{V cruise}}}$ where $i_{c_{trim_{V cruise}}} = 0.602°$. The C_L and C_m trend lines are linear while the C_D is quadratic and all three only take into consideration the points up until $\alpha = 9°$ since after that angle the lifting surfaces enter the stall zone and their behavior is non-linear.

Similarly to the system of equations 4.2, one can use the system of equations 4.3 to calculate the trim condition at any speed. Instead of using variables V_{stall} and α, the solution to the system of equations will give the values of α and α'_c from which α_c can be calculated through $\alpha_c = \alpha'_c + i_{c_{trim_{V cruise}}}$. The C_L and C_m coefficients of each component are defined as $C_{L_{w+fus}} = m_{wf_1}\alpha + b_{wf_1}$, $C_{m_{w+fus}} = m_{wf_2}\alpha + b_{wf_2}$, $C_{L_c} = m_{c_1}\alpha'_c + b_{c_1}$ and $C_{m_c} = m_{c_2}\alpha'_c + b_{c_2}$ where the m and b terms are taken from the trend lines in the plots in figures 4.14.

$$\begin{cases} M = 0 \\ L_c + L_{w+fus} = m_i g \end{cases} \Leftrightarrow \begin{cases} C_{m_c} + C_{m_{w+fus}} = 0 \\ \frac{1}{2}\rho S_w V^2 (C_{L_c} + C_{L_{w+fus}}) = m_i g \end{cases} \Leftrightarrow$$
$$\Leftrightarrow \begin{cases} m_{c_2}\alpha'_c + b_{c_2} + m_{wf_2}\alpha + b_{wf_2} = 0 \\ \frac{1}{2}\rho S_w V^2 (m_{c_1}\alpha'_c + b_{c_1} + m_{wf_1}\alpha + b_{wf_1}) = m_i g \end{cases} . \tag{4.3}$$

Through the use of a *MATLAB* program, the system of equations was solved for speeds between 23 m/s and 60 m/s. From it, figures 4.15, 4.16(a), 4.16(b), 4.17(a), 4.17(b), 4.17(c), 4.18(a) and 4.18(b) were plotted. Figure 4.15 shows the L/D plotted against the airspeed.

At 23 m/s, the L/D is 16.5. It rises until 29 m/s where it has a value of 19.9. It then begins to decrease until it reaches a minimum of 6.4 at the dash speed. This shows that if during the mission there is a segment that allows for the aircraft to be flown at slower speeds, it would be beneficial from a range standpoint to fly at 29 m/s instead of 35 m/s.

Figures 4.16(a) and 4.16(b) plot the $C_{L_{trim}}$, $C_{L_{w+fus}}$, and C_{L_c} vs airspeed and Lift over Drag ratio vs

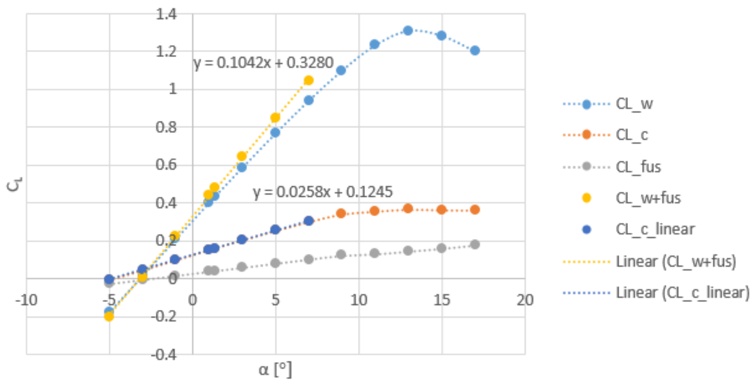

(a) C_L vs α plot.

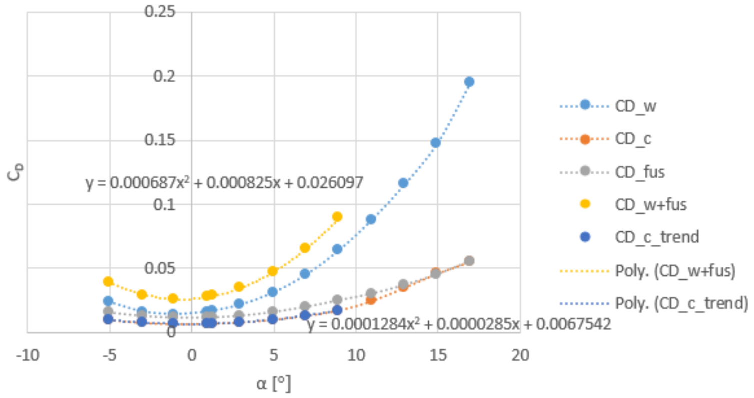

(b) C_D vs α plot.

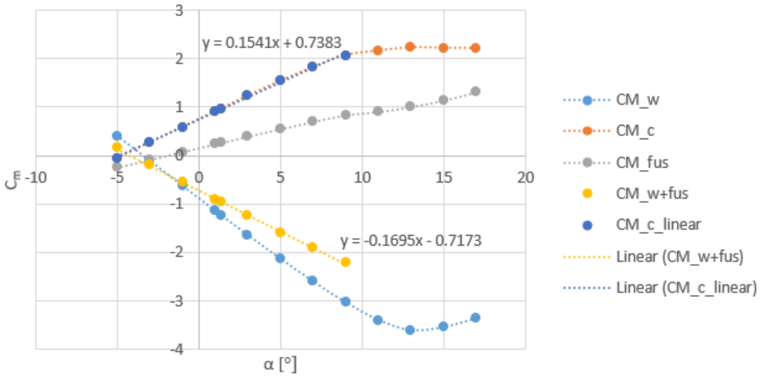

(c) C_m vs α plot.

Figure 4.14: C_L, C_D and C_m vs α plots with trendlines for all three coefficients.

$C_{L_{trim}}$ respectively.

The maximum C_L value the aircraft is able to produce is 1.48. From it, 77 % comes from the wing while 23 % originates from the canard. The C_L then decreases with the square of the velocity until a value of 0.217 at 60 m/s. In this situation, the canard has a bigger contribution, producing a third of the total lift, while the wing produces 67 %. It is also possible to see that the maximum L/D value occurs for a C_L value of 0.93.

Figures 4.17(a), 4.17(b) and 4.17(c) show the trim condition angles as a function of the aircraft speed.

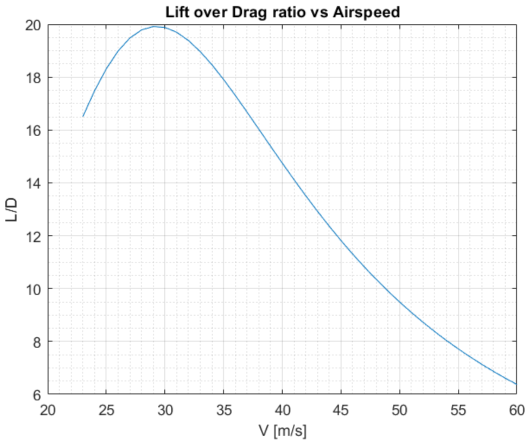

Figure 4.15: Lift over Drag ratio for different forward velocities.

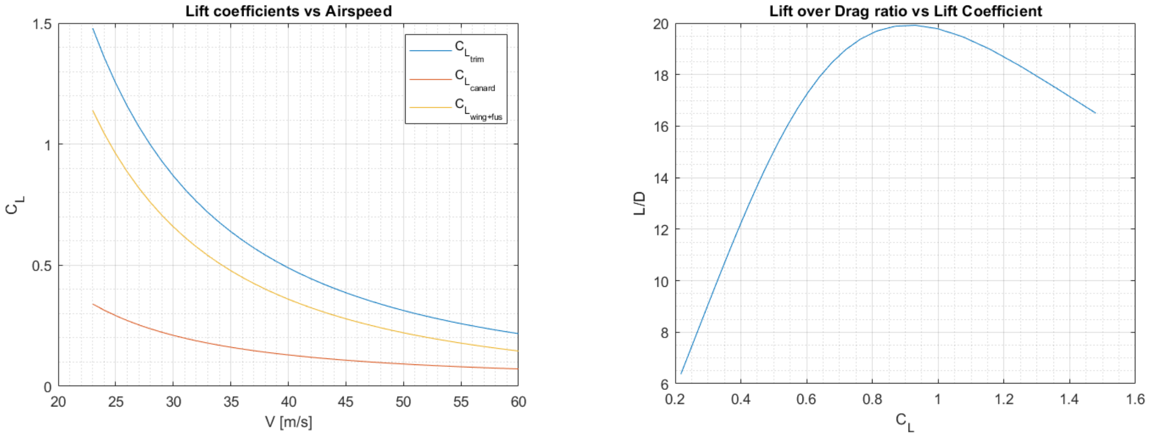

(a) $C_{L_{trim}}$, $C_{L_{w+fus}}$, and C_{L_c} vs airspeed plot.

(b) L/D vs $C_{L_{trim}}$ plot.

Figure 4.16: $C_{L_{trim}}$, $C_{L_{w+fus}}$, and C_{L_c} vs airspeed and Lift over Drag ratio vs $C_{L_{trim}}$ plots.

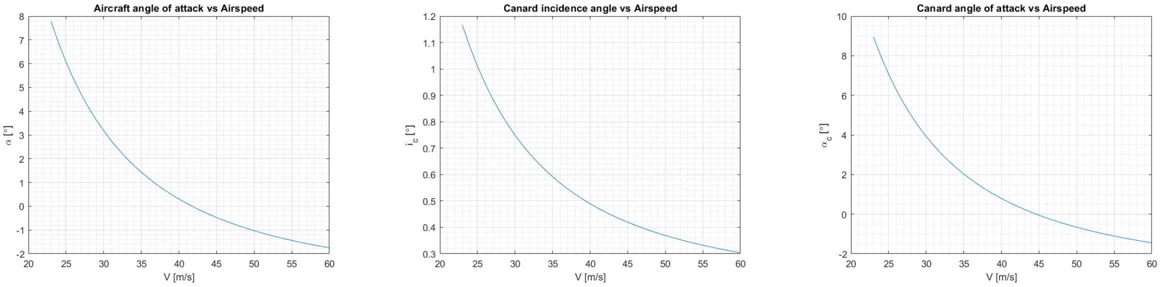

(a) Trimmed α.

(b) Trimmed i_c.

(c) Trimmed α_c.

Figure 4.17: Trimmed angles for different forward velocities.

The maximum and minimum α values are 7.784° and -1.750°. The maximum and minimum i_c angles are 1.165° and 0.304°. The resulting maximum and minimum α_c are 8.949° and -1.446°. The amplitude of the canard incidence angle is small, at only 0.861° of difference between the two extremes, so the canard is almost horizontal with the aircraft body for the trim condition, no matter the speed. Both the α and α_c range of angles are below 9° so the linear approximations used are still valid.

Figures 4.18(a) and 4.18(b) show the ideal power and thrust necessary from the propulsion system for each airspeed, calculated from the total drag.

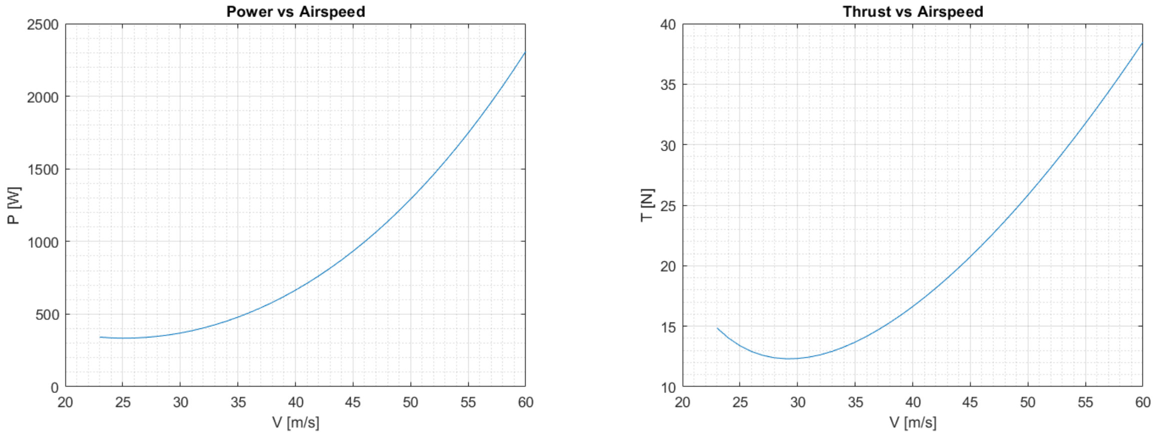

(a) Power.

(b) Thrust.

Figure 4.18: Power and Thrust required for trim condition for different forward velocities.

As expected, the required thrust for level flight has the inverse behavior of the L/D beginning to decrease until 29 m/s for a total thrust force of 12.3 N and increasing again until the dash speed. However, since the power required is directly proportional to the velocity of the aircraft, its minimum is 335 W for 25 m/s and it increases exponentially to 2309 W at the dash speed. During cruise, the required thrust and power levels are 13.7 N and 479 W respectively.

To validate these calculations, the dash speed trim performance was accessed through CFD. The trim angles were found to be $\alpha = -1.784°$, $\alpha_c = -1.415°$, and $i_c = 0.369°$. In comparison with the predicted values of $\alpha = -1.750°$, $\alpha_c = -1.446°$ and $i_c = 0.304°$, the errors are of 0.034° for α, 0.031° for α_c and 0.065° for i_c, all relatively small errors, which means that the predictions are correct. Furthermore, the L/D_{dash} was determined to be 7.114, a value 11.2 % higher than the predicted 6.4 from the *MATLAB* program. This means that the drag may be overestimated for high velocities.

4.6 Control Surfaces Design

The design of the control surfaces was based on empirical data. According to [44], the typical values for the geometry of the aileron in comparison with the wing are as follows:

- $\frac{b_{a_i}}{b_w} = 0.6 - 0.8;$
- $\frac{b_a}{b_w} = 0.2 - 0.4;$
- $\frac{c_a}{c_w} = 0.15 - 0.3;$
- $\frac{S_a}{S_w} = 0.03 - 0.12;$

Based on this information, the following values were chosen for the ailerons of this aircraft:

- $\frac{b_{a_i}}{b_w} = 0.72;$

- $\frac{b_a}{b_w} = 0.26;$
- $\frac{c_a}{c_w} = 0.25;$
- $\frac{S_a}{S_w} = 0.0558;$

These values make it so that the ailerons are located 0.03 m after the chord discontinuity and end 0.03 m before the beginning of the winglet. The aileron chord also leaves a small space to the rear spar so that there is no interference there. The total aileron area is also between the normal values. Figure 4.19 shows a top and an isometric view of the ailerons with a deflection of 30° , the maximum deflection chosen for the ailerons.

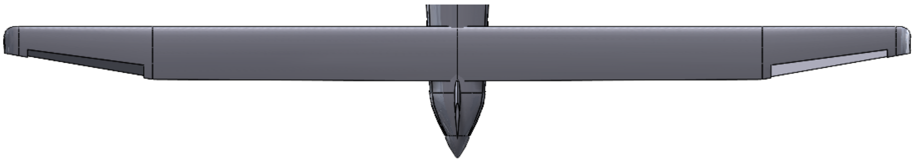

(a) Top view of ailerons.

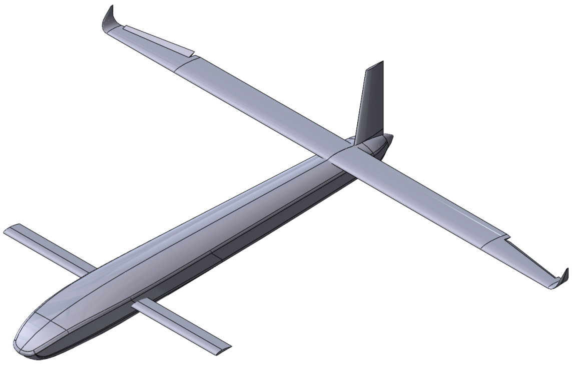

(b) Isometric view of ailerons.

Figure 4.19: Top and Isometric view of the aircraft with ailerons actuated.

Regarding the rudder, the typical values according to [44] are:

- $\frac{c_r}{c_f} = 0.2 - 0.42;$
- $\frac{S_r}{S_f} = 0.15 - 0.38;$

Taking this into consideration, the following values were chosen for the geometry of the rudder:

- $\frac{b_{r_i}}{b_f} = 0.05;$
- $\frac{b_r}{b_f} = 0.9;$
- $\frac{c_r}{c_f} = 0.25;$
- $\frac{S_r}{S_f} = 0.225;$

These values define a rudder that spans almost the entirety of the vertical fin, leaving a 0.02 m distance to the beginning and the end of the stabilizer. It also leaves a small distance to the spar at 70 % of the chord. Figure 4.20 shows a lateral and an isometric view of the vertical fin with a rudder deflection of -30° , which was considered the maximum negative deflection for this control surface.

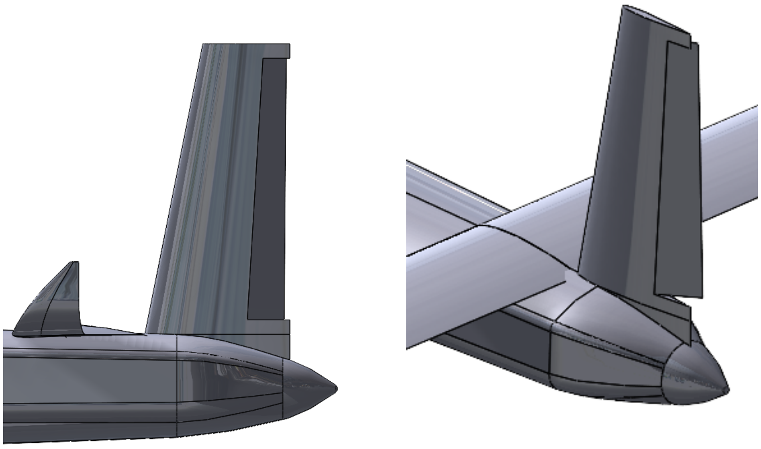
(a) Lateral view of rudder. (b) Isometric view of rudder.

Figure 4.20: Lateral and isometric view of the aircraft with rudder actuated.

4.7 Flight Dynamics Model

A Flight Dynamics Model of the aircraft allows for the simulation of its behavior in different flying scenarios. The first step in creating the FDM is getting the derivatives that characterize the motion of the aircraft according to the control inputs and the current aircraft state. Using the simulations from section 4.2, new simulations to get the control surfaces and the sideslip angle β coefficients and also the equations from appendix A to calculate the p, q, and r coefficients, table 4.3 was built. p, q, and r are the angular velocities in the three axes.

Another important piece of information that remains to be calculated is the inertia of the aircraft. Since most of the systems that will go on the aircraft have yet to be defined, their weight and dimensions are unknown. For this reason, some assumptions had to be made to estimate the inertia. All components were modeled as cylinders with a fixed radius and length that fit inside the fuselage. Their center of mass is in line with the center of the fuselage. Their longitudinal positions are based on special requisites of the MAD sensor. The MAD sensor detects magnetic fields and certain objects must be placed a certain distance away from it to not interfere with its activity. These distances were previously determined by CfAR and can be found in [45].

The inertia of the aircraft structure was taken from *Ansys Mechanical*. The fuel tank had to be placed in the aircraft CoG position because its location should remain in the same place whether the fuel tank is empty or full. The resulting dimensions and longitudinal placement of the different components can be found in table 4.4.

The resulting inertia matrix of the aircraft with the components inside is:

$$I = \begin{bmatrix} I_{xx} & I_{xy} & I_{xz} \\ I_{yx} & I_{yy} & I_{yz} \\ I_{zx} & I_{zy} & I_{zz} \end{bmatrix} = \begin{bmatrix} 0.97255 & 0 & -1.13462 \\ 0 & 16.2584 & 0 \\ -1.13462 & 0 & 17.1078 \end{bmatrix},$$

where the components I_{xz} and I_{zx} come from the structure FEM model.

Table 4.3: Aerodynamic derivatives. Coefficients signaled with * have a symmetric behavior whether the angle is positive or negative.

Derivative [/rad]	Value	Derivative [/rad]	Value
C_{D_0}	0.03291	C_{l_β}	-0.08861
$C_{D_{\alpha_1}}$	0.04727	C_{l_p}	-0.69866
$C_{D_{\alpha_2}}$	2.25529	C_{l_r}	0.09931
$C_{D_\beta}*$	-0.01184	$C_{l_{aileron}}$	0.23158
$C_{D_{\alpha_{c_1}}}$	0.00719	$C_{l_{rudder}}$	0.01574
$C_{D_{\alpha_{c_2}}}$	0.42151		
$C_{D_{aileron}}*$	0.04728		
$C_{D_{rudder}}*$	0.03522		
C_{Y_β}	-0.64194	C_{m_0}	-0.08328
C_{Y_r}	0.27518	C_{m_α}	-0.70292
$C_{Y_{aileron}}$	0.00376	$C_{m_\beta}*$	0.08852
$C_{Y_{rudder}}$	0.26348	$C_{m_{i_c}}$	9.55036
		C_{m_q}	-171.827
		$C_{m_{aileron}}*$	0.15325
		$C_{m_{rudder}}*$	0.05625
C_{L_0}	0.45344	C_{n_β}	0.02558
C_{L_α}	7.30472	C_{n_p}	-0.03796
$C_{L_\beta}*$	-0.06921	C_{n_r}	-0.05898
$C_{L_{i_c}}$	1.29298	$C_{n_{aileron}}$	0.00124
C_{L_q}	12.1834	$C_{n_{rudder}}$	-0.06027
$C_{L_{aileron}}*$	-0.04968		
$C_{L_{rudder}}*$	-0.00536		

Table 4.4: Aircraft component list.

	Structure	Payload	Fuel Tank	Batteries	Electric Eng.	Other	Gas Eng.	Ballast
mass [kg]	3.386	3	5	4.5	0.5	4.244	3	1.37
CoG$_x$ [m]	0.11	1.427	0	-0.323	-0.323	-0.623	-0.873	1.627
Radius [m]	-	0.1	0.08	0.07	0.04	0.06	0.125	0.025
Length [m]	-	0.3	0.35	0.2	0.05	0.35	0.2	0.05

With the inertia and the aerodynamic coefficients defined, a *Simulink* model was created. Running this model starts with a *MATLAB* script that defines all the aircraft properties as well as the initial state, which includes the initial position, velocity, Euler angles, and angular velocity. The model then simulates the aircraft behavior until a certain end time based on the control inputs δ_{i_c} (canard incidence angle), δ_A (aileron deflection angle), δ_R (rudder deflection angle) and δ_T (thrust percentage) and the current state of the aircraft. It calculates and sums all the forces and moments from each variable and inserts them in the 6 DOF EOM subsystem that calculates the linear and angular accelerations of the aircraft taking into account its mass and inertia to determine the new state of the aircraft.

When the Flight Control System (FCM) of this aircraft is designed, it can be implemented with this FDM by taking the current state vector, calculating the control inputs, and inserting them in the dynamic model. Figure 4.21 shows the general FDM architecture, while figure 4.22 shows the Subsystem Dynamic Model where the calculations of the forces and moments happen.

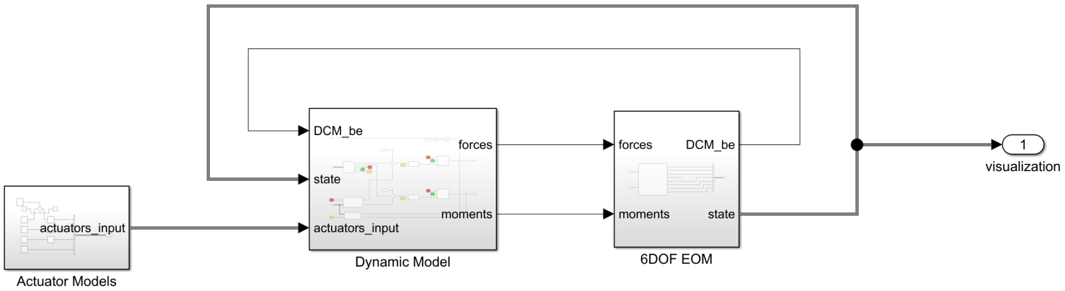
DCM_be
state
actuators_input
forces
moments
Dynamic Model
forces
DCM_be
moments
state
6DOF EOM
Actuator Models
1
visualization

Figure 4.21: Flight Dynamics Model architecture.

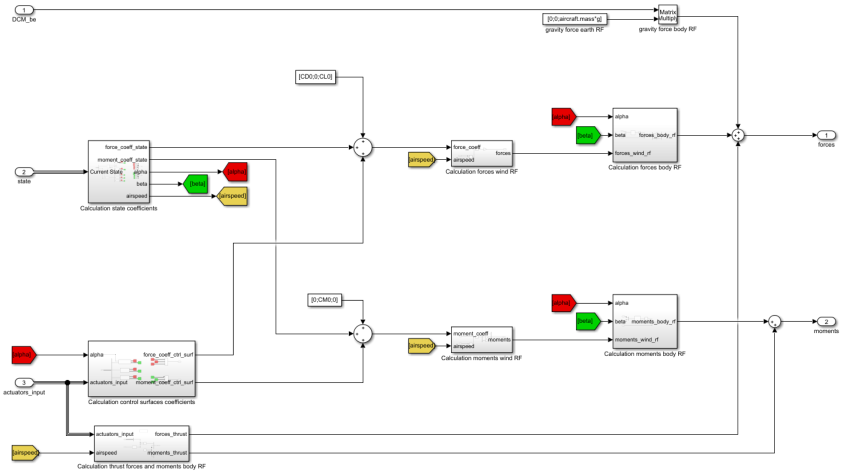
DCM_be
state
actuators_input
Calculation state coefficients
Calculation forces wind RF
Calculation forces body RF
Calculation moments wind RF
Calculation moments body RF
Calculation control surfaces coefficients
Calculation thrust forces and moments body RF
gravity force earth RF
gravity force body RF
forces
moments

Figure 4.22: Dynamic Model subsystem architecture.

4.8 Stability

To determine the aircraft stability characteristics at the trim condition for different velocities, another *MATLAB* program was constructed. This program takes the trim conditions calculated in section 4.5.2 and solves equation 2.20 to calculate the eigenvalues for both longitudinal and lateral modes.

Figures 4.23(a) and 4.23(b) show the evolution of the longitudinal complex poles for different airspeeds. The red circles correspond to the poles at 23 m/s, the black circles to the 35 m/s cruise speed, and the green circles to the 60 m/s dash speed.

Both longitudinal modes are stable since they are always in the negative real axis. The phugoid mode shape is characterized by a low damping, low-frequency movement, while the short-period has a higher damping and a shorter period, like the name suggests. The phugoid damping is higher at slower speeds, initially decreasing along with the frequency until around the cruise speed and then starting to increase again until the dash speed. The short-period damping tends to remain very high no matter the speed, while the frequency tends to increase the faster the aircraft goes.

Figures 4.24(a), 4.24(b), and 4.24(c) show the evolution of the lateral poles for different airspeeds. The circle color scheme is the same as in the longitudinal case.

It is possible to see that the Dutch roll mode tends to have constant damping while the frequency gets higher the faster the aircraft flies. The roll mode is highly damped and it increases even more the

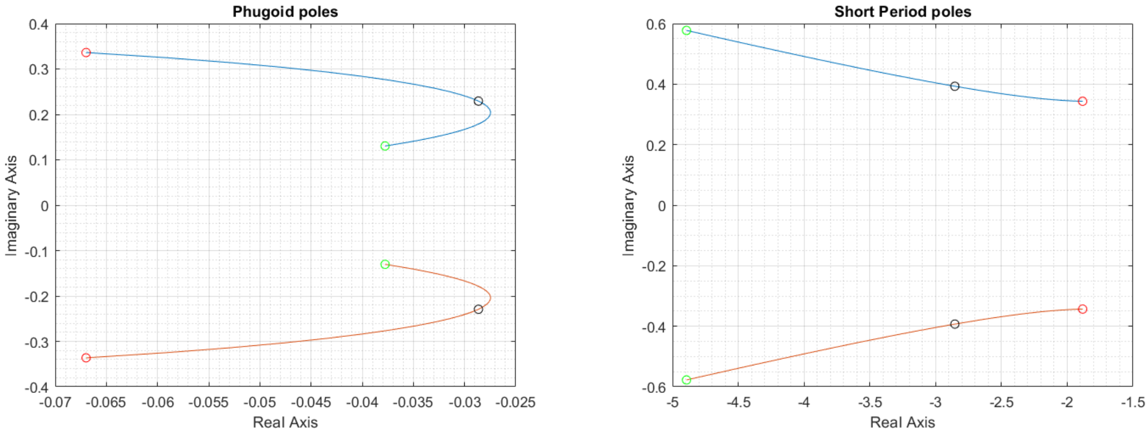

(a) Phugoid Poles Evolution.

(b) Short-Period Poles Evolution.

Figure 4.23: Eigenvalue evolution for longitudinal motion.

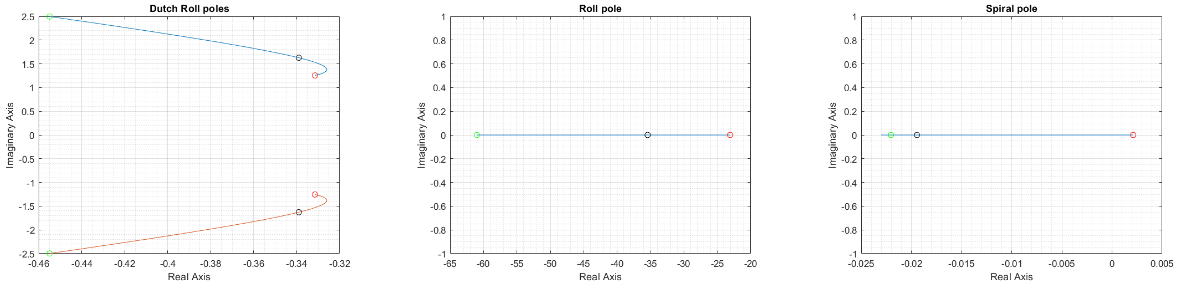

(a) Dutch Roll Poles Evolution.

(b) Roll Pole Evolution.

(c) Spiral Pole Evolution.

Figure 4.24: Eigenvalue evolution for lateral motion.

closer to the dash speed the aircraft is flying at. The spiral mode is the only non-stable mode, but only at very slow speeds, as the real part of the mode crosses to the negative side at 24 m/s where it then tends to stabilize with low damping.

The *Simulink* model can be cross-checked with this *MATLAB* program. By subjecting the aircraft to a canard pulse, one can excite the short-period and phugoid longitudinal modes. By analyzing the forward velocity plot from figure 4.25, one can get the period for the phugoid mode by checking the time interval between two peaks. In this case, where the trim speed was set to 35 m/s, the period was found to be 27.27 s. The *MATLAB* program calculates a value of 27.19 s, so there is only a 0.3 % error between the two methods. The short-period should be recognizable from the α behavior, but the 99 % damping of this mode made it impossible to see the period on the FDM simulation. Still, the *MATLAB* program calculates a 2.18 s period.

The Dutch roll can also be analyzed by introducing an aileron pulse as seen in figure 4.26 or by a rudder pulse. Looking at the angular velocity p one can obtain a 3.71 s period for this mode. The *MATLAB* program provided a 3.68 s value, so once again a less than 1 % error which means that both models behave similarly.

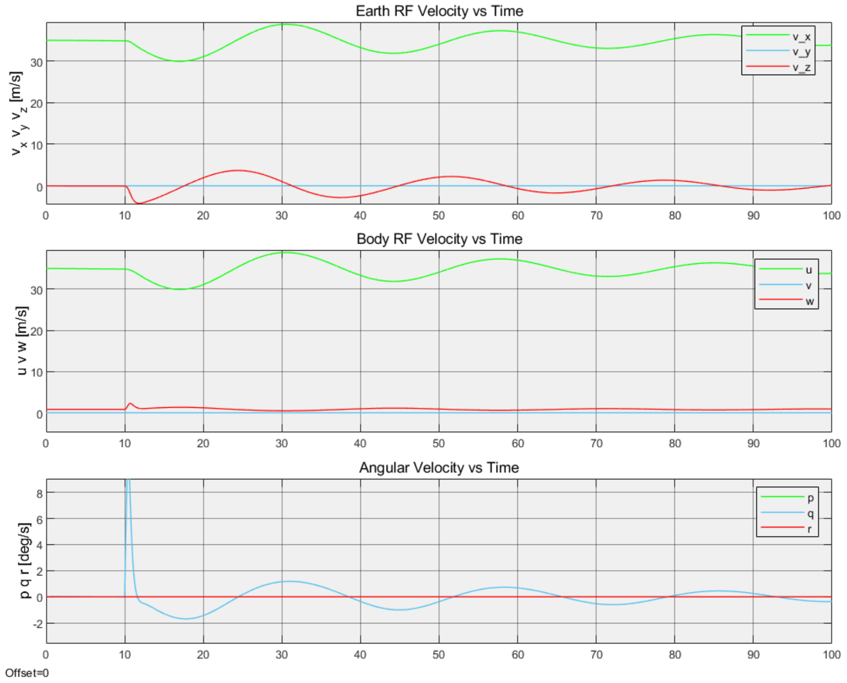

Figure 4.25: 1° canard half a second pulse dynamic simulation at 35 m/s.

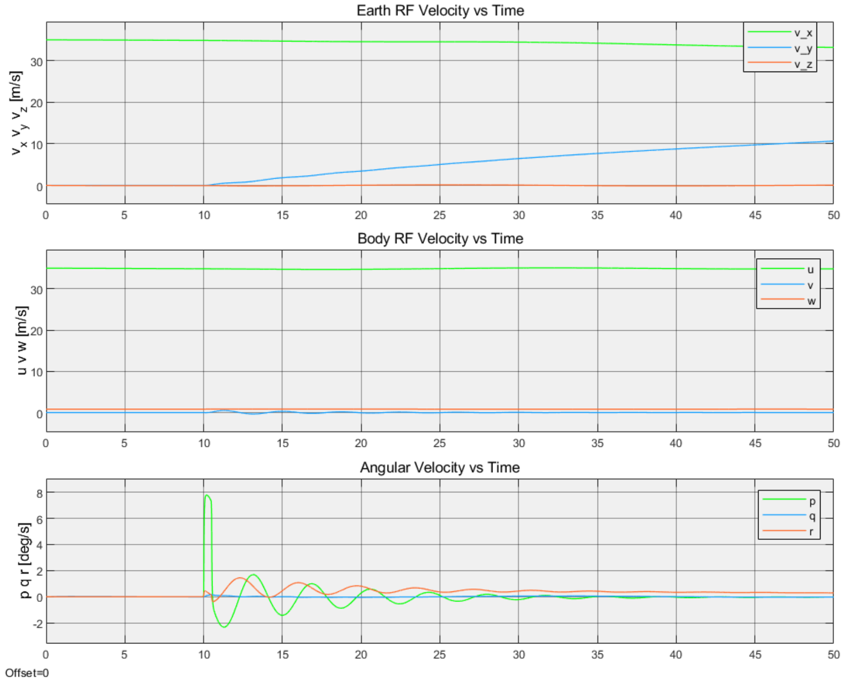

Figure 4.26: 1° aileron half a second pulse dynamic simulation at 35 m/s.

Chapter 5

Experimental Testing

In order to validate the FE model of the wing, static load tests as well as GVT were performed on a manufactured sample. This chapter is dedicated to the explanation of the manufacturing and testing processes and to the discussion of the results obtained.

5.1 Manufacturing

The composite wing was manufactured using the open mold hand lay-up process. The first step was designing the molds using *SOLIDWORKS* which have the negative OML of the wing. Figure 5.1 shows the assembly of all the mold parts and a close-up of the tip region of these molds is depicted in figure 5.2.

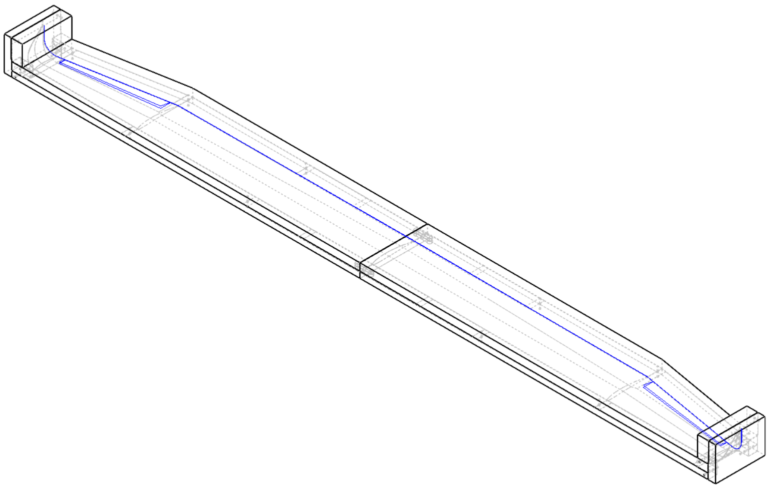

Figure 5.1: CAD Mold assembly.

The molds were divided in eight pieces, four of which are symmetrical to the other four. The wing skin was divided along the leading and trailing edges, resulting in a separation between the top and bottom surfaces. Each surface was divided in four different molds, two on each side, one for the planar wing surface and another for the winglet.

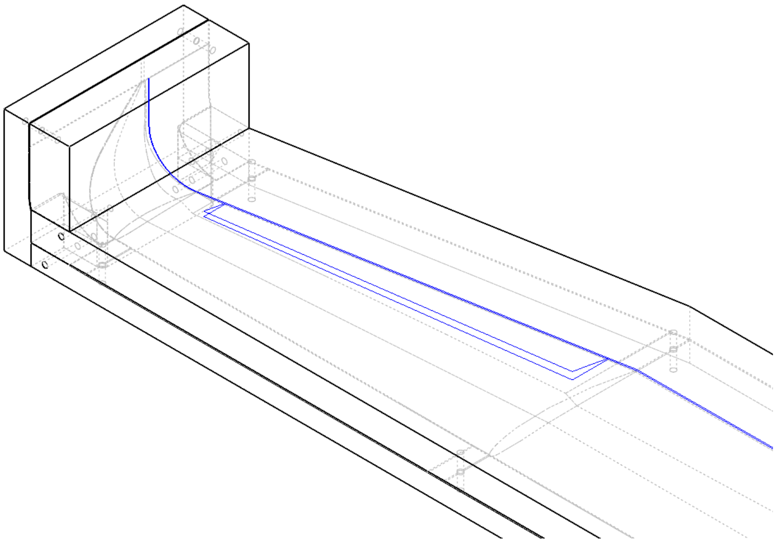

Figure 5.2: Close-up of the wingtips mold CAD assembly.

The molds were designed in a way that allows for the sliding of the four molds of the top surface inside the four molds of the bottom surface and holes for dowel pins were machined on both sides to allow for the alignment of the leading and trailing edges when gluing the two composite skins that will come from each side.

Medium Density Fiberboard (MDF) sheets with 3/4 inches of thickness were cut and glued together using wood glue until the necessary mold thickness was achieved, forming MDF blocks. These were machined with a Computer Numerical Control (CNC) machine to get the mold shapes. Each winglet mold was glued together to their respective wing mold. The left and right halves of each surface's molds were not glued together but connected with 3D printed pieces instead, which allows for easier maneuvering and storage of the molds.

The composite flashing, *i.e*, the composite laminate that exceeds the leading and trailing edge also had to be taken into account. The thickness of each laminate section had to be removed from the surface of the molds ranging from 1.5 mm at the root of the top surface to 0.4 mm in the winglet surface. The trailing edge line and the aileron lines were also machined into the molds which leaves a mark on the composite laminate so that it is easier to cut both surfaces in the correct place after they are glued together.

After the machining of the MDF blocks, the surface was sanded and sealed using epoxy resin. Otherwise, the composite laminate would likely stick to the molds and it would be impossible to separate the two without damaging them. Moreover, a mold release agent was spread on the mold surface before each hand lay-up process to ensure that the piece would not stick to the mold.

Figures 5.3(a) and 5.3(b) show pictures of the manufactured lower and upper molds, respectively.

Each wing skin was then manufactured. This process involves cutting UD and woven carbon fiber rolls into sheets with the dimensions of the plies from the wing structure, spreading epoxy resin on top of them, and laying the impregnated sheets on top of the molds. To soak extra epoxy resin from the composite pieces and make them lighter a breathing cloth is put on top of the laminate with a plastic

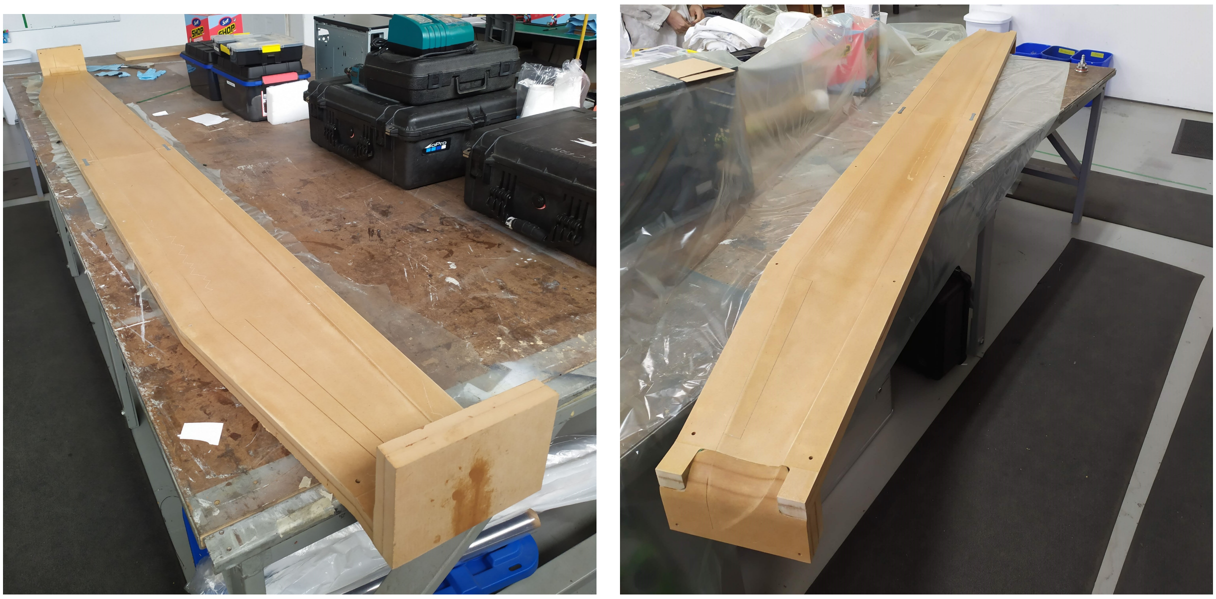

(a) Lower surface molds.

(b) Upper surface molds.

Figure 5.3: Manufactured molds.

peel ply in the middle. A vacuum bag and a vacuum machine are then used to make the composite layers adhere to the shape of the mold while the epoxy resin cures. Figure 5.4(a) shows the lower surface after the hand lay-up process still under vacuum while the resin was curing and figure 5.4(b) shows the composite piece after the vacuum bag, breathing cloth and plastic peel were removed.

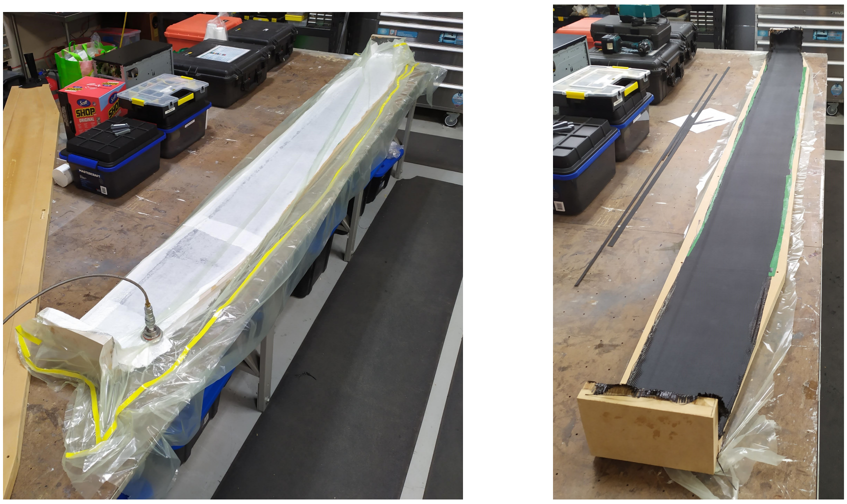

(a) Lower surface curing under vacuum.

(b) Lower surface after cure resting on the mold.

Figure 5.4: Manufacturing of the lower surface.

The spars were manufactured on a flat table, but the lay-up process was the same as for the skins. Because of the angle change at the chord discontinuity, each spar was divided into three pieces, one middle piece and two tip pieces.

An extra part was added to the internal structure of the wing that is not in the Finite Element (FE) model. This part is a 6 mm thick carbon fiber rib with the shape of the airfoil that was placed at the root of the wing. It will serve as a support to an aluminum plate that will be used to fix the wing during the static load tests. The rib was divided into three sections with cuts where the spars cross the root of the wing.

The spars and rib were then glued with epoxy resin to the top surface of the wing in their respective locations. After the resin cured, the internal elements were sanded until the lower surface fitted correctly on the upper surface. Figure 5.5 shows the internal structure already glued to the upper surface inside the upper molds and the lower surface out of the molds.

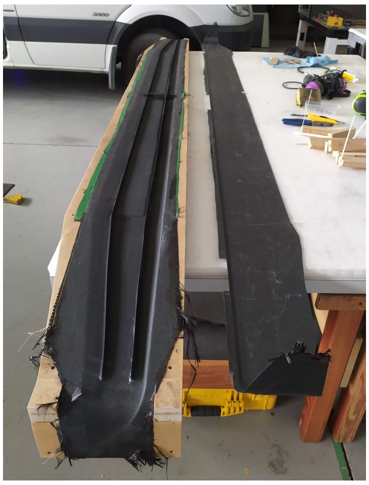

Figure 5.5: Internal structure glued to the upper surface and lower surface.

The next step was gluing the lower surface to the rest of the structure. Epoxy resin was applied to the leading and trailing edges and to the upper edges of the spars to ensure the connection between both surfaces.

After the epoxy resin cured, the last step is to cut the composite flashing and the aileron cut-outs and fill any holes in the leading edge that may have appeared. Figure 5.6 shows a picture of the manufactured wing.

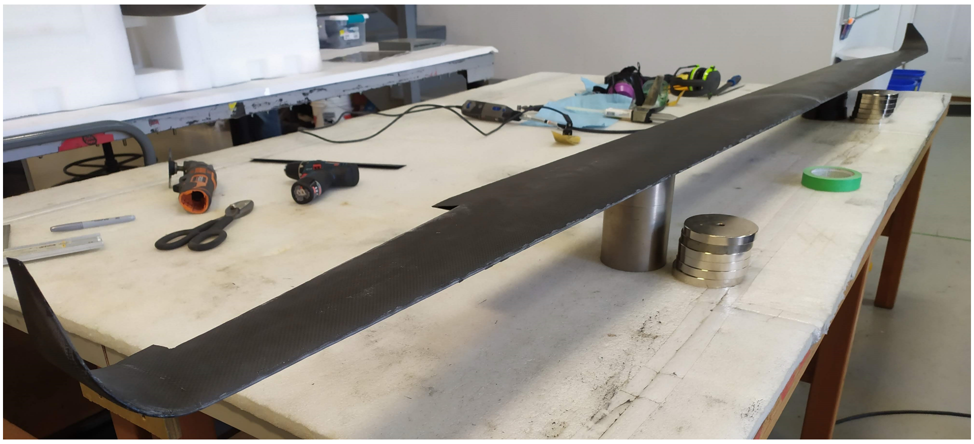

Figure 5.6: Manufactured wing.

The manufactured wing had a final mass of 1.716 kg, 32.5 % heavier than the expected mass of the FE model of the wing without ailerons of 1.295 kg. This increase in mass may be due to several reasons. First, the middle rib was not included in the FE model and its mass was approximately 20 g. Second, about 200 g of epoxy resin were used when gluing the internal structure and both surfaces of the wing together and this was also not included in the FE model. Besides those two points, the extra mass probably came from excess resin that was used in the lay-up process and that contributes to the laminate weight.

5.2 Ground Vibration Testing

The first performed test on the wing was the GVT.

The wing was supported by a cable to simulate a free-free boundary condition as close as possible. Four uniaxial sensors were placed on the wing and one of the winglets to collect accelerations and through a previously developed *LabView* interface, the FRFs were computed by making use of the data also collected from the impact hammer. Figure 5.7(a) shows the cables that held the wing from the ceiling and figure 5.7(b) shows the four sensors positioned on the wing.

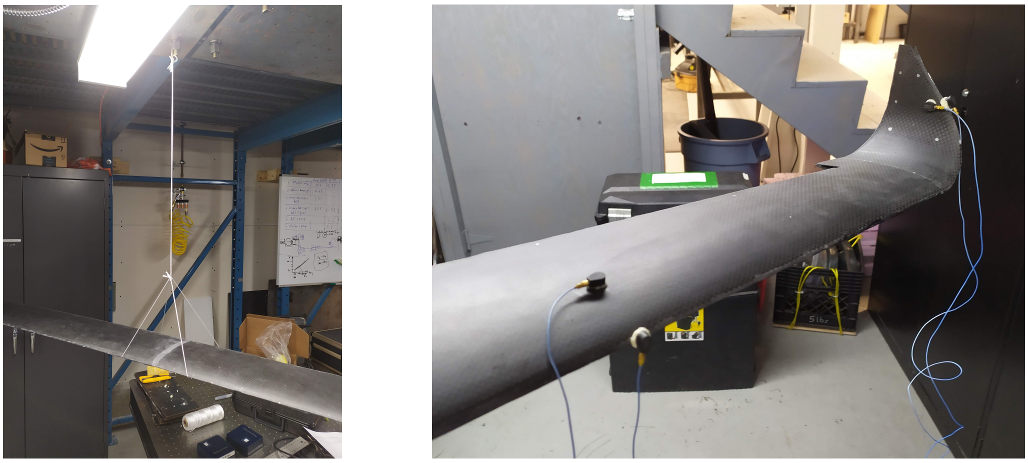

(a) Cable support that held the wing.

(b) Sensors mounted on the wing.

Figure 5.7: Setup of the wing for GVT.

Both out-of-plane and in-plane information was collected, adding to a total of 54 locations on the wing where either the impact hammer hit or the sensors were placed and a total of 81 Degrees of Freedom (DOFs). The distribution of the locations and DOFs can be seen in Table 5.1.

The location of the sensors and DOF measured are available in table 5.2. The reference frame in the direction column is the same as in figure 2.2.

The frequency range of interest for this wing was considered to be from 0 Hz until 200 Hz. For this reason, the impact hammer was equipped with a soft tip. Three successful hits per point were necessary to collect the FRFs.

The collected data was then processed with *MEScope* where a model of the wing defined by the impact points was built to post-process the data. The movement of the points where the sensors were located had to be interpolated since there were no FRFs obtained there. Additionally, it was not possible

Table 5.1: Impact locations and Degrees of Freedom.

Location #	Structure	Out-of-Plane DOFs #	In-plane DOFs #
1 - 11	Right LE	1 - 11	55 - 65
12 - 21	Left LE	12 - 21	66 - 75
22 - 32	Right TE	22 - 32	N.A.
33 - 42	Left TE	33 - 42	N.A.
43 - 45	Right winglet LE	43 - 45	76 - 78
46 - 48	Right winglet TE	46 - 48	N.A.
49 - 51	Left winglet LE	49 - 51	79 - 81
52 - 54	Left winglet TE	52 - 54	N.A.

Table 5.2: Sensor locations and Degrees of Freedom.

Sensor #	Location #	Direction	DOF #
1	19	-z	19
2	19	-x	73
3	50	y	50
4	50	-x	80

to perform valid hammer hits on the tips of the winglets due to their high flexibility, so the two last points of each winglet were also interpolated.

To compare the GVT results to the FE model, a modal analysis as described in section 2.6 was performed. For this modal analysis, the entire wing was in the model and the ailerons were cut out for the computational results to be as similar as possible to the testing conditions. There were also no boundary conditions applied.

Figure 5.8(a) shows the FE model of the wing in *Ansys Mechanical* and figure 5.8(b) shows the model of the wing in *MEScope*.

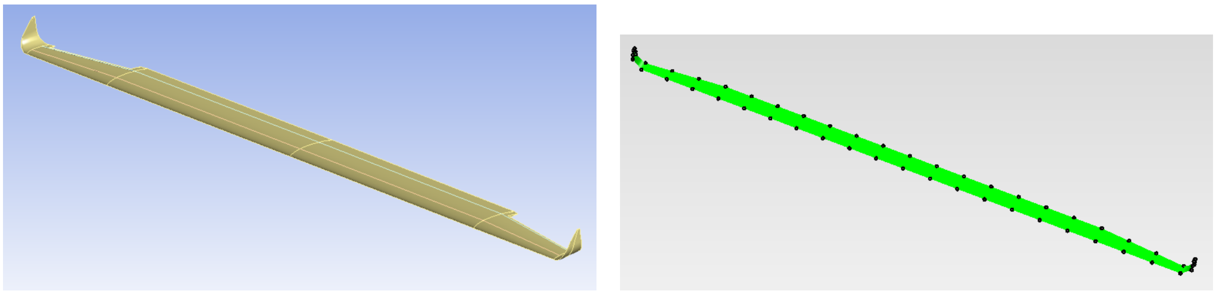

(a) FE model of the wing.

(b) *MEScope* model of the wing.

Figure 5.8: FE model from *Ansys* and *MEScope* model of the wing.

5.2.1 Mode shape analysis

The computational and experimental results were used to build table 5.3. It shows the modes whose frequencies are under 200 Hz, the disparity between both acquired frequencies as well as the damping from the GVT. Some abbreviations were used to describe the mode shape: *anti.* means anti-symmetrical, *sym.* means symmetrical, *OP* means out-of-plane and *IP* means in-plane.

Table 5.3: Wing mode shapes and respective natural frequencies.

Mode #	Mode shape	f_{FEA} [Hz]	f_{GVT} [Hz]	Δf [%]	ζ [%]
1	1st OP sym. bending	23.1	25.8	+11.7	1.2
2	1st OP anti. bending	46.3	43.8	-5.4	0.3
3	1st torsion	67.4	81.1	+20.3	0.4
4	2nd OP sym. bending	77.4	74.5	-3.7	1.1
5	2nd OP anti. bending	108.6	107.0	-1.5	0.8
6	2nd torsion	121.1	132.0	+9.0	1.1
7	3rd OP sym. bending	161.9	158.0	-2.4	0.2
8	1st IP sym. bending	172.5	158.0	-8.4	0.6
9	3rd torsion	178.2	197.0	+10.5	1.0

In general, the frequencies obtained from both methods tend to match well, with errors under 12 % except for the 1st torsion mode with an error of 20.3 %. In fact, all three detected torsion modes were among the highest error levels which means that while the bending was better predicted, the composite model needs updating to better predict the torsion.

Figures 5.9, 5.10, 5.11, 5.12, 5.13, 5.14, 5.15, 5.16, and 5.17 show all nine mode shapes from both FEA and GVT, in order.

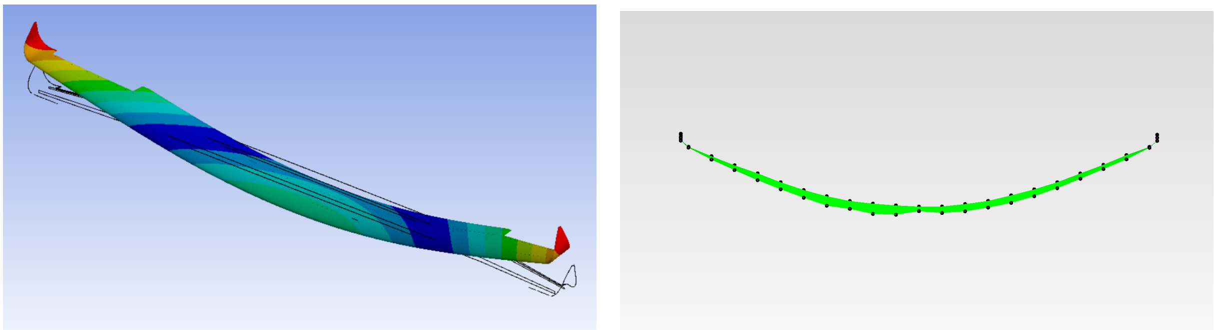

(a) 1st FEA mode shape.

(b) 1st GVT mode shape.

Figure 5.9: 1st out-of-plane symmetrical bending.

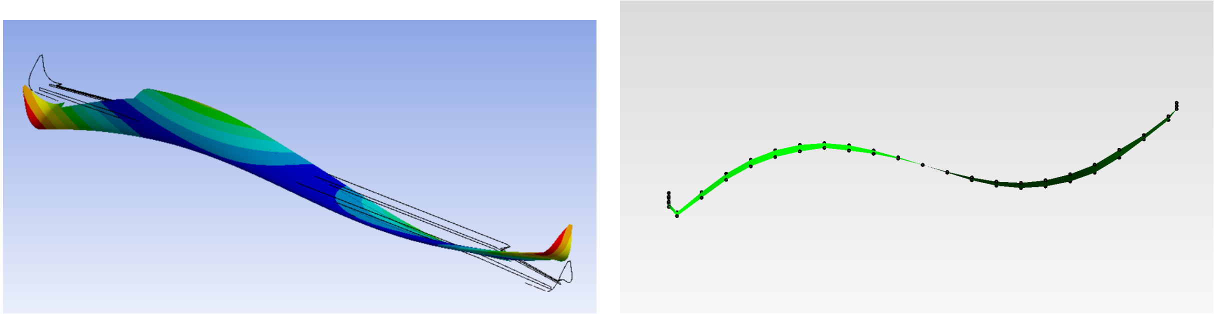

(a) 2nd FEA mode shape.

(b) 2nd GVT mode shape.

Figure 5.10: 1st out-of-plane anti-symmetrical bending.

Furthermore, two winglet mode shapes were also detected in both the FE model and the GVT.

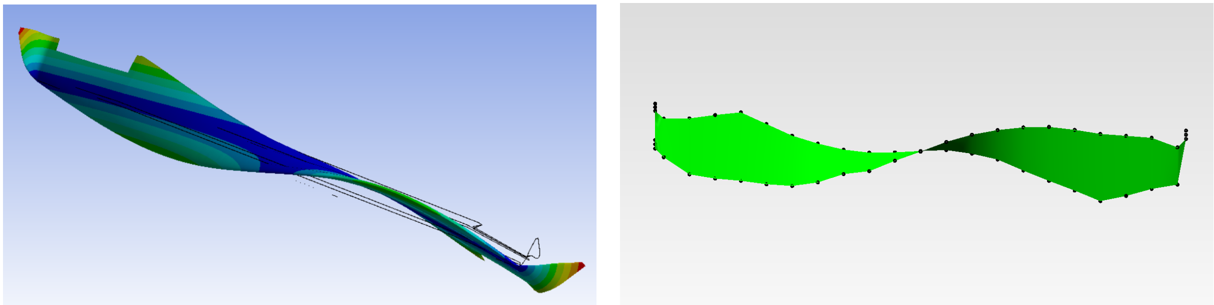
(a) 3rd FEA mode shape.
(b) 3rd GVT mode shape.

Figure 5.11: 1st torsion mode shape.

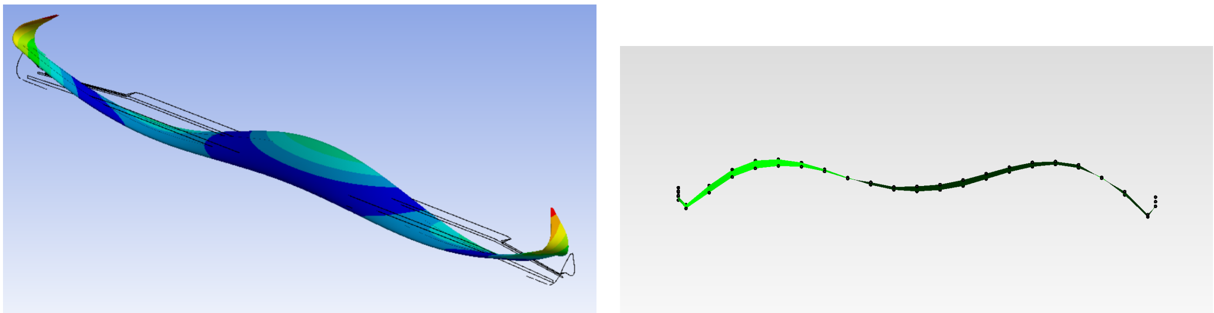
(a) 4th FEA mode shape.
(b) 4th GVT mode shape.

Figure 5.12: 2nd out-of-plane symmetrical bending.

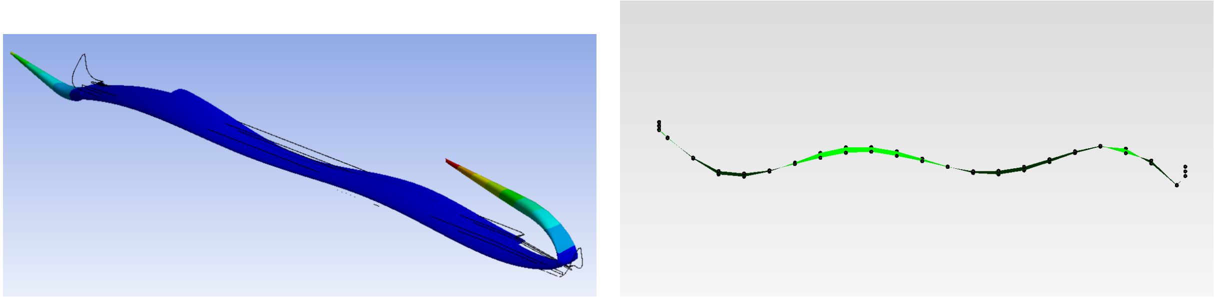
(a) 5th FEA mode shape.
(b) 5th GVT mode shape.

Figure 5.13: 2nd out-of-plane anti-symmetrical bending.

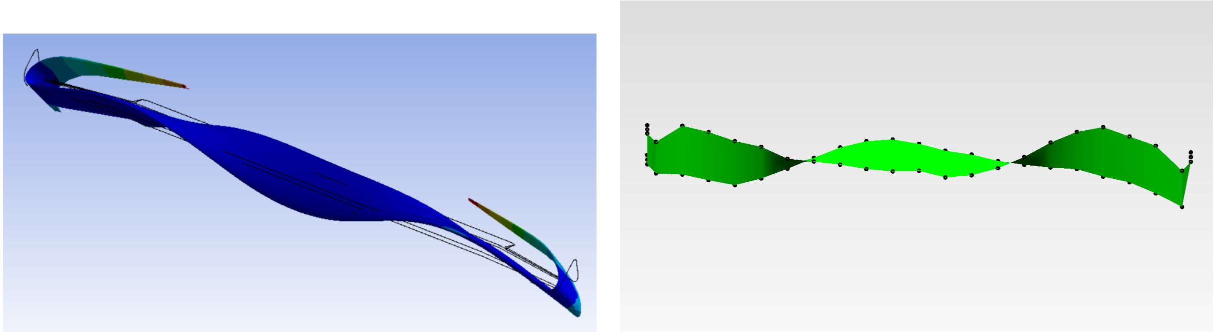
(a) 6th FEA mode shape.
(b) 6th GVT mode shape.

Figure 5.14: 2nd torsion mode shape.

Modal analysis on *Ansys* revealed an OP symmetrical bending at 109.6 Hz and an OP anti-symmetrical bending at 124.3 Hz. From the GVT, it was possible to detect OP symmetrical bending at 106.5 Hz and

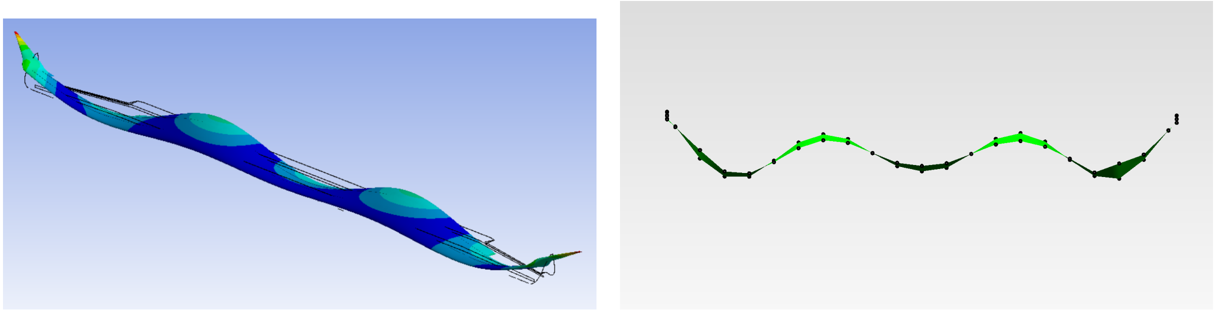

(a) 7th FEA mode shape.

(b) 7th GVT mode shape.

Figure 5.15: 3rd out-of-plane symmetrical bending.

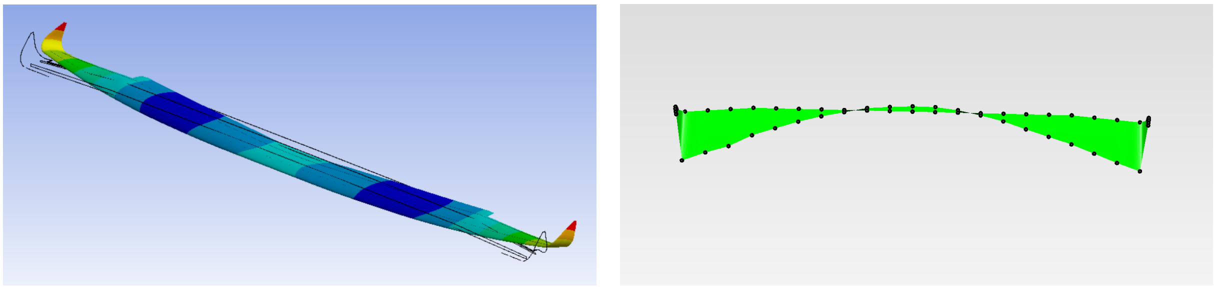

(a) 8th FEA mode shape.

(b) 8th GVT mode shape.

Figure 5.16: 1st in-plane symmetrical bending.

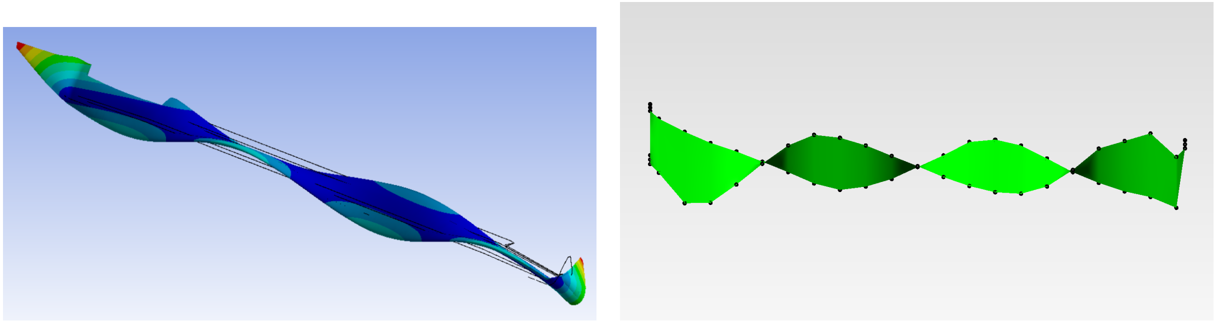

(a) 9th FEA mode shape.

(b) 9th GVT mode shape.

Figure 5.17: 3rd torsion mode shape.

OP anti-symmetrical bending at 121 Hz which gives an error of 2.8 % for the former mode shape and an error of 2.7 % for the latter.

Moreover, three Rigid-Body Motions (RBM) frequencies were detected. The first was a rotating movement around the x-axis at 0.885 Hz. The second was a rotating movement around the y-axis at 4.98 Hz. The final and third RBM was a translation motion in the z-axis at 10.9 Hz. These frequencies are related to the setup of the cable that holds the wing. Since all three frequencies are far enough below the frequency of the first mode shape, there was no need to change the way the wing was supported to confirm they correspond to RBM.

5.3 Wing Static Loading

As mentioned previously, the rib that was placed at the root of the wing served as a support to an aluminum plate. This aluminum plate was not glued to the wing during the GVT tests because it would interfere with the results. However, before the static loading tests, the aluminum plate had to be rigidly secured to the wing. This plate was divided into two parts, one with a cut out with the shape of the top of the airfoil and the other with a cut out of the bottom part of the airfoil. First, the two parts were clamped using bolts against the wing where the rib was located and then a small carbon fiber reinforcement was used to glue the aluminum to the wing skin. This aluminum plate was then bolted against a metal support that was secured to the ceiling to secure the wing in a fixed position.

The wing lift was simulated through the use of iron weights and sandbags. Since the lift points upwards and the weight of these masses point downwards, the wing was fixed upside down.

Figure 5.18(a) shows the right half of the wing and the aluminum plate and figure 5.18(b) shows the wing fixed on the metal support.

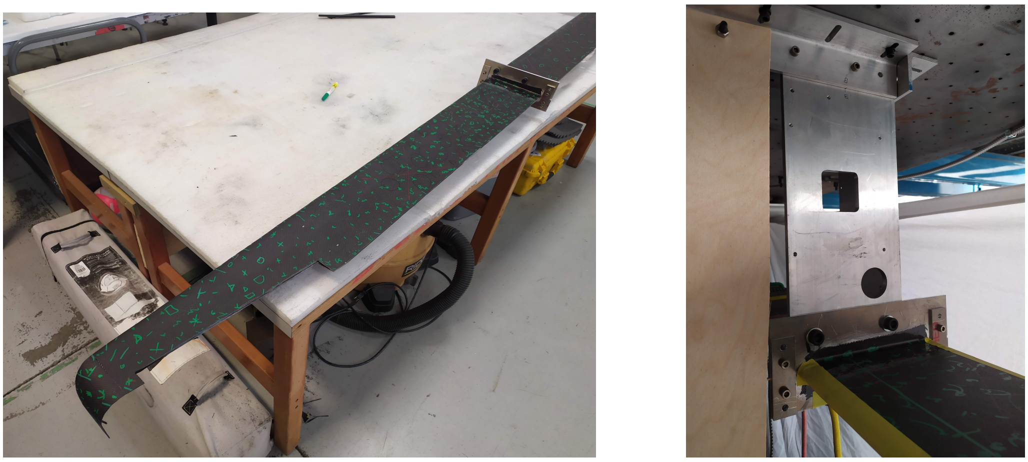

(a) Aluminum plate connected to the wing.

(b) Wing support to the ceiling.

Figure 5.18: Wing fixed support setup for static load tests.

5.3.1 Photogrammetry

For a better analysis of the deformation of the wing under loading, a photogrammetry software called *Regard3D* was used. The technique this program uses consists of extracting 3D information from photographs of an object to reconstruct it into a 3D model.

It was found that more saturated colors and higher contrast between objects helped achieve better accuracy of the 3D model. For this reason, the leading and trailing edges were covered with yellow tape and the top surface of the wing was covered with green tape. Furthermore, to align the undeformed and deformed shapes, the ceiling and a wood board placed in the plane of the wing root chord were used as reference entities. Both also had yellow and green strips of tape so that they could be more easily identified. Only the right half of the wing was used to get the 3D model, but both halves were loaded simultaneously so that there was little moment being transferred to the support structure. Figure 5.19 shows a picture of the setup of the wing and the reference planes ready for photogrammetry.

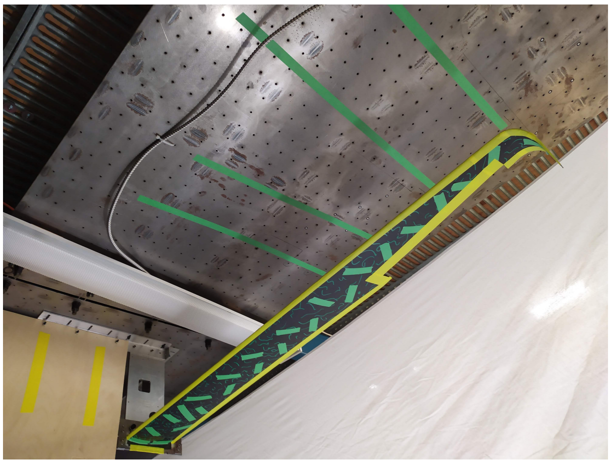

Figure 5.19: Setup of the wing before static load tests.

To get the shape in the loaded and unloaded conditions, multiple photographs had to be taken from multiple perspectives while also always showing the entire right half of the wing. These photographs were then uploaded to *Regard3D*. After setting up the focal length and the sensor size of the camera used, the images were triangulated in search of common points whose 3D coordinates could be collected. This resulted in a sparse point cloud which was densified to get more points and a better overall shape of the wing and reference planes. This densified point cloud was then imported into another software called *MeshLab*. Each triangulation process had its own reference frame and this program allowed for the alignment of the reference frames between loading conditions through the use of rotation, translation and scaling transformations.

Figures 5.20(a) and 5.20(b) show the point clouds in *MeshLab* of the undeformed shape and the $1g$ equivalent bending moment loading condition shape, respectively.

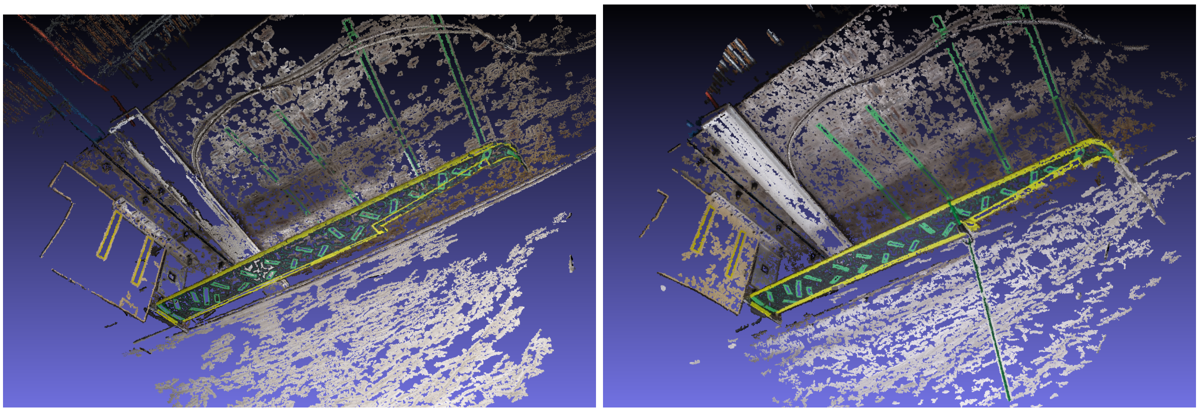

(a) Undeformed point cloud.

(b) $1g$ loading condition point cloud.

Figure 5.20: Point clouds of undeformed shape and $1g$ loading condition shape.

5.3.2 1g Loading Case

The wing root bending moment in cruise is estimated to be 65.6 N.m from the *Ansys CFX* analysis. To test this loading condition it was decided to use a single mass of 6.43 kg at the chord discontinuity 1.04 m away from the root chord.

A simulation in *Ansys Mechanical* was performed to evaluate the deformation of the FE model of the wing with this force applied and compare it with the experimental results. The maximum deformation of 3.56 mm was predicted at the tip of the winglet.

The experimental deformation at the tip of the winglet was measured in two ways. The first was through the use of the photogrammetry software and the second was through manual reading of a ruler placed perpendicularly to the ceiling and next to the winglet. The measured deformation from the ruler at the 1g loading condition was 2.8 cm while the measurement from the point cloud gave a value of 2.4 cm. There is an error of 15.4 % between the two measurement methods. The measurement of the undeformed shape was taken after the loading was applied and removed.

With respect to the computationally predicted maximum deformation, the first method shows a difference of 21.3 % while the second shows 33.43 %. This difference may be due to the extra mass which translates to an increase in stiffness and, consequently, a decrease in the maximum deformation.

The maximum deformation on the left wing was also measured with a ruler and the recorded value was 3.1 cm.

Figure 5.21 shows a photograph of the experimental loading condition.

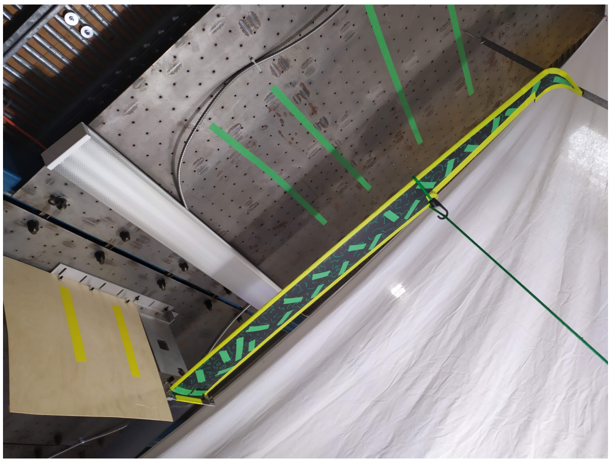

Figure 5.21: Photograph of 1g loading condition.

The point clouds from the photogrammetry software were also used to extract the 3D position of several points in the Leading Edge (LE) and Trailing Edge (TE) of both the deformed and undeformed states. By also extracting the position of the leading and trailing edge from the results from *Ansys*, figure 5.22 was created in *MATLAB* which shows the deformed and undeformed shapes from both methods.

Because there is a degree of uncertainty from the photogrammetry method, the experimental points do not lie on a straight line. A spline for both the LE and TE was used in order to smooth the experimental points. Figures 5.23(a) and 5.23(b) show the smoothed splines of the LE and TE respectively, for both the deformed and undeformed shapes. The winglets are not included because their shape could not be

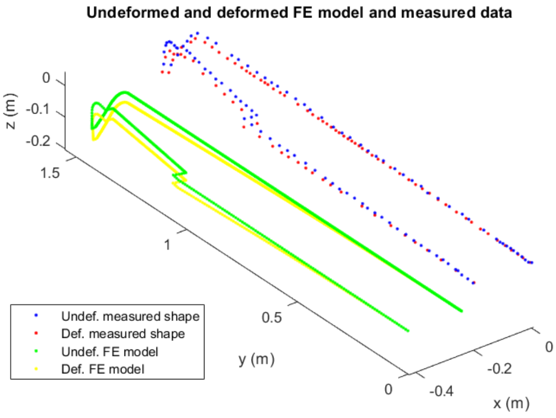

Figure 5.22: 3D plot of the deformed and undeformed LE and TE from both experimental and computational results.

replicated well with splines.

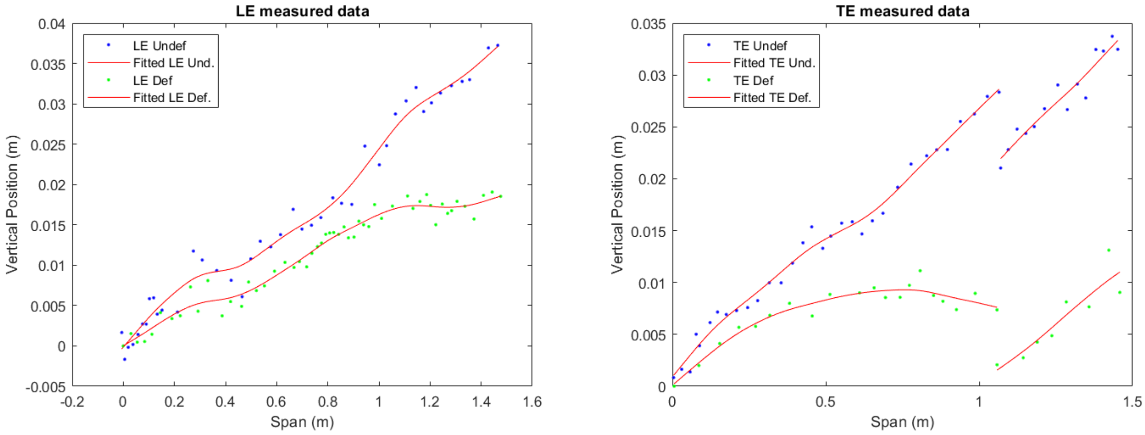

(a) Smoothing of the LE experimental points.

(b) Interpolation of the TE experimental points.

Figure 5.23: Smoothing of the extracted points from the photogrammetry software.

These splines allowed for a comparison of the expected deformation estimated from FEA and the deformation obtained from the photogrammetry method. Figure 5.24 shows the deformation of the leading edge in blue and the trailing edge in red for both methods. The sparser results are from the splines while the smoother curve is from *Ansys*.

It is possible to use photogrammetry to determine the deformation of the wing and to get a 3D model. However, the errors associated with the determination of each point make the fidelity of the displacement calculations low. Since this loading case had a small maximum displacement, this uncertainty results in a high relative error. If the loading conditions tested are higher, the relative error should be smaller.

5.3.3 3g and 4.5g Loading Cases

After the cruise loading condition was tested, the operational load limit case scenario of 3g and the ultimate loading condition of 4.5g for which the wing was designed were tested. In these cases, the load

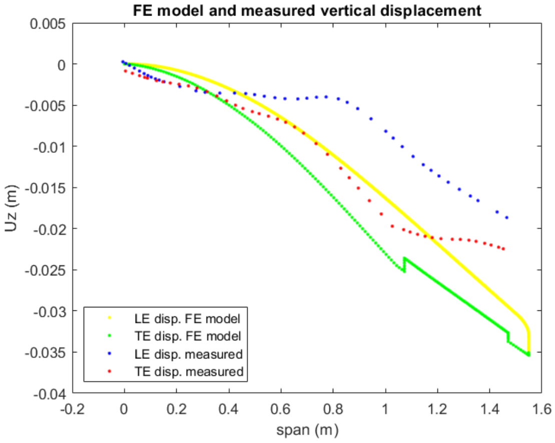

Figure 5.24: Displacement of the LE and TE for both methods.

was distributed in ten different locations along the wingspan according to the aerodynamic pressure distribution loads estimated for the wing. The loads were applied starting from the tip and ending at the root. First, the $3g$ masses were applied, the maximum deformation was recorded and after that, the masses necessary to reach the $4.5g$ were applied. Table 5.4 shows the masses and their respective locations measured from the wing root for both scenarios. One can see that the loads on the root are smaller than at the tip of the wing due to the downwash effect of the canard.

Table 5.4: Mass distribution along the wing for both tests.

Position [m]	Mass $3g$ loading case [g]	Mass $4.5g$ loading case [g]
0.075	1563	2345
0.225	1549	2324
0.375	1536	2303
0.525	1522	2283
0.663	1258	1886
0.800	3483	5224
0.950	3469	5203
1.100	3259	4888
1.250	2754	4130
1.413	2574	3861

Photographs of both conditions were taken to get the deformed shape of the structure from *Regard3D*. However, due to lack of time, these results were not processed.

For this reason, the value of the maximum deformation is available only through the ruler measurement in both wings. For the $3g$ condition, the maximum deformation on the right winglet was 8.0 cm, while in the left winglet it was 9.3 cm. In the $4.5g$ condition, the maximum measured deformation was 12 cm in the right winglet and 13.7 cm in the left winglet. The wing did not break, no cracking sounds were heard and no buckling was visible. This validated the wing for the ultimate load limit of $4.5g$.

Photographs of the wing loaded under both conditions are available in figures 5.25(a) and 5.25(b).

The deformation of the left wing was higher than the right wing in all three loading tests. This can

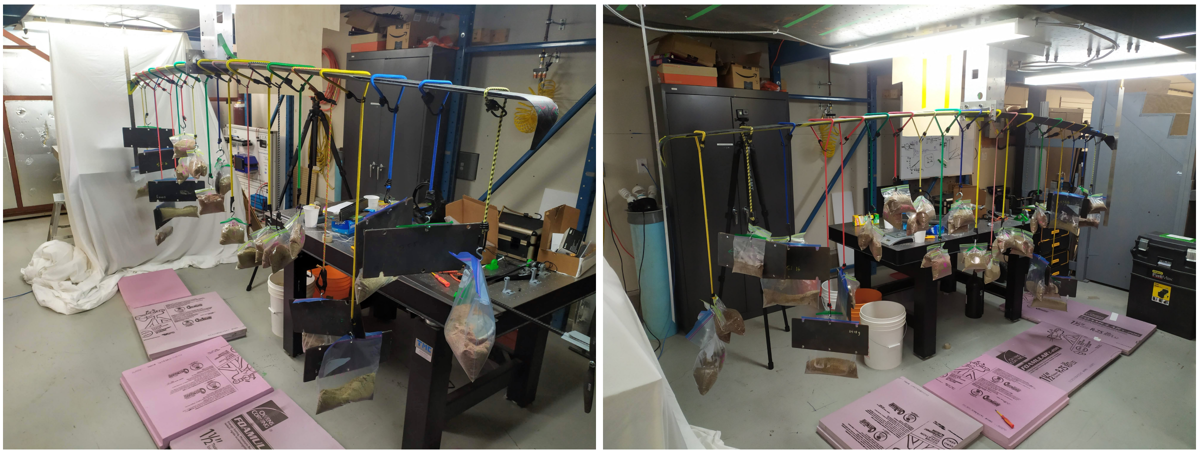

(a) Photograph of 3g loading condition.

(b) Photograph of 4.5g loading condition.

Figure 5.25: Photographs of the 3g and 4.5g loading conditions.

mean that the loading was applied asymmetrically due to human error, but this is unlikely since this behavior was detected in two different tests. The other possible reason is that the manufacturing process was not precisely symmetric and the right wing is stiffer than the left wing.

When comparing the experimental results for the 4.5g loading case with the computational result of 10.8 cm calculated in section 4.4, one may notice that the deformation is higher in the experimental tests. This is the opposite behavior of the 1g loading case. This may be due to non-linear effects being poorly estimated. The experimental maximum deformation tended to vary linearly with the load applied, while the *Ansys Mechanical* analysis shows nonlinear behavior. The 4.5g maximum deformation estimate was only 3.5 times higher than the 1g case in section 4.5. Simulating the loads as they were applied in the experiment instead of through the aerodynamic loads from FSI simulation may prove to be beneficial in getting more reliable results.

Chapter 6

Conclusions

This chapter is dedicated to the summary of the work done in this project and to the achievements reached. Some suggestions for future work are also included.

6.1 Achievements

This project started with the attainment of a structurally and aerodynamically optimized design through the means of an MDO tool. Convergence of the optimization process was reached and a configuration was chosen out of the best design points. An analysis of the geometry of this configuration and its performance was done, achieving a range 3.5 times greater than the initial reference configuration and 20 % higher than the best configuration at the start of this thesis work.

Through CFD simulations using *Ansys CFX*, the stall speed of the aircraft was determined and changes to the canard geometry were made to lower the stall speed. Furthermore, a *MATLAB* program was built to estimate the stall speed based on the canard and wing areas. The winglets were also modified to improve the smoothness of the transition between this aerodynamic surface and the wing.

Using the FEM in *Ansys Mechanical*, the structure obtained from the optimization process was redesigned to achieve a lighter structure and have more available volume inside the fuselage. Through one-way FSI simulations and non-linear structural analysis, the wing structure was also revamped to withstand the ultimate load condition. Core materials were employed to decrease weight, guarantee rigidity and prevent buckling.

The cruise condition was tested with two-way FSI simulations and the aerodynamic performance was found to not decrease with the deformation of the wing due to the aerodynamic pressure loads. The aircraft's performance at various speeds and angles of attack was determined. The trim angles were calculated for each speed as well as the power and thrust necessary for level flight.

The ailerons and rudder of the aircraft were sized and their aerodynamic coefficients were determined. The inertia of the aircraft was also estimated with the data available at the time. A Flight Dynamics Model was built using *Simulink* to simulate the aircraft behavior in various flight conditions. Another *MATLAB* program was built to calculate the lateral and longitudinal stability of the aircraft at all operational speeds and the aircraft was found to be stable in all modes at all speeds except spiral at 23 m/s. The results from this *MATLAB* program were compared to the FDM in *Simulink* and the period of the phugoid mode and the dutch roll mode were calculated and determined to be consistent between the two programs.

The designed wing was manufactured using CFRP. The molds for the top and bottom surfaces were designed and built using MDF. The skins and the internal structure of the wing were manufactured and assembled.

GVT was then performed using an impact hammer. The mode shapes and their respective frequencies were determined. Modal analysis was performed in *Ansys Mechanical* and the results from both the computational method and the experimental method were compared and found to be consistent.

Static load tests were also performed. The wing was fixed using an aluminum plate to a metal support. Photogrammetry software was used to get the 3D undeformed and deformed shapes of the wing under a 1g equivalent bending moment loading condition. The computational results were compared to this static load test. The operational limit loading condition was also tested by subjecting the wing to a 3g loading, to which the wing survived. Furthermore, the ultimate load condition was also tested without the structure showing signs of degradation.

Overall, the structural and aerodynamic design of the aircraft was successfully completed. The projected wing was built, tested and the FE model results were compared to the experimental ones.

6.2 Future Work

There are still improvements that can be made to the aircraft design.

When the systems that will go inside the aircraft are developed and their mass and geometry characteristics known, their integration with the rest of the aircraft structure has to be planned. Although the structural design for the main load-carrying structures was completed, the structural parts that fix these internal components in place were not studied and neither were the connections between the fuselage and the lifting surfaces.

Knowing the mass and inertia of these elements also allows for a better estimation of the total inertia of the aircraft, which should be updated on the FDM and the aircraft stability should also be reevaluated.

When the Flight Control System is constructed and the propulsion system designed, both can be implemented with the FDM to get better predictions of the aircraft behavior in real-world flight conditions.

The post-processing of the experimental results should be completed. The 3D model from photogrammetry method should be obtained for the 3g and 4.5g loading conditions to better evaluate the deformation from the experimental tests and compare them to the expected values from the FE model.

Due to the high aspect ratio of the wing, aeroelastic phenomena like flutter and divergence can become a problem so they should be studied. The experimental results from the GVT and the static load tests can be used to update a simplified beam model of the wing whose characteristics can then be used to determine the flutter and divergence speed and guarantee that these are outside the operational envelope of the aircraft.

Bibliography

[1] B. R. Gillespie. Ballooning in France and Britain, 1783-1786: Aerostation and Adventurism. *Isis*, 75(2):249–268, 1984. ISSN 0021-1753. doi: 10.1086/353479.

[2] Orville and W. Wright. The Wright Brothers' Aeroplane. *Aeronautical journal (London, England : 1897)*, 20(79):100–106, sep 1916. ISSN 2398-1873. doi: 10.1017/S2398187300142525. URL `https://www.cambridge.org/core/product/identifier/S2398187300142525/type/journal_article`.

[3] K. Goebel and B. Saha. *Handbook of Unmanned Aerial Vehicles*. 2015. ISBN 9789048197071. doi: 10.1007/978-90-481-9707-1_47.

[4] B. M. W. Luís. Design and development of a magnetic anomaly detection unmanned aerial vehicle. Master's thesis, Instituto Superior Técnico, 2019.

[5] T. A. S. Jesus. Surrogate-based multidisciplinary design optimization of a canard configuration vtol uav. Master's thesis, Instituto Superior Técnico, 2021.

[6] J. F. Keane and S. S. Carr. A brief history of early unmanned aircraft. In *Johns Hopkins APL Technical Digest*, volume 32, pages 558–571. 2013.

[7] U. S. Navy. Curtiss n-9. `https://commons.wikimedia.org/wiki/File:Curtiss_N-9H_on_ramp_c1918.jpg`. [Online; accessed on June 2021].

[8] D. Darling. Kettering bug. `https://www.daviddarling.info/encyclopedia/K/Kettering_Bug.html`. [Online; accessed on June 2021].

[9] M. Palik and M. Nagy. Brief history of UAV development. *Repüléstudományi Közlemények*, 31(1):155–166, 2019. ISSN 14170604. doi: 10.32560/rk.2019.1.13.

[10] K. L. Cook. The silent force multiplier: The history and role of UAVs in warfare. *IEEE Aerospace Conference Proceedings*, 2007. ISSN 1095323X. doi: 10.1109/AERO.2007.352737.

[11] S. Tsach, A. Tatievsky, and L. London. Unmanned Aerial Vehicles (UAVs). *Encyclopedia of Aerospace Engineering*, pages 1–16, 2010. doi: 10.1002/9780470686652.eae385.

[12] J. Sobieszczanski-Sobieski. Multidisciplinary Design Optimization: An Emerging New Engineering Discipline. In *Kluwer Academic Publishers*, volume 66, pages 483–496. 1995. ISBN

9786026258076. doi: 10.1007/978-94-011-0453-1_14. URL `http://link.springer.com/10.1007/978-94-011-0453-1_14`.

[13] J. Sobieszczanski-Sobieski and R. T. Haftka. Multidisciplinary aerospace design optimization: Survey of recent developments. *Structural Optimization*, 14(1):1–23, 1997. ISSN 09344373. doi: 10.1007/BF01197554.

[14] A. Papageorgiou, M. Tarkian, K. Amadori, and J. Ölvander. Multidisciplinary design optimization of aerial vehicles: A review of recent advancements. *International Journal of Aerospace Engineering*, 2018, 2018. ISSN 16875974. doi: 10.1155/2018/4258020.

[15] J. R. Martins and A. B. Lambe. Multidisciplinary design optimization: A survey of architectures. *AIAA Journal*, 51(9):2049–2075, 2013. ISSN 00011452. doi: 10.2514/1.J051895.

[16] Z. Wang, W. Huang, and L. Yan. Multidisciplinary design optimization approach and its application to aerospace engineering. *Chinese Science Bulletin*, 59(36):5338–5353, 2014. ISSN 18619541. doi: 10.1007/s11434-014-0671-1.

[17] T. W. Simpson and J. R. Martins. Multidisciplinary design optimization for complex engineered systems: Report from a national science foundation workshop. *Journal of Mechanical Design, Transactions of the ASME*, 133(10):1–10, 2011. ISSN 10500472. doi: 10.1115/1.4004465.

[18] P. Piperni, A. DeBlois, and R. Henderson. Development of a multilevel multidisciplinary-optimization capability for an industrial environment. *AIAA Journal*, 51(10):2335–2352, 2013. ISSN 00011452. doi: 10.2514/1.J052180.

[19] G. Hou, J. Wang, and A. Layton. Numerical Methods for Fluid-Structure Interaction — A Review. *Communications in Computational Physics*, 12(2):337–377, aug 2012. ISSN 1815-2406. doi: 10.4208/cicp.291210.290411s. URL `https://www.cambridge.org/core/product/identifier/S1815240600003029/type/journal_article`.

[20] B. Hans-Joachim and M. Schäfer. *Fluid-Structure Interaction*, volume 53 of *Lecture Notes in Computational Science and Engineering*. Springer Berlin Heidelberg, Berlin, Heidelberg, 2006. ISBN 978-3-540-34595-4. doi: 10.1007/3-540-34596-5. URL `http://link.springer.com/10.1007/3-540-34596-5`.

[21] J. R. Wright and J. E. Cooper. *Introduction to Aircraft Aeroelasticity and Loads: Second Edition*. 2015. ISBN 9781118700440. doi: 10.1002/9781118700440.

[22] A. Gupta, P. Seiler, and B. Danowsky. Ground vibration tests on a flexible flying wing aircraft. *AIAA Atmospheric Flight Mechanics Conference*, (January):1–10, 2016. doi: 10.2514/6.2016-1753.

[23] M. J. Kochenderfer and T. A. Wheeler. *Algorithms for Optimization*. The MIT Press, 2019. ISBN 0262039427.

[24] A. I. J. Forrester, A. Sóbester, and A. J. Keane. *Engineering Design via Surrogate Modelling*. Wiley, jul 2008. ISBN 9780470060681. doi: 10.1002/9780470770801. URL `https://doi.org/10.1002/9780470770801`.

[25] N. Bartoli, T. Lefebvre, S. Dubreuil, R. Olivanti, R. Priem, N. Bons, J. R. Martins, and J. Morlier. Adaptive modeling strategy for constrained global optimization with application to aerodynamic wing design. *Aerospace Science and Technology*, 90:85–102, 2019. ISSN 12709638. doi: 10.1016/j.ast.2019.03.041. URL `https://doi.org/10.1016/j.ast.2019.03.041`.

[26] M. L. Camilleri. *Structural analysis*. 2010. ISBN 9781617284816. doi: 10.4324/9781410600745-17.

[27] D. J N Reddy. *An Introduction to the Finite Element Method*. McGraw-Hill Education, 2005. ISBN 9780072466850. URL `https://books.google.ca/books?id=8gqnRwAACAAJ`.

[28] Ansys Inc. *Theory Reference for the Mechanical APDL and Mechanical Applications*. 2009.

[29] S. Gudmundsson. Chapter 9 - the anatomy of the wing. In S. Gudmundsson, editor, *General Aviation Aircraft Design*, pages 299–399. Butterworth-Heinemann, Boston, 2014. ISBN 978-0-12-397308-5. doi: https://doi.org/10.1016/B978-0-12-397308-5.00009-X. URL `https://www.sciencedirect.com/science/article/pii/B978012397308500009X`.

[30] F. Moukalled, L. Mangani, and M. Darwish. *The Finite Volume Method in Computational Fluid Dynamics*, volume 113 of *Fluid Mechanics and Its Applications*. Springer International Publishing, Cham, 2016. ISBN 978-3-319-16873-9. doi: 10.1007/978-3-319-16874-6. URL `http://link.springer.com/10.1007/978-3-319-16874-6`.

[31] H. K. Versteeg and W. Malalasekera. *An introduction to computational fluid dynamics - the finite volume method.* Addison-Wesley-Longman, 1995. ISBN 978-0-582-21884-0.

[32] Ansys Inc. *ANSYS CFX-Solver Theory Guide*. 2011.

[33] D. A. Caughey. *Introduction to Aircraft Stability and Control - Course Notes*. Cornell University, 2011.

[34] K. Roncin, M. Behrel, P. Iachkine, and J.-b. Leroux. Benchmark Sea Trials on a 6-Meter Boat Powered by Kite. 2020. doi: 10.3390/app10186148.

[35] J. R. Azinheira. *Flight Control - Class Notes*. Instituto Superior Técnico, 2019.

[36] J. Oliveira. *Flight Stability - Class Notes*. Instituto Superior Técnico, 2019.

[37] G. Kerschen, M. Peeters, J. C. Golinval, and C. Stéphan. Nonlinear modal analysis of a full-scale aircraft. *Journal of Aircraft*, 50(5):1409–1419, 2013. ISSN 15333868. doi: 10.2514/1.C031918.

[38] M. Peeters, G. Kerschen, and J. C. Golinval. Dynamic testing of nonlinear vibrating structures using nonlinear normal modes. *Journal of Sound and Vibration*, 330(3):486–509, 2011. ISSN 0022460X. doi: 10.1016/j.jsv.2010.08.028. URL `http://dx.doi.org/10.1016/j.jsv.2010.08.028`.

[39] A. Brandt. *Noise and Vibration Analysis*. John Wiley and Sons, Ltd, Chichester, UK, feb 2011. ISBN 9780470978160. doi: 10.1002/9780470978160. URL `http://doi.wiley.com/10.1002/9780470978160`.

[40] J. R. Wright and J. E. Cooper. *Introduction to Aircraft Aeroelasticity and Loads*. John Wiley and Sons Ltd, Chichester, UK, dec 2014. ISBN 9781118700440. doi: 10.1002/9781118700440. URL `http://doi.wiley.com/10.1002/9781118700440`.

[41] N. M. Simões. Design of a ground vibration test certification system for unmanned air vehicles. Master's thesis, Instituto Superior Técnico, 2015.

[42] C. Larson. The u.s. navy's underwater nightmare: Russia's hot rod papa-class submarine. `https://www.19fortyfive.com/2021/06/the-u-s-navys-underwater-nightmare-russias-hot-rod-papa-class-submarine/`. [Online; accessed on October 2021].

[43] T. Jesus, M. Sohst, J. L. do Vale, and A. Suleman. Surrogate based MDO of a canard configuration aircraft. *Structural and Multidisciplinary Optimization*, sep 2021. ISSN 1615-147X. doi: 10.1007/s00158-021-03051-6. URL `https://link.springer.com/10.1007/s00158-021-03051-6`.

[44] M. Sadraey. *Aircraft Design: A Systems Engineering Approach*. John Wiley and Sons Ltd, 2012.

[45] C. R. D. Hansen. Magnetic signature characterization of a fixed-wing vertical take-off and landing (vtol) unmanned aerial vehicle (uav). Master's thesis, University of Victoria, 2018.

[46] W. F. Philips. *Mechanics of Flight*. John Wiley and Sons Ltd, 2010.

Appendix A

Aerodynamic and Stability Derivatives

The formulas of the aerodynamic derivatives regarding the angular velocity and the stability derivatives can be found in this appendix. They were obtained from [35] and [46].

A.1 Aerodynamic Derivatives

$$C_{L_q} = \left(\frac{l_w}{V}C_{L_{\alpha w}} + \frac{S_c l_c}{S_w V}C_{L_{\alpha c}}\frac{S_w}{S_c}\right)\frac{2V}{\bar{c}} \tag{A.1}$$

$$C_{Y_r} = -\left(\frac{S_f l_f}{S_w V}(-C_{Y_\beta})\frac{S_w}{S_f}\right)\frac{2V}{b} \tag{A.2}$$

$$C_{l_p} = -\frac{b}{16V}C_{L_{\alpha w}}\frac{2V}{b} \tag{A.3}$$

$$C_{l_r} = \frac{S_f l_f z_f}{S_w b V}(-C_{l_\beta})\frac{S_w}{S_f}\frac{2V}{b} - 2C_{N_p} \tag{A.4}$$

$$C_{m_q} = \left(\frac{l_w^2}{\bar{c}S_w}C_{L_{\alpha w}} - \frac{S_c l_c^2}{S_w V\bar{c}}C_{L_{\alpha c}}\frac{S_w}{S_c}\right)\frac{2V}{\bar{c}} \tag{A.5}$$

$$C_{N_p} = -\left(1 - \frac{3C_{L_{\alpha w}}}{\pi AR}\right)\frac{2VbC_{L_{0w}}}{16Vb} \tag{A.6}$$

$$C_{N_r} = -\frac{S_f l_f^2}{S_w V b}(-C_{Y_\beta})\frac{S_w}{S_f}\frac{2V}{b} \tag{A.7}$$

A.2 Stability Derivatives

$$\mu = \frac{m}{\rho S_w V_0} \tag{A.8}$$

$$X_u = -\frac{C_{D_0}}{\mu} \tag{A.9}$$

$$X_w = -\frac{C_{D_\alpha} - C_{L_0}}{2\mu} \tag{A.10}$$

$$Z_u = -\frac{C_{L_0}}{\mu} \tag{A.11}$$

$$Z_w = -\frac{C_{L_\alpha} + C_{D_0}}{2\mu} \tag{A.12}$$

$$Z_q = -\frac{C_{L_q}\bar{c}}{4\mu} \tag{A.13}$$

$$Z_{\delta_{i_c}} = -\frac{C_{L_{i_c}} V_0}{2\mu} \tag{A.14}$$

$$M_w = \frac{C_{M_\alpha} m\bar{c}}{2\mu I_{yy}} \tag{A.15}$$

$$M_q = \frac{C_{M_q} m\bar{c}^2}{4\mu I_{yy}} \tag{A.16}$$

$$M_{\delta_{i_c}} = \frac{C_{M_{i_c}} m\bar{c} V_0}{2\mu I_{yy}} \tag{A.17}$$

$$Y_v = \frac{C_{Y_\beta}}{2\mu} \tag{A.18}$$

$$Y_r = \frac{C_{Y_r} b}{4\mu} \tag{A.19}$$

$$Y_{\delta_A} = \frac{C_{Y_{\delta_A}} V_0}{2\mu} \tag{A.20}$$

$$Y_{\delta_R} = \frac{C_{Y_{\delta_R}} V_0}{2\mu} \tag{A.21}$$

$$L_\beta = \frac{C_{l_\beta} m b V_0}{2\mu I_{xx}} \tag{A.22}$$

$$L_v = \frac{L_\beta}{V_0} \tag{A.23}$$

$$L_p = \frac{C_{l_p} m b^2}{4\mu I_{xx}} \tag{A.24}$$

$$L_r = \frac{C_{l_r} m b^2}{4\mu I_{xx}} \tag{A.25}$$

$$L_{\delta_A} = \frac{C_{l_{\delta_A}} m b V_0}{2\mu I_{xx}} \tag{A.26}$$

$$L_{\delta_R} = \frac{C_{l_{\delta_R}} m b V_0}{2\mu I_{xx}} \tag{A.27}$$

$$N_\beta = \frac{C_{n_\beta} m b V_0}{2\mu I_{zz}} \tag{A.28}$$

$$N_v = \frac{N_\beta}{V_0} \tag{A.29}$$

$$N_p = \frac{C_{n_p} m b^2}{4\mu I_{zz}} \tag{A.30}$$

$$N_r = \frac{C_{n_r} m b^2}{4\mu I_{zz}} \tag{A.31}$$

$$N_{\delta_A} = \frac{C_{n_{\delta_A}} m b V_0}{2\mu I_{zz}} \tag{A.32}$$

$$N_{\delta_R} = \frac{C_{n_{\delta_R}} m b V_0}{2\mu I_{zz}} \tag{A.33}$$